POLITECNICO DI TORINO

Master Degree course in Communications and Computer Networks Engineering

Master Degree Thesis

Characterization and Experimental Validation of Mode-Division-Multiplexing based receivers for Free-Space Optical systems with Turbulent Channels

Supervisors
Prof. Andrea Carena
Prof. Fernando Guiomar
Prof. Gil Fernandes

Candidate
Davide Recano

Academic Year 2024-2025

Acknowledgements

This thesis marks the end of a long and winding journey, filled with difficult moments and days that deeply shaped my everyday life. For this reason, I feel the need to write these acknowledgements, because I am fully aware that I would have never reached this point on my own. The sum of your contributions truly made the difference.

First, I would like to thank the Politecnico di Torino and, in particular, Professor Andrea Carena for presenting me with this opportunity and for his constant guidance throughout the project and the writing of this thesis. I am also deeply grateful to Instituto de Telecomunicações for hosting me and making me feel at home from the very first day, especially through my two supervisors, Professor Fernando Pedro Pereira Guiomar and Professor Gil Fernandes, always available and genuinely attentive to my work.

My thanks go to all the people I met at IT, especially Manuel Freitas, Bruno Brandão, Vítor Correia, Manuel Neves, and Salma Yahyaoui, with whom I shared most of my days, lunches, and afternoon breaks — and from whom I often asked for help. I hope I did not bother them too much.

Alongside them, I want to thank all the people who made my time in Portugal special also outside the lab. Kristal, my favourite blonde Venetian flatmate; Maria Clara, one of the craziest people I have ever met; Alice, with her unconditional love for sweets; and Serena and Fernanda — daughter and mother — who hosted me for dinners for an entire week and gifted me an endless supply of Amaro Lucano. Thank you for making sure I never felt alone, not even for a day.

My gratitude also goes to the entire Converse team for accompanying me in my first real work experience. A special thanks to Giorgia, the first person who believed in me professionally; to Vittoria, with whom I shared university worries, rants about “particularly kind” clients, and moments of pure nonsense — always during working hours, of course; and to Riccardo, who was, in sporting terms, the seasoned teammate who lovingly bullies the rookie.

Back within the walls of the Politecnico, I must mention my eternal project and group-work companions, Nicolò and Angelo: always reliable, always present, and, why not, very often better than me. I honestly do not know how many exams I would have failed without them.

Also, to Simone — “Cambu” — my partner during these years of the Master’s degree, with whom I recovered through Discord calls all the gaming time I lost during his videogame prime and his universal rage toward allies and enemies alike. Time I had to subtract from PlayStation parties with Luke and Zephir, a deadly duo of massive Venetian men whom I don’t see often, but who once managed to nearly get my white Fiat

600 stuck on a sidewalk. “Cigno, we have a problem.” And then Robb — whom I tried to avoid my entire life by escaping to Calabria for 6 to 10 weeks at a time — but whom I eventually had to pick up from Caselle airport.

Completing the legendary TRMN group, thank you to Ermo and Mutu. Teammates on the pitch, online, and at university. It is impossible to explain so many years of friendship in a few lines; I would not even know where to begin. Sincere, deep, constant friends — probably, for the first time, I explicitly say: “I love you, guys.” They are truly the best thing football ever gave me. And through football, I also met Ivan, Iacopo, and Prezio — our captain — whose support and presence I have always felt, just like on the field.

A heartfelt thank you to Federica, a ten-year-long friend, always present, a companion in endless conversations about anything — noble or trivial, you decide which is which. I am proud to have such an honest, direct, and genuine person by my side. It’s incredible to think about all the phases we went through: school, university, work, and countless heart problems.

Thanks to Simone and Kevin, who brightened those freezing 6 a.m. rides on bus 46 with conversations bouncing between football, trap music, and FIFA — specifically, a Southampton career mode — and for founding the Fantasanbe league together with Pietro and Federico, lifelong friends and the first true “best friends” I ever had, once rivals in epic A vs. B matches, now teammates.

To Chiara — inspiration and motivation in these last years. The person who makes me feel small and inadequate, yet at the same time capable of anything. An unexpected and indescribable force in my life, more excited than me for every achievement and always ready to defend me from my own negativity. Her influence in the decisions that led me to this thesis — continuing with a Master’s degree and moving abroad for this project — was decisive. Just as decisive as her entry into my life, even if she will never admit it.

Thank you to my family — to my uncles, aunts, and cousins — who have always shown me love, support, and pride, even though I am not the most present person. For me, this is what family means: feeling loved even from afar, even if we don’t see or talk often. I have always felt loved, and I hope you feel the same from me. A special thank you to my grandparents — nonna Rosaria and nonno Bruno, nonna Franca and nonno Franco — for everything you have done to give me the chance to achieve this. I hope I have honoured your sacrifices.

Finally, thank you to my core. To mom and dad, for never letting me miss anything, for lifting me up when I hit rock bottom, and for grounding me when I bragged too much. And to Gabriele, Elisa, and Matteo — my siblings — for their endless company and unconditional support, for the constant noise at home that I sometimes complain about but secretly missed when I was alone. We are an incredible team.

This thesis is yours as much as it is mine.

Ringraziamenti

Questa tesi è stata il completamento di un percorso tortuoso, caratterizzato da tanti momenti difficili e da giorni che hanno cambiato la mia quotidianità. Per questo, mi sento in dovere di scrivere questi ringraziamenti, perché so bene che non sarei mai arrivato fino a qui da solo; la somma di tutti i vostri contributi ha fatto nettamente la differenza.

Per prima cosa voglio ringraziare il Politecnico di Torino e in particolare il professore Andrea Carena per avermi presentato questa opportunità e seguito in maniera costante durante il lavoro e la stesura della tesi. Insieme a lui voglio ringraziare l'IT-Instituto de Telecomunicaçoes per avermi ospitato e fatto sentire a casa, in primo luogo attraverso i due supervisori, il professor Fernando Pedro Pereira Guiomar e il professor Gil Fernandes anche loro sempre disponibili e costantemente attenti al mio lavoro.

Grazie a tutti i ragazzi che ho incontrato nell'IT, in particolare Manuel Freitas, Bruno Brandao, Vitor Correia, Manuel Neves e Salma Yahyaoui con cui ho condiviso la maggior parte delle giornate tra pranzi e break pomeridiani e a cui ho chiesto non poche volte una mano. Spero di non averli disturbati troppo.

Insieme a loro, ringrazio tutte le persone che hanno reso speciale il mio periodo in Portogallo anche fuori dall'ambiente lavorativo; Kristal, la mia coinquilina bionda veneta preferita, Maria Clara, una delle persone più pazze che io abbia mai conosciuto, Alice, con il suo amore viscerale per i dolci, Serena e Fernanda, rispettivamente sorella e mamma, che mi hanno fatto cenare da loro per una settimana regalandomi anche un infinito Amaro Lucano. Grazie a tutti voi per non avermi fatto sentire solo nemmeno un giorno.

Grazie a tutto il team di Converse per avermi accompagnato nella mia prima vera esperienza lavorativa. In particolare grazie a Giorgia, la prima persona che ha creduto in me dal punto di vista lavorativo, grazie a Vittoria con cui ho condiviso paranoie per l'università, sfoghi per colpa di clienti particolarmente simpatici e momenti di cazzeggio, il tutto, ovviamente, in orario lavorativo e grazie a Riccardo, che è stato per me, usando una metafora sportiva, il compagno di squadra, il senatore dello spogliatoio che bullizza amorevolmente il giovane appena arrivato.

Tornando dentro alle mura del Politecnico, devo assolutamente menzionare e ringraziare i miei eterni compagni di progetto e lavoro di gruppo Nicolò e Angelo, sempre super affidabili, sempre presenti e, perché no, molto spesso più bravi di me. Non so quanti esami avrei fallito senza di loro.

Insieme a loro, compagno in questi anni di magistrale Simone, Cambu, con cui ho recuperato, nelle videochiamate su Discord, tutto il tempo che purtroppo ho perso sulla play, nel suo prime videoludico e di cattiveria verso alleati e nemici indistintamente. Tempo che ho dovuto togliere ai party sulla play con Luke e Zephir, una micidiale accoppiata di enormi uomini veneti che vedo poco, ma che ha rischiato di incastrarmi la 600 bianca in un marciapiede. "Cigno, abbiamo un problema". E poi, Robb, che ammetto di aver tentato di evitare per tutta la vita andando in Calabria dalle 6 alle 10 settimane, ma che alla fine ho dovuto raccattare all'aeroporto di Caselle.

Per chiudere il gruppo leggendario dei TRMNs, grazie a Ermo e Mutu. Compagni in campo, online e in università. Non si possono spiegare così tanti anni di rapporto in poche parole, non saprei nemmeno da dove iniziare. Amici sinceri, profondi e presenti in praticamente tutta la mia vita a cui probabilmente per la prima volta dico esplicitamente "vi voglio bene". Sono stati nettamente la cosa più bella che il calcio mi ha lasciato. Insieme a loro, da questo sport, ho avuto la fortuna di avere come compagni di vita, non solo di reparto, Ivan, Iacopo e Prezio, il capitano, di cui, come in campo, ho sempre sentito il sostegno e la copertura, anche se mi allontanavo.

Grazie a Federica, amica decennale, onnipresente, compagna di infinite conversazioni su qualsiasi argomento, dai più bassi ai più nobili, decidi tu quali sono gli uni e quali sono gli altri. Sono orgoglioso di poter avere accanto a me una persona onesta, diretta, vera. E' incredibile pensare a tutti i cambiamenti e le fasi attraverso cui siamo passati: dalla scuola, all'università, al lavoro, passando per mille problemi di cuore.

Grazie a Simone e Kevin, che mi hanno alleggerito quel gelido 46 alle 6 del mattino rimbalzando nelle conversazioni tra calcio, trap e fifa, nello specifico la carriera con il Southampton, ma anche per aver fondato la lega Fantasambe insieme a Pietro e a Federico, amici storici, i primi veri "migliori amici" della mia vita, avversari prima negli epici A contro B e compagni adesso.

A Chiara, ispirazione e motivazione di questi ultimi anni. La persona che mi fa sentire piccolo e scarso, ma allo stesso tempo capace di qualsiasi cosa. Un' inspiegabile ed inaspettata spinta nella mia vita, più gasata di me per ogni traguardo e sempre in prima linea per difendermi dalla mia negatività. La sua influenza nel prendere le decisioni che mi hanno portato a fare questa tesi, sia per la scelta di proseguire in un percorso magistrale, sia per la scelta di andare a fare la tesi all'estero, è stata decisiva. Così come decisivo è stato il suo ingresso nella mia vita anche se non lo dirà mai.

Grazie a tutta la mia famiglia, agli zii, ai cugini che mai mi hanno fatto mancare la loro stima, il loro supporto e il volermi bene, nonostante io non mi faccia molto sentire o vedere. Ringrazio ognuno di voi per tutto l'affetto che sento. Per me questa è la famiglia: sentirmi voluto bene anche se lontano, anche se vi vedo o vi parlo poco. Mi sono sempre sentito voluto bene e spero che voi sentiate lo stesso da parte mia. Un grazie particolare ai nonni, nonna Rosaria e nonno Bruno, nonna Franca e nonno Franco, per quello che avete fatto per donare a me la possibilità di fare questo. Spero di essere stato all'altezza dei vostri sacrifici.

Infine grazie al mio nucleo. Grazie a mamma e papà per non avermi mai fatto mancare niente, per avermi tirato su quando mi buttavo eccessivamente giù e per avermi tenuto coi piedi per terra quando mi sono vantato troppo. Grazie a Gabriele, Elisa e Matteo, i miei fratelli, per la loro eterna compagnia e il loro disinteressato sostegno, per quel continuo brusio che c'è in casa di cui a volte mi lamento, ma che ho, a tratti, sofferto quando ero da solo. Siamo un team incredibile.

Questa tesi è anche vostra.

Abstract

In this thesis, we explore advanced techniques to mitigate the effects of atmospheric turbulence in Free-Space Optical (FSO) communication systems. The focus is on the application of Mode Division Multiplexing (MDM) techniques in the receiver apparatus of FSO systems. After presenting the theoretical foundations and reviewing the state of the art of MDM-supported receivers for FSO systems, we experimentally characterize an innovative solution based on Multi Plane Light Converter (MPLC). We then evaluate its performance compared both to a photonic lantern approach and to conventional Single Mode Fiber (SMF). The study demonstrates the potential of MPLC to enhance mode separation and reduce modal crosstalk, both of which are critical in improving signal robustness under turbulent propagation conditions. Results suggest that MPLC-based solutions offer a promising path toward more reliable and higher-capacity optical wireless communication links in the presence of atmospheric distortions. These findings contribute to the development of next-generation FSO systems with enhanced performance in challenging environments.

Contents

Chapter 1

Introduction

1.1 Introduction to Free-Space Optical Communications

FSO communication systems have recently emerged as a highly promising solution for future high-capacity wireless transmission links. FSO communications refer to wireless optical links in which information is conveyed by collimated light beams propagating through the atmosphere or vacuum, typically using modulated infrared wavelengths [1]. Unlike radio-frequency technologies, which require regulated spectral bands and are constrained by limited bandwidth availability, FSO systems exploit optical carriers, enabling extremely high data rates and providing fiber-like performance without the need for a physical waveguide [2]. The basic architecture of an FSO link consists of an optical transmitter, a beam expansion and collimation stage, free-space propagation, and an optical receiver equipped with focusing optics and photodetection circuitry [3].

The key advantage of FSO communications lies in the very high carrier frequency of optical signals (on the order of hundreds of terahertz), which allows transmission capacities well beyond those achievable with microwave or millimeter-wave systems, while also avoiding electromagnetic interference and spectrum licensing constraints [4]. These characteristics make FSO links attractive for a wide range of deployment scenarios, including high-capacity inter-building backhaul, rapidly deployable temporary networks, airborne and UAV communication, and, most notably, satellite-to-ground, satellite-to-satellite and deep-space optical communication links [5]. The compactness and low power consumption of optical hardware enable lightweight communication terminals suitable for spaceborne and stratospheric platforms. However, FSO links are not free from impairments. Long-distance propagation leads to beam divergence, while mechanical vibrations and atmospheric dynamics introduce pointing and alignment errors. Moreover, adverse weather conditions such as fog, rain, and snow can severely attenuate the optical signal. Most critically, atmospheric turbulence causes random refractive-index fluctuations that distort the wavefront and induce irradiance fluctuations at the receiver, leading to performance degradation [6]. Therefore, in order to fully exploit the high-capacity potential of FSO communications, it becomes crucial to investigate how turbulence affects optical propagation and to explore transmission strategies capable of enhancing robustness under deteriorated channel conditions.

1.2 Impact of Atmospheric Turbulence

Atmospheric turbulence is widely recognized as one of the dominant impairment factors in free-space optical communication links [4]. Turbulence originates from random spatial and temporal variations of temperature and pressure in the atmosphere, which produce fluctuations of the refractive index of air [7]. As an optical beam propagates through such a medium, its wavefront becomes distorted and its intensity distribution may change unpredictably over time [8].

These distortions manifest primarily in two observable effects at the receiver. The first is wavefront aberration, which results in beam wandering and spreading [9]. The second is scintillation, namely rapid fluctuations in the received optical power caused by interference of the distorted wavefront [10]. Scintillation can severely degrade the signal-to-noise ratio, especially over long propagation distances or in strong turbulence conditions.

Since these effects are dynamic and depend on atmospheric conditions, the optical channel becomes inherently time-varying and difficult to predict. In this context, the characterization of turbulence strength plays a fundamental role in evaluating the behavior of FSO systems. A key metric used for this purpose is the Rytov variance [4].

In qualitative terms, the Rytov variance provides an indication of the strength of scintillation along the propagation path. Low values correspond to mild and slowly varying intensity fluctuations, whereas high values are associated with strong turbulence conditions, where the received signal experiences deep fading and rapid power variations. This interpretation is widely adopted in the literature, and it is commonly used to distinguish weak, moderate, and strong turbulence regimes in optical links. Recent studies, such as the unified statistical modeling of turbulence-induced fading in Orbital Angular Momentum (OAM)-multiplexed FSO systems [11], further demonstrate how the Rytov variance correlates with the severity of irradiance fluctuations and thus serves as a key indicator of link reliability. For this reason, the Rytov variance is widely used to compare the effectiveness of different transmission strategies and spatial mode allocations. A more detailed discussion of this parameter and its role in system performance evaluation will be presented in Chapter 2.

Atmospheric turbulence therefore represents a major limitation for the reliability of free-space optical links, as it introduces random signal fading and performance fluctuations that cannot be easily mitigated through simple power control or beam alignment alone. This raises the need for strategies that can increase the robustness of the received signal by reducing the sensitivity to scintillation and wavefront distortions. Instead of relying solely on improving optical hardware or atmospheric compensation techniques, an increasingly effective approach is to exploit the spatial structure of the optical field itself. This idea leads to the use of MDM, which aims to distribute the transmitted power across multiple spatial modes so that the effects of turbulence can be averaged or compensated. The principles and motivations behind this approach are introduced in the following section.

1.3 Mode-Division Multiplexing as a Mitigation Strategy

Atmospheric turbulence introduces random wavefront distortions and intensity fluctuations that strongly affect the stability of free-space optical links. When transmission is performed using a single optical mode, such as a Gaussian beam, these distortions directly translate into fluctuations of the received power, often resulting in deep fading and performance degradation [4]. To improve robustness, it is beneficial to exploit the fact that light can propagate in multiple orthogonal spatial modes, each representing a distinct field distribution that is affected differently by turbulence.

This idea leads to the use of MDM, where information is distributed across several spatial modes rather than being confined to a single one [12]. Since turbulence does not distort all modes in the same way at the same time, the fluctuations experienced by each modal channel are only partially correlated. By coherently combining or jointly detecting multiple modes at the receiver, the system can effectively average out these fluctuations, resulting in a received signal that is more stable over time. In other words, MDM provides a form of spatial diversity, improving resilience to scintillation without requiring changes in transmitted power or complex adaptive optics.

In the context of this thesis, modal diversity is applied specifically at the receiver side: the optical field arriving from the turbulent channel is decomposed into a set of orthogonal spatial modes, and their contributions are combined to obtain a more stable received signal. This approach leverages turbulence-induced mode coupling rather than requiring multiple independent transmitters, making it particularly suitable for practical FSO implementations.

This strategy has been explored using various families of spatially structured beams, including Hermite-Gaussian (HG), Laguerre-Gaussian (LG), and OAM modes [11, 12]. However, the effectiveness of modal diversity depends critically on the ability to separate and recombine the modes without introducing interference. Indeed, mode diversity is beneficial only when the different excited modes can be properly distinguished and processed at the receiver [13], otherwise cross-talk may negate the diversity gains.

In conventional FSO links employing SMF, the transmitted field is constrained to the fundamental Gaussian mode. As a consequence, any turbulence-induced distortion directly leads to received power fluctuations, making SMF-based links particularly sensitive to scintillation and beam wander [4]. In contrast, MDM systems distribute optical power across multiple orthogonal modes so that each mode experiences different fading realizations. The resulting modal diversity leads to statistical averaging of turbulence effects, yielding a more stable received signal.

To realize this benefit in practice, the receiver must be capable of separating the optical field into its constituent modes. Several demultiplexing architectures have been proposed for this purpose. The Photonic Lantern (PL) performs a passive low-loss transformation from a multimode input to multiple single-mode outputs through an adiabatic taper [14], preserving orthogonality but offering limited control over mode selectivity. A more flexible solution is the MPLC, which implements a sequence of phase transformations to convert spatial modes into distinct Gaussian-like outputs with high mode selectivity and low cross-talk [15]. This makes the MPLC particularly suitable for MDM-based FSO links, especially when higher-order spatial modes are used.

In this context, comparing MPLC and PL reception to conventional single-mode detection provides insight into how spatial mode diversity can effectively enhance robustness under atmospheric turbulence.

1.4 Objectives and Contributions of This Thesis

The aim of this thesis is to investigate experimentally the effectiveness of MDM as a strategy to mitigate the impact of atmospheric turbulence in FSO communication systems. In particular, the work focuses on the use of a MPLC for spatial mode multiplexing and demultiplexing, and evaluates its performance in comparison with conventional single-mode and PL-based receivers.

The first objective is the characterization of the MPLC device, analyzing its behavior with respect to different spatial modes. This includes the measurement of insertion loss for each output mode, and a comparison with the performance of a PL. Additional effects, such as polarization sensitivity, fiber bending, and modal correlation at the MPLC output, are also examined to assess the robustness and practical usability of the device.

The second objective is the evaluation of received power stability under atmospheric turbulence, by comparing three different reception configurations: single-mode fiber, photonic lantern, and MPLC. The analysis focuses on two performance indicators: the moving average of the received power and the Rytov variance, used as a measure of scintillation strength. Based on these metrics, a subset of four spatial modes is identified as the most resilient to turbulence when combined in an MDM scheme.

Finally, the third objective is the experimental validation of a complete communication link, where real data transmission is performed using modulation, amplification, and digital signal processing. This transmission test is used to assess whether the selected multimode configuration provides improved Signal-to-Noise Ratio (SNR) compared to single-mode and PL-based reception, thereby confirming the practical effectiveness of mode diversity in mitigating turbulence-induced fading.

Overall, the contributions of this thesis can be summarized as follows:

- experimental characterization and performance assessment of an MPLC-based spatial mode demultiplexing system;
- comparative analysis of received power fluctuations and turbulence impact across SMF, PL, and MPLC reception architectures;
- demonstration of improved communication performances, in terms of SNR, when using a selected subset of spatial modes in an MDM transmission scheme under turbulent propagation conditions.

1.5 Structure of The Thesis

The remainder of this thesis is organized as follows.

Chapter 2 first presents mode-division multiplexing and the spatial modes considered in this work. Then. it introduces the state of the art related to free-space optical communication systems. The chapter introduces and finally reviews different coupling and demultiplexing architectures, including SMF, PL, and the MPLC. The physical origin and statistical characterization of atmospheric turbulence are also discussed, with particular attention to the Rytov variance as a metric for scintillation. The chapter concludes with an overview of coherent optical communication systems and digital signal processing techniques relevant to the final experimental validation.

Chapter 3 focuses on the experimental characterization of the MPLC device employed in this work. The insertion loss associated with different spatial modes is measured and compared with the performance of a photonic lantern. The effects of polarization changes, fiber bending, and modal correlation at the output of the MPLC are also analyzed to assess the device's robustness and suitability for use in multimode scenarios.

Chapter 4 investigates the propagation of optical modes through atmospheric turbulence. Then, a comparison is carried out among three receiver configurations: single-mode fiber, photonic lantern, and MPLC. The analysis examines the stability of the received power using a moving average metric and evaluates the impact of turbulence through the Rytov variance. Based on these results, a subset of four spatial modes is selected for enhanced resilience, and the benefits of modal diversity are discussed.

Chapter 5 validates the selected modal configuration in a complete communication scenario. Real data transmission is performed using coherent modulation, amplification, and digital signal processing. The quality of transmission is assessed in terms of signal-to-noise ratio, demonstrating the effectiveness of mode-division multiplexing in improving robustness against turbulence-induced fading.

Chapter 6 concludes the thesis by summarizing the main findings, discussing the implications of the results, and outlining potential directions for future research in the development of turbulence-resilient free-space optical communication systems.

Chapter 2

State of the art and theoretical background

This chapter provides the theoretical background required to understand the techniques and experimental results presented in the subsequent parts of this thesis. The focus is placed on free-space optical communication systems and how to improve robustness under atmospheric turbulence at the receiver.

A subsequent overview of the state of the art in mode-division demultiplexing is then presented, discussing and contextualizing the main approaches, namely SMF-based schemes, PLs, and MPLC. First, the principles of MDM are introduced, with particular attention to Hermite–Gaussian spatial modes and their suitability for free-space propagation. Then, different mode multiplexing and demultiplexing architectures are reviewed, including the SMF interface, the PL, and the MPLC, which will play a central role in the experimental analysis of this work.

The chapter then discusses the physical mechanisms of atmospheric turbulence and its impact on optical wave propagation, together with the commonly used metrics for characterizing turbulence strength. Finally, the fundamentals of coherent optical communications are summarized, and the digital signal processing steps required for coherent detection.

Overall, the goal of this chapter is to establish the theoretical framework necessary to interpret the experimental characterization of mode demultiplexing devices (Chapter 3), the analysis of turbulence effects on received power statistics (Chapter 4), and the coherent transmission experiments (Chapter 5).

2.1 Mode Division Multiplexing

2.1.1 Introduction to Spatial Modes

An optical mode is a stable, self-consistent solution of the wave equation that describes the electromagnetic field distribution of a propagating beam under given boundary conditions [16] [17]. In optical fibers, modes correspond to eigenfunctions of the Helmholtz equation that satisfy the boundary conditions imposed by the core-cladding structure. In free space, they are solutions of the paraxial wave equation that maintain their transverse intensity and phase profiles during propagation.

All optical mode are characterized by a spatial field distribution, a propagation constant, and a polarization state. Modes are orthogonal, which mathematically means that two modes $E_m(x, y)$ and $E_n(x, y)$ satisfy:

$$\int E_m(x, y)\, E_n^*(x, y)\, dA = 0 \quad \text{for } m \neq n, \tag{2.1}$$

where the integral is performed over the transverse plane. This orthogonality allows independent information channels to be multiplexed and demultiplexed on different modes without coherent interference, forming the basis of Mode Division Multiplexing.

In fibers, the refractive index profile determines the supported modes. Step-index fibers have a uniform core refractive index with a sharp core-cladding interface, while graded-index fibers feature a smooth radial decrease. These profiles define the Linearly Polarized (LP) modes, which are approximate solutions in weakly guiding fibers [16]. LP_{01} has a nearly Gaussian profile, while LP_{11a} and LP_{11b} exhibit two-lobed intensity patterns corresponding to linear combinations of free-space HG modes.

Other families of spatial modes, such as LG modes and OAM modes, are often used in high-capacity links due to their intrinsic orthogonality and cylindrical symmetry.

In this thesis, these broader families are mentioned only for context. The experimental work focuses on Hermite-Gaussian modes, which provide a separable basis well suited for free-space propagation and, as demonstrated in later chapters, for turbulence-resilient modal decomposition at the receiver.

2.1.2 Modal Analysis at the Receiver

The focus of this work is on the receiver side, which collects an optical signal distorted by turbulence and analyzes it by decomposing the field into orthogonal spatial modes. This decomposition allows to study turbulence-induced distortions and crosstalk between modes.

The projection of the received field onto a given mode is expressed as:

$$c_{mn} = \iint E_{\text{recv}}(x, y)\, \mathrm{HG}_{mn}^*(x, y)\, dx\, dy, \tag{2.2}$$

where:

- $E_{\text{recv}}(x, y)$ is the complex field at the receiver plane.
- c_{mn} represents the amplitude of the mode HG_{mn}. The corresponding modal power is $|c_{mn}|^2$.

Modal diversity exploits the fact that turbulence-induced fading is only partially correlated between modes. By coherently combining multiple modes at the receiver, the variance of received power can be reduced, enhancing the stability of the detected signal without requiring multiple transmitters [13] [15].

Devices such as the PL and the MPLC implement high-fidelity mode separation. While the PL separates LP modes (LP_{01}, LP_{11a} and LP_{11b}) in fiber, the MPLC is capable of demultiplexing free-space HG modes with low insertion loss, high mode selectivity, which means low crosstalk and exploits a larger number of modes. These devices enable detailed experimental analysis of mode-specific turbulence effects.

As demonstrated in Chapter 3, the MPLC was experimentally validated as a high-fidelty HG-mode demultiplexer. In the final communication experiment (Chapter 5), the same modal projections were used to implement Multiple-Input Single-Output (MISO) diversity combining, revealing the performance benefits of multi-mode reception under turbulence.

2.1.3 Hermite-Gaussian Modes

HG modes constitute a fundamental family of solutions to the paraxial wave equation in rectangular coordinates [4]. The paraxial approximation of the Helmholtz equation applies to optical beams whose envelope varies slowly along the propagation direction z:

$$\nabla_T^2 E(x,y,z) - 2ik\frac{\partial E(x,y,z)}{\partial z} = 0, \tag{2.3}$$

where:

- ∇_T^2 is the transverse Laplacian,
- $k = \frac{2\pi}{\lambda}$ is the wavenumber,
- $E(x,y,z)$ is the slowly varying field envelope.

This approximation simplifies the full Helmholtz equation under the assumption that the beam propagates mainly along z and that transverse variations are slow relative to the wavelength.

A standard method to solve the paraxial equation in rectangular coordinates is to assume a separable solution:

$$E(x,y,z) = X(x,z)\,Y(y,z)\,e^{-ikz}. \tag{2.4}$$

Substituting this form into the paraxial equation yields two independent one-dimensional equations along x and y:

$$\frac{\partial^2 X}{\partial x^2} - 2ik\frac{\partial X}{\partial z} = 0, \quad \frac{\partial^2 Y}{\partial y^2} - 2ik\frac{\partial Y}{\partial z} = 0. \tag{2.5}$$

The transverse equations are solved in terms of the *Hermite polynomials* $H_m(x)$ and $H_n(y)$, which naturally arise from the harmonic-oscillator differential equation:

$$\frac{d^2 H_m(\xi)}{d\xi^2} - 2\xi\frac{dH_m(\xi)}{d\xi} + 2mH_m(\xi) = 0, \tag{2.6}$$

where ξ is the normalized transverse coordinate. This ensures that the modes are orthogonal and form a complete basis for any transverse field profile.

The one-dimensional HG functions along x and y can be expressed as:

$$X_m(x,z) = \frac{1}{\sqrt{2^m m!\, w(z)\sqrt{\pi}}} H_m\Big(\sqrt{2}\frac{x}{w(z)}\Big) \exp\Big[-\frac{x^2}{w^2(z)}\Big] \exp\Big[-ik\frac{x^2}{2R(z)} + i(m+1/2)\phi(z)\Big], \tag{2.7}$$

$$Y_n(y,z) = \frac{1}{\sqrt{2^n n!\, w(z)\sqrt{\pi}}} H_n\Big(\sqrt{2}\frac{y}{w(z)}\Big) \exp\Big[-\frac{y^2}{w^2(z)}\Big] \exp\Big[-ik\frac{y^2}{2R(z)} + i(n+1/2)\phi(z)\Big]. \tag{2.8}$$

The normalization ensures that the total optical power in each mode integrates to unity.

The full two-dimensional HG mode of order (m,n) is obtained by combining the x and y components:

$$\mathrm{HG}_{mn}(x,y,z) = X_m(x,z)\, Y_n(y,z), \tag{2.9}$$

or explicitly:

$$\mathrm{HG}_{mn}(x,y,z) = \frac{H_m\left(\sqrt{2}\frac{x}{w(z)}\right) H_n\left(\sqrt{2}\frac{y}{w(z)}\right)}{w(z)} \exp\Big[-\frac{x^2+y^2}{w^2(z)}\Big] \exp\Big[-ik\frac{x^2+y^2}{2R(z)} + i\phi_{mn}(z)\Big], \tag{2.10}$$

with:

$$w(z) = w_0\sqrt{1+\left(\frac{z}{z_R}\right)^2}, \tag{2.11}$$

$$R(z) = z\left[1+\left(\frac{z_R}{z}\right)^2\right], \tag{2.12}$$

$$\phi_{mn}(z) = (m+n+1)\arctan\left(\frac{z}{z_R}\right). \tag{2.13}$$

Here,

- $w(z)$ is the beam radius,
- $R(z)$ the wavefront curvature,
- $\phi_{mn}(z)$ the Gouy phase, which varies with mode order and affects interference and phase-sensitive detection.

HG modes are orthogonal:

$$\iint \mathrm{HG}_{mn}(x,y,z)\, \mathrm{HG}^*_{pq}(x,y,z)\, dx\, dy = \delta_{mp}\, \delta_{nq} \tag{2.14}$$

This property allows them to form a complete basis for decomposing the received optical field.

Although higher-order modes ($m+n>0$, so the modes different from the fundamental one) are more sensitive to phase and amplitude distortions caused by atmospheric

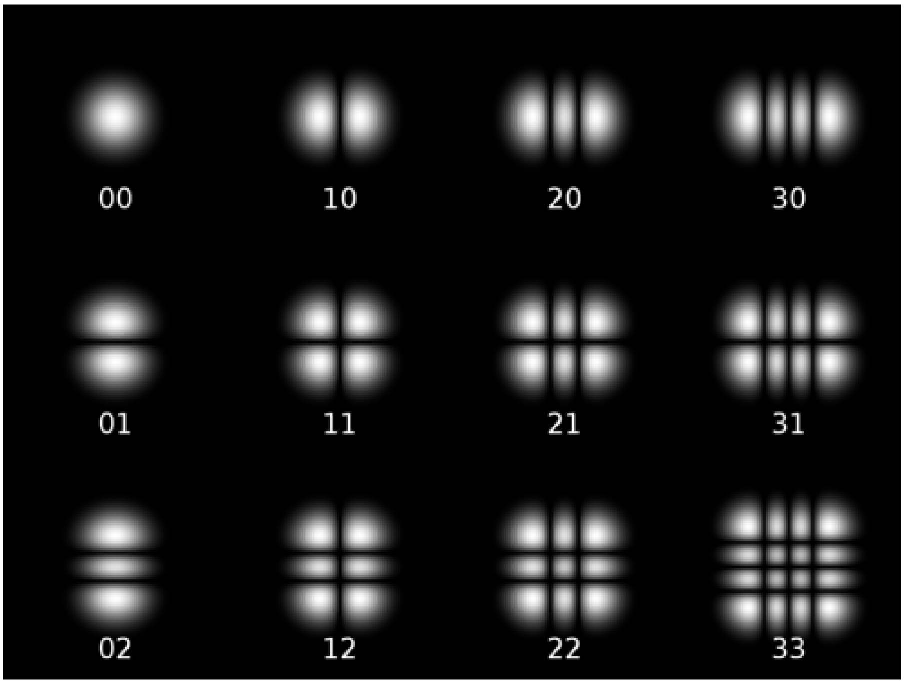

Figure 2.1: Intensity patterns for HG modes up to order 6. Reproduced from Wikimedia Commons under CC BY-SA 3.0 by DrBob.

turbulence, this property can be exploited at the receiver. By projecting the received beam onto multiple HG modes, it is possible to implement modal diversity.

In weak turbulence conditions, HG_{00} typically captures most of the received power, while higher-order modes carry only a small fraction. However, under stronger distortions, these modes become increasingly valuable, because their spatial structure is less affected by beam wander and centroid fluctuations, allowing them to retain a complementary projection of the distorted wavefront. Some advantages could be:

- each mode experiences partially independent turbulence-induced distortions;
- combining the detected signals from multiple modes reduces fluctuations in the total received power;
- this improves link stability without modifying the transmitted signal, making it ideal for receiver-side compensation of atmospheric turbulence.

In other words, adding higher-order HG modes at the receiver does not increase transmitted capacity but enhances robustness against turbulence.

Figure 2.1 shows the transverse intensity patterns of HG modes up to order 6.

2.2 Mode Coupling e Multiplexing Devices

In mode-division demultiplexing systems, the ability to selectively excite, transport, and exctract spatial modes is determined by the optical devices placed at the receiver. These mode-management components define how efficiently power is coupled into spatial channels, how well the modal orthogonality is preserved, and how robustly individual modes can be recovered after propagation through a perturbed medium.

Different device architectures have been developed to perform mode coupling and demultiplexing, each with dinstinct advantages and limitations in terms of insertion loss, modal selectivity, scalability and polarization dependence. Among them, three representative solutions are particularly relevant in the context of this work:

- the standard single-mode fiber;
- the photonic lantern;
- the Multi-Plance Light Converter.

In the following subsections, each device is introduced and analyzed, with emphasis on its operational principles and relevance to spatial-mode detection in turbulent free-space propagation.

2.2.1 Single Mode Fiber

A SMF supports only the fundamental linearly polarized mode (LP_{01}) and rejects all higher-order spatial content. When an optical field $E_{\text{in}}(x, y)$ is coupled into the fiber, only the component that matches the fundamental mode profile is guided, while the remainder is radiated or lost at the input facet. This behavior is well established in classical fiber theory [16, 17].

The coupling efficiency can be expressed through the normalized overlap integral:

$$\eta = \frac{\left|\iint E_{\text{in}}(x, y)\, E_{00}^{*}(x, y)\, dx\, dy\right|^2}{\left(\iint |E_{\text{in}}|^2\, dx\, dy\right)\left(\iint |E_{00}|^2\, dx\, dy\right)}, \tag{2.15}$$

showing that the SMF acts as a spatial mode filter that retains only the part of the wavefront whose amplitude and phase distribution match the fundamental mode.

In ideal laboratory conditions, such as diffraction-limited beams or well-aligned setups, this results in stable and efficient coupling. However, in FSO systems, the received wavefront is significantly distorted by atmospheric turbulence, which induces scintillation, beam wander, and phase-front corrugation [4, 8, 10]. These effects reduce the spatial coherence of the beam and degrade its overlap with the SMF-guided mode. As a consequence, during turbulence-induced fading events, the SMF captures only a small and highly variable fraction of the received optical power.

This limitation of SMF-based reception in FSO systems is well documented in the literature [2, 3, 5]. Because the SMF cannot access higher-order spatial components that may still carry useful optical power—or even a less distorted projection of the incoming field—the receiver experiences deep power fades and large SNR fluctuations, ultimately leading to Bit Error Rate (BER) degradation and unstable link performance.

For these reasons, although SMF reception is standard in fiber-based coherent systems, it is suboptimal for turbulence-impaired FSO channels. This motivates the use of mode-selective devices such as photonic lanterns [14] and MPLCs [15], which preserve multiple spatial projections of the distorted wavefront and enable improved turbulence resilience through modal diversity.

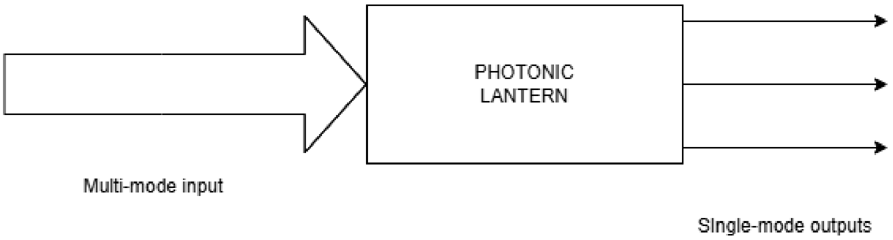

Figure 2.2: PL block diagram

2.2.2 Photonic Lantern

The PL is a passive spatial demultiplexing device that enables the separation of a multimode input field into multiple single-mode outputs. When used at the receiver of an FSO system, the collected free-space beam is first coupled into a Few Mode Fiber (FMF), after which the PL performs an adiabatic transition that maps the guided modes of the FMF onto individual single-mode fibers. In this configuration, the device functions as a *mode demultiplexer*, providing several spatially selective detection branches that can be processed independently. Figure 2.2 illustrates the conceptual block diagram of this receiver-side configuration.

A PL operates by gradually transforming a multimode core into a bundle of isolated single-mode cores. If the taper transition is sufficiently adiabatic, the orthogonal eigenmodes supported by the FMF evolve into distinct single-mode channels with minimal coherent interference. In weakly guiding step-index fibers, this typically results in the separation of the LP_{01}, LP_{11a}, and LP_{11b} modes, which constitute the fundamental modal set for three-mode lanterns [14]. As a consequence, the PL provides a fixed modal basis determined entirely by the fiber geometry.

When applied to free-space optical reception, this modal decomposition allows the receiver to extract different projections of the distorted wavefront. Each output SMF preserves the amplitude and phase evolution of one spatial mode, enabling the study of mode-dependent fading and offering a basic form of modal diversity. Compared to direct coupling into a single-mode fiber, the PL thus captures multiple partially uncorrelated spatial components of the received beam, providing improved resilience to turbulence-induced fluctuations. Figure 2.3 shows the actual photonic lantern used in the experimental campaign of this thesis.

However, several limitations arise in FSO scenarios. A major issue is the polarization sensitivity of the LP-mode excitation: since LP_{11a} and LP_{11b} differ only by their polarization orientation, the power balance across PL outputs depends strongly on the instantaneous polarization state of the incoming beam—a parameter that is neither stable nor controllable in free-space propagation [2]. This makes the modal decomposition inherently polarization-dependent, reducing reproducibility and robustness. Furthermore, the number and nature of modes separated by the PL are fixed by the supporting FMF, limiting the richness of the spatial decomposition and preventing the use of alternative modal bases such as Hermite–Gaussian modes.

Figure 2.3: Photograph of the PL device used in this thesis, featuring 1 FMF input and 3 SMF outputs.

Despite these constraints, the PL represents an important intermediate reference for spatial-mode demultiplexing. In this thesis, it serves as a benchmark against which the capabilities of the MPLC can be evaluated, highlighting the advantages of a free-space compatible, polarization-insensitive, and higher-dimensional mode decomposition.

2.2.3 Multi-Plane Light Converter (MPLC)

MPLC is a powerful and increasingly adopted technique for spatial-mode manipulation in both free-space and fiber-based optical systems. Unlike devices such as photonic lanterns—which rely on adiabatic transitions inside multimode fibers—the MPLC implements mode transformations using a sequence of engineered phase masks that perform a unitary mapping between a set of input modes and a set of output modes [15,18]. This makes it especially suitable for free-space HG modes and for applications requiring high modal selectivity, low crosstalk, and flexible mode bases.

The MPLC performs an arbitrary spatial transformation by decomposing it into a sequence of simpler phase manipulations. Conceptually, any linear optical transformation

$$T : \{E_m(x,y)\} \to \{E_n(x,y)\}$$

can be approximated by alternating free-space propagation, between the phase masks, and phase modulation.

An MPLC consists of:

- a set of N fixed phase plates (or reflective phase masks),
- separated between them by free-space propagation segments,
- engineered to collectively implement a desired unitary mapping.

At each plane, the transverse field undergoes a transformation:

$$E_{k+1}(x,y) = \mathcal{F}^{-1}\Big\{\mathcal{F}\{E_k(x,y)\}\exp[i\phi_k(x,y)]\Big\}$$

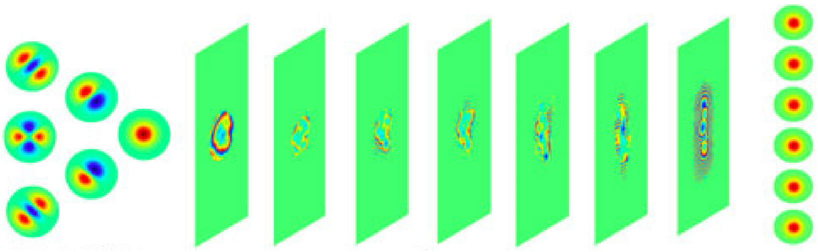

Figure 2.4: Conceptual internal structure of an MPLC: a sequence of phase masks separated by free-space propagation sections implements an arbitrary spatial transformation. The multi-mode input (left) is transformed to the single mode array (right).

where $\phi_k(x, y)$ is the phase profile of the k-th mask. By properly optimizing all $\phi_k(x, y)$, the MPLC can realize:

- mode demultiplexing (MUX/DEMUX);
- spatial filtering;
- arbitrary unitary transforms;
- separation of HG, LG, OAM or custom mode sets.

A key advantage is that the mapping accuracy increases with the number of planes. Typical devices for HG or LG modes use between 7 and 14 planes. The result is a quasi-unitary transform with:

- mode-dependent loss often below 3–5 dB;
- inter-modal crosstalk often below –20 dB;
- high stability and polarization tolerance.

This makes MPLCs ideal for mode decomposition of free-space beams affected by atmospheric turbulence [19]. A practical MPLC demultiplexer, such as the one used in this thesis, consists of:

- a graded-index FMF (which injects the free-space field into the MPLC);
- a reflective multi-plane conversion module (sequence of phase plates);
- an array of SMF outputs, each associated to a specific spatial mode.

The free-space field collected by a collimator is coupled into the FMF, which acts as an interface between the turbulence-distorted optical beam and the MPLC. Inside the MPLC, the field undergoes successive reflections, each applying a phase mask $\phi_k(x, y)$. After the final plane, the modal components are spatially separated and coupled into distinct SMFs.

The MPLC therefore performs a deterministic projection of the received beam onto an orthogonal mode basis. In the experimental setup, the MPLC is used exclusively as a

Figure 2.5: Photograph of the MPLC device (Proteus, Cailabs) used in this thesis, featuring 1 FMF input and 10 SMF outputs.

receiver-side mode demultiplexer. The functional chain is:

1. turbulent free-space beam collected by the collimator;
2. coupling into a FMF feeding the MPLC;
3. spatial demultiplexing into HG modes by MPLC;
4. SMF outputs feeding the Waveshaper (for frequency selection) or fast optical power meters.

The device used in this thesis is the Proteus MPLC developed by Cailabs. Its key specifications are:

- 1 FMF input (supporting HG-like spatial distributions);

- 10 SMF outputs, each mapped to a specific HG mode;
- optimized for wavelengths around 1550 nm;
- static, no moving parts, highly stable over time.

The MPLC offers several unique advantages when used as a receiver in turbulent FSO systems:

- high modal selectivity: ideal for distinguishing turbulence-induced modal content;
- compatibility with free-space HG modes: unlike PLs, which are optimized for LP modes in fiber;
- low sensitivity to input polarization;
- enables modal diversity: different modes carry partially uncorrelated fading;
- unitary transformation: preserves field information for coherent combining.

These properties make the MPLC a superior tool for receiver-side turbulence mitigation and spatial-mode analysis.

2.2.4 Summary

To summarize the key differences between the three receiving architectures discussed above, Table 2.1 provides a comparative overview of their main properties and limitations.

Table 2.1: Comparison of the three demultiplexing devices considered in this thesis.

Feature	**SMF**	**PL**	**MPLC**
Modes	Fundamental mode only	Typically 2–6	≥ 10
Mode selectivity	N/A	Moderate	High selectivity
Polarization sensitivity	High	Moderate	Low
Insertion loss	Intrinsic fiber coupling loss only	Moderate; depends on taper quality and splice losses	Mode dependent
Response to turbulence	Very poor	Medium, it captures a few modal projections	Excellent — decomposes the distorted wavefront into several orthogonal spatial modes
Application in this thesis	Baseline reference receiver	Benchmark tool for LP-mode reception	Main device for modal decomposition and diversity combining
Advantages	Simple, low-loss, robust, widely available	Compact multimode-to-multicore mapping	High mode count, low crosstalk, general modal transformations, turbulence robustness

2.3 Atmospheric Turbulence in FSO Links

Atmospheric turbulence is one of the dominant impairments affecting coherent FSO communication systems. It originates from random refractive-index fluctuations in the atmosphere caused by temperature gradients, pressure variations, and wind-induced mixing of warm and cold air masses. These fluctuations introduce random amplitude, phase, and wavefront distortions on the propagating laser beam, leading to well-known effects such as scintillation, beam wander, beam spreading, and wavefront corrugation. Together, these impairments can strongly degrade coherent detection and significantly limit link stability.

In this thesis, turbulence is treated not as an abstract theoretical disturbance but as a controllable and measurable phenomenon. A thermal atmospheric chamber is used to emulate realistic turbulence conditions, while the Rytov variance provides a physically meaningful quantification of turbulence strength. Both tools were validated in prior work on fiber-coupled FSO links—notably in [6]—and serve as cornerstones of the experimental methodology adopted in later chapters.

The following sections describe the operating principles of the atmospheric chamber used in the experiments and introduce the Rytov variance as a robust metric for characterizing turbulence-induced fading.

2.3.1 Atmospheric Chamber

The experiments conducted in this thesis employ a thermal atmospheric chamber specifically designed to generate controlled and repeatable turbulence conditions. The setup follows the architecture demonstrated and validated in [6], where two thermally regulated chambers are arranged in series. By imposing a stable temperature gradient between them, refractive-index fluctuations are generated that emulate the weak-to-moderate turbulence typical of short-range FSO links.

The atmospheric chamber operates through the following mechanisms:

1. thermal gradient and refractive-index fluctuations: a temperature difference between the hot and cold chambers induces convection-driven mixing of air; producing random refractive-index perturbations.
2. realistic distortion of the optical beam: as the beam propagates through the chamber, it experiences scintillation, centroid displacement, and wavefront distortions consistent with weak–moderate atmospheric turbulence;
3. Repeatability and stability: for fixed thermal settings, the turbulence statistics remain highly repeatable, an essential requirement for comparing different receiver architectures under identical turbulence regimes, as emphasized in [6];
4. Relevance to fiber coupling: since the receiver employs fiber coupling (SMF or FMF), the chamber is particularly suitable because the induced distortions translate directly into power fluctuations and coupling efficiency variations.

This controlled environment makes the chamber ideal for studying modal decomposition and modal diversity, since different spatial modes react differently to turbulence-induced distortions. Two of the chamber shown in Figure 2.6 are used throughout this thesis for all turbulence-impaired measurements, ensuring consistency and reproducibility across experiments.

2.3.2 Rytov Variance

The Rytov variance is one of the most widely adopted metrics for quantifying turbulence strength in optical propagation. It expresses the variance of log-amplitude fluctuations induced by refractive-index inhomogeneities. For plane-wave propagation, it is given by:

$$\sigma_R^2 = 1.23\, C_n^2\, k^{7/6}\, L^{11/6}, \tag{2.16}$$

where:

- C_n^2 is the refractive-index structure constant;
- $k = 2\pi/\lambda$ is the wavenumber;

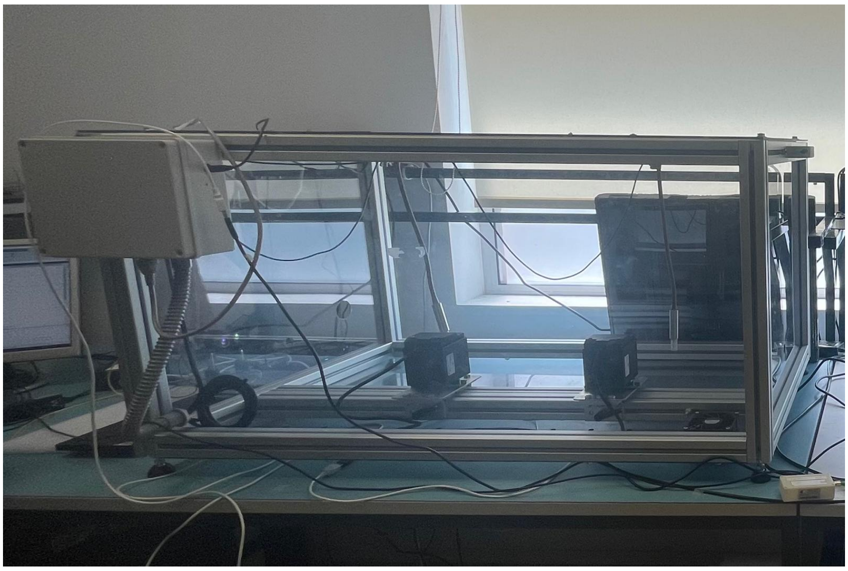

Figure 2.6: Atmospheric turbulence emulator used in the experimental campaign. In this work it is an atmospheric chamber.

- L is the propagation distance.

The value of σ_R^2 provides a clear classification of turbulence regimes:

- $\sigma_R^2 < 1$: weak turbulence;
- $1 < \sigma_R^2 < 4$: moderate turbulence;
- $\sigma_R^2 > 4$: strong turbulence.

In fiber-coupled FSO systems, the Rytov variance correlates strongly with the statistics of received optical power, because coupling efficiency is highly sensitive to amplitude distortions and low-order wavefront aberrations.

The work in [6] demonstrated that, for thermally induced turbulence:

- the temporal statistics of scintillation match theoretical predictions for weak–moderate turbulence;
- the estimated Rytov variance remains stable across repeated measurements;
- the metric correlates well with system-level performance indicators such as BER and SNR.

Thus, the Rytov variance is not only physically meaningful but also experimentally practical.

Since C_n^2 cannot be measured directly in the chamber, the Rytov variance is estimated from the normalized received power $I(t)$ as:

$$\sigma_R^2 \approx \ln\left(1 + \frac{\mathrm{Var}[I(t)]}{\mathrm{E}[I(t)]^2}\right), \tag{2.17}$$

which is the same estimator adopted in [6]. This makes the Rytov variance directly comparable across all receiver architectures investigated in following chapters.

The Rytov variance plays several key roles in this thesis:

- it quantifies the turbulence strength for each experiment;
- it validates the repeatability of the atmospheric chamber;
- it enables fair comparison between SMF, PL, and MPLC reception;
- it provides physical insight into why different spatial modes exhibit different fading behaviors.

Overall, the Rytov variance provides a rigorous framework connecting turbulence physics to communication performance, forming an essential foundation for the analyses presented in Chapters 4 and 5.

2.4 Coherent Optical Transmission System

Coherent optical communication is the current standard for high-capacity fiber links and is increasingly adopted for FSO systems. Unlike direct detection, coherent reception preserves amplitude and phase, enabling the use of advanced modulation formats (e.g., QAM), digital dispersion compensation, and powerful adaptive equalization techniques. In turbulence-impaired FSO channels, these capabilities are particularly advantageous: despite scintillation, beam wander, and random phase distortions, coherent detection maintains access to the full complex field, enabling robust digital compensation. In contrast to the power-only measurements of Chapter 4, the experiments will employ a complete coherent transmission chain. The optical waveform is digitally synthesized, pulse-shaped, and uploaded to a high-speed Arbitrary Waveform Generator (AWG). The electrical signals generated by the AWG drive a dual-polarization I/Q modulator, producing a 16-QAM waveform. A booster Erbium-Doped Fiber Amplifier (EDFA) increases the launch power before propagation through the atmospheric chamber. At the receiver, the distorted signal received after the atmospheric chamber is pre-amplified by a low-noise EDFA, detected by a coherent receiver, and processed by a dedicated Digital Signal Processing (DSP) chain including clock recovery, equalization, carrier-frequency and carrier-phase estimation, and symbol decoding.

This framework allows full evaluation of SNR, BER, and Normalized Generalized Mutual Information (NGMI) under different reception strategies and ultimately enables the modal-diversity experiments presented later.

2.4.1 16-QAM Modulation

In this work, the transmitted waveform is based on square 16-ary quadrature amplitude modulation (16-QAM), a widely adopted format in coherent optical systems because it offers a good compromise between spectral efficiency and implementation complexity. Each symbol carries 4 bits and is mapped onto the in-phase (I) and quadrature (Q)

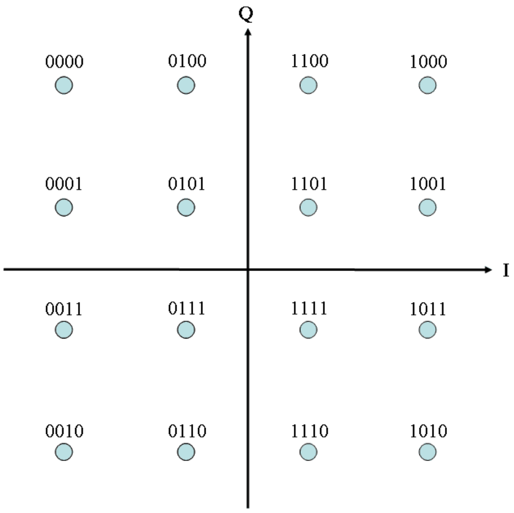

Figure 2.7: Example of a square 16-QAM constellation used in coherent optical communication with highlighted the Gray code bit mapping.

components of the complex optical field, forming a Cartesian constellation of equally spaced points.

Before digital-to-analog conversion, the symbols are pulse-shaped with a Root Raised-Cosine (RRC) filter with a given roll-off coefficient, to limit potential crosstalk with adjacent channels. The signal is generated offline with a sampling rate that matches the capabilities of the Keysight M8194A AWG used in the transmitter. A pilot-symbol structure is included to improve DSP convergence, particularly for carrier-phase estimation under turbulence. Forward-error correction is disabled, so the BER and NGMI measurements presented in this thesis correspond to uncoded performance.

The digital I/Q streams drive a dual-polarization modulator, generating optical 16-QAM waveform. After modulation, a booster EDFA raises the launch power to the required level before propagation through the atmospheric chamber. An illustration of a square 16-QAM constellation is reported in Figure 2.7.

2.4.2 Single-Carrier vs. Subcarrier Multiplexing

In coherent optical communication systems, information can be transmitted either using a single wideband carrier or by distributing the signal across multiple radio-frequency subcarriers. These two approaches, commonly referred to as Single-Carrier (SC) modulation and Subcarrier Multiplexing (SCM), differ significantly in terms of spectral structure and sensitivity to channel impairments. This section provides an overview of both schemes to clarify their operating principles and motivate the use of SCM in turbulence-affected FSO links.

Single-Carrier Modulation

In a SC system, the entire data stream modulates a single optical carrier using formats such as QAM. After digital pulse shaping the baseband signal directly drives the optical modulator. The resulting spectrum is compact and occupies a single continuous band around the carrier.

SC systems are simple and spectrally efficient, but they may be more vulnerable to wideband fading. In the presence of atmospheric turbulence, a deep fade or strong phase distortion can affect the whole signal bandwidth simultaneously, significantly degrading link performance.

Subcarrier Multiplexing

SCM extends the SC approach by distributing the information across multiple subcarriers. Each subcarrier is pulse-shaped, frequency-shifted and then summed to produce a multi-band electrical signal. The optical modulator maps this composite waveform onto the optical domain, generating several narrow sub-bands around the carrier.

SCM offers several advantages:

- **Resilience to fading:** turbulence-induced fluctuations affect individual subcarriers with only partial correlation, enabling frequency-domain diversity.
- **Flexibility:** each subcarrier can be independently weighted, enabled, or disabled to adapt to channel conditions.

In this thesis, SCM is not used to increase capacity but to introduce redundancy for diversity purposes. The same information block is replicated across four subcarriers. Because each subcarrier experiences partially uncorrelated turbulence-induced fading, their independent replicas can be combined at the receiver to mitigate deep fades and stabilize the received power. This diversity mechanism increases robustness at the cost of reduced spectral efficiency, since part of the available bandwidth carries redundant information.

Comparison

The fundamental difference between SC and SCM lies in how signal energy is distributed across the spectrum. SC concentrates all information into a single band, making the transmission more exposed to wideband fading. In contrast, SCM spreads the signal across multiple narrower sub-bands, reducing the probability that all components are simultaneously affected by turbulence impairments. This property makes SCM particularly attractive for free-space links where turbulence induces frequency-dependent distortions.

2.4.3 Digital Signal Processing in Coherent Optical Systems

Digital coherent receivers rely on a sophisticated DSP chain to recover the transmitted symbols in the presence of chromatic dispersion, phase noise, frequency offset, nonlinear distortions, and—in the context of this thesis—turbulence-induced impairments from the

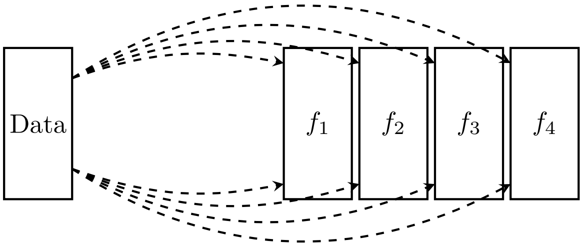

Figure 2.8: Conceptual representation of the SCM-based diversity scheme. A single data stream is copied and digitally upconverted onto four independent subcarriers (f_1–f_4), each experiencing partially uncorrelated fading.

FSO channel. The general DSP architecture adopted here follows the functional structure presented in [20], adapted to the specific characteristics of the experimental setup and to the particularities of modal diversity processing introduced in Chapter 5.

General DSP Architecture

A coherent optical receiver samples the in-phase and quadrature components of the received field and processes them digitally through a sequence of blocks designed to progressively undo channel and hardware impairments. Although individual implementations may differ in the number of internal stages, the overall DSP pipeline is conceptually organized into the following major modules:

(1) Front-End Preprocessing This stage prepares the sampled waveforms for further processing and includes:

- resampling to the desired samples-per-symbol ratio;
- IQ and polarization deskew to compensate for differential delays between tributaries due to hardware implementation imperfections;
- DC removal to eliminate detector-induced offsets;
- optional Gram–Schmidt orthonormalization to correct IQ imbalance or front-end mixing imperfections.

These operations ensure that the received samples occupy a well-conditioned representation of the optical field before equalization and synchronization.

(2) Matched Filtering and Coarse Timing Alignment Pulse-shaping filters at the transmitter are inverted by a corresponding matched filter—typically a RRC—which maximizes the signal-to-noise ratio. Coarse timing alignment is then performed to place the sampling instant within the region of maximum eye opening.

(3) Static Equalization A static finite-impulse-response filter compensates for deterministic distortions such as bandwidth limitations or group-delay variations. While chromatic dispersion is negligible in the short-fiber paths of an FSO link, this block serves as a linear stabilization stage that prepares the signal for adaptive equalization.

(4) Adaptive Equalization The adaptive equalizer is typically based on a 2×2 MIMO structure in polarization-multiplexed systems. In this work, the equalizer compensates for residual front-end distortions and turbulence-induced amplitude and phase fluctuations. Blind or data-aided algorithms (LMS, CMA, or decision-directed schemes) iteratively adapt the filter coefficients to track channel variations.

(5) Carrier Recovery Carrier-frequency and carrier-phase recovery are performed in two steps:

- frequency-offset estimation to remove residual frequency mismatch between transmitter and LO;
- phase recovery (e.g., Viterbi–Viterbi or blind-phase-search) to track fast phase noise and slow drifts.

These operations restore the correct constellation orientation before symbol detection.

(6) Fine Timing and Frame Synchronization Fine symbol timing ensures that the sampling instant is optimally placed after equalization. Frame alignment—relying on pilots or data-aided correlation—aligns the received sequence with its transmitted counterpart for performance evaluation.

(7) Soft Demapping and Performance Estimation Finally, the equalized symbols are converted into log-likelihood ratios (LLRs) through a soft demapper. This allows computing the BER, Generalized Mutual Information (GMI), and the NGMI, which quantify post-Forward Error Correction (FEC) performance margins. This modular DSP framework provides the foundation for all experimental results reported in this thesis, including the multi-carrier modal-diversity experiments described next.

2.4.4 DSP Extensions for Multi-Carrier Modal Diversity

In the final experimental configuration, four subcarriers carrying identical data are launched through a SMF and later separated at the receiver by the MPLC and a Waveshaper. Each subcarrier predominantly couples to a different Hermite–Gaussian mode, providing four partially uncorrelated replicas of the same waveform.

The DSP chain extends naturally to this multi-carrier scenario: after per-subcarrier processing, the branches are combined through a MISO equalizer that coherently fuses the four replicas of the same transmitted sequence. The MISO equalizer performs a combination of the four branches, exploiting the fact that turbulence-induced fading affects the spatial projections of the field differently. Because the four subcarriers correspond to the four selected modes, the receiver can dynamically select any subset of branches—for example, two, three, or all four— and evaluate the incremental diversity gain. This architecture is conceptually simple but powerful:

- it requires only one coherent receiver;
- it leverages the orthogonality of the MPLC modes to extract complementary information from the distorted wavefront.

The performance improvements observed in Chapter 5—higher SNR stability, consistently higher NGMI, and significantly reduced BER spikes—originate directly from this DSP-enabled modal diversity mechanism.

Chapter 3

MPLC Characterization

This chapter presents the experimental characterization of the MPLC used for mode multiplexing in FSO communication systems. The primary objective is to evaluate the performance of the MPLC in terms of insertion loss, polarization effects and mode correlation.

A thorough characterization is essential to compare the MPLC with a conventional photonic lantern, aiming to identify potential advantages such as improved mode separation, reduced modal crosstalk, and enhanced overall performance. Highlighting these benefits is crucial for demonstrating the MPLC's suitability in advanced multimode optical communication scenarios.

3.1 Basic Description and Key Specification of the Mode-Multiplexing Devices

The MPLC employed in this study, presented in Figure 3.1a is a space division multiplexer manufactured by Cailabs. The specific model used is the PROS_10_0002_1550, designed to multiplex 10 modes for optical communication applications. The device operates optimally at a wavelength of $\lambda = 1550$ nm, a standard choice in optical communications due to low fiber attenuation. The MPLC features standard LC/PC connectors for SMF interfaces, ensuring compatibility with common telecom-grade fiber equipment. The single-mode fibers used on the device outputs are typical SMF fibers, while the multimode fiber input is specified as type 6PLGI on the datasheet given by Cailabs.

For what concerns the photonic lantern, presented in Figure 3.1b the device employed in this work is a three-mode fiber-based lantern specifically designed to demultiplex the fundamental and first higher-order linearly polarized modes of a weakly guiding fiber. In particular, it provides spatial separation of the modes LP_{01} and the two degenerate components LP_{11a} and LP_{11b}, which constitute the primary modal set supported by few-mode fibers at $\lambda = 1550$ nm.

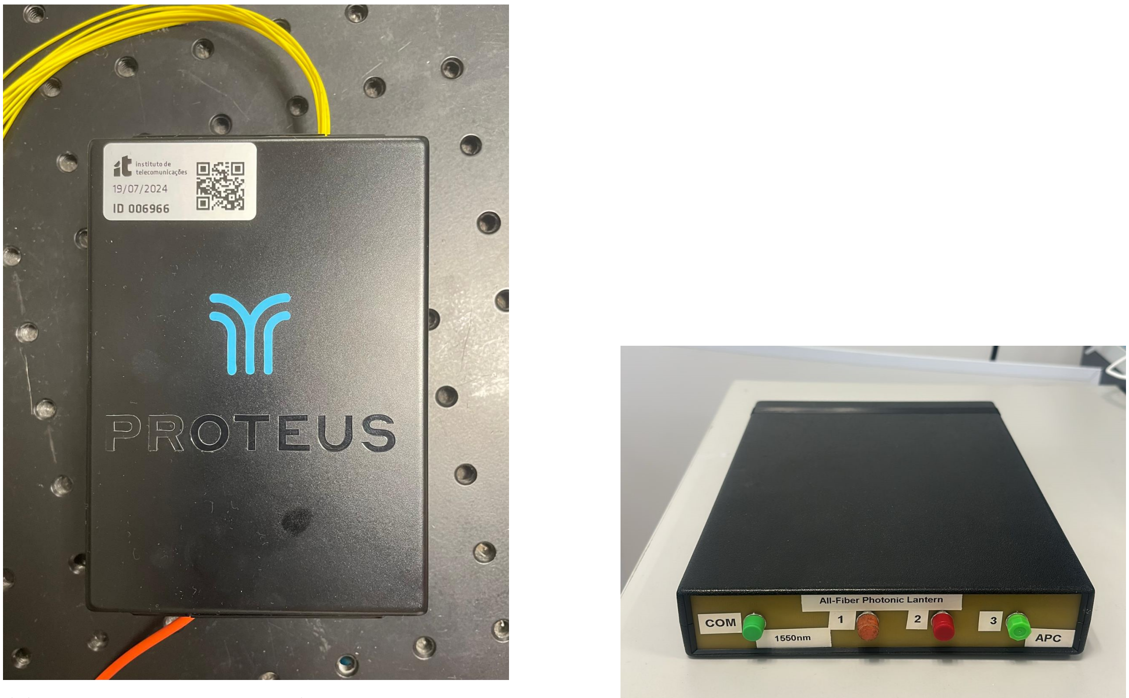

(a) MPLC device (Cailabs, model PROS_10_0002_1550) used during the experimental characterization.

(b) PL device used in this thesis, featuring 1 FMF input and 3 SMF outputs.

Figure 3.1: Mode multiplexing devices.

3.2 Characterization of Insertion Loss

The experiments, with the setup depicted in Figure 3.2, have been conducted with the following conditions:

Parameter	**Value** heightSource
DFB laser at $\lambda = 1554.130$ nm Input power	$P_{in} = 4$ dBm
Power after Polarization Controller	$P = 3.49$ dBm

Note: the power is constant with respect to polarization. Despite different states of polarization, the power at the device input remains the same.

To measure the insertion loss, the logarithmic relationship between input and output power was used:

$$\text{IL}[\text{dB}] = P_{\text{in}}[\text{dBm}] - P_{\text{out}}[\text{dBm}]$$

with:

- $P_{\text{in}}[\text{dBm}]$: optical power measured after the polarization controller
- $P_{\text{out}}[\text{dBm}]$: optical power measured at the output of the device under test

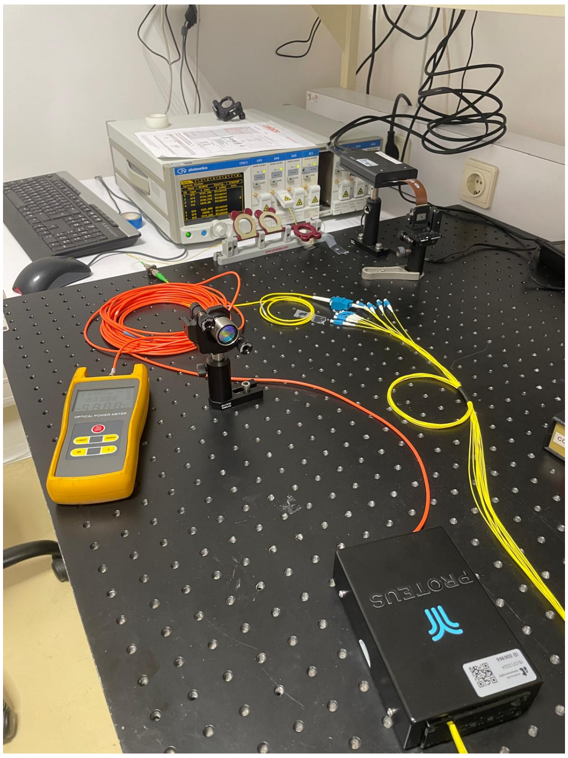

Figure 3.2: Setup for the characterization of the insertion loss. In the photograph the MPLC is characterized. Same setup is used for the photonic lanter.

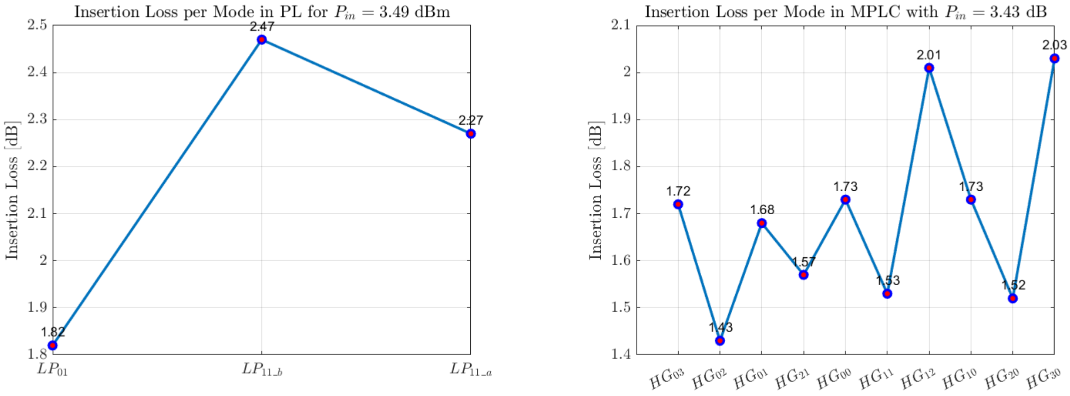

(a) PL: the mean IL is 2.2 dB

(b) MPLC: the mean IL is 1.7 dB

Figure 3.3: Comparison of insertion loss for the photonic lantern and the MPLC.

The insertion loss has been investigated against the 3 modes; the ports are, respectively, $LP_{01}, LP_{11_a}, LP_{11_b}$. For the MPLC, the insertion loss was investigated against the 10 modes. The results are presented e compared in Figure 3.3. As can be seen in Figure 3.3a, the insertion loss of the PL devices varies from ∼1.8 dB to ∼2.5 dB, with the

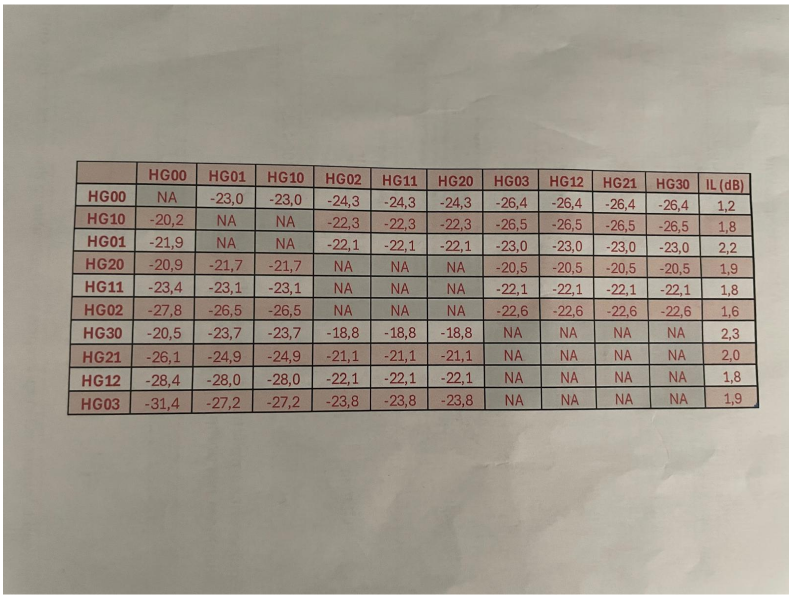

	HG00	HG01	HG10	HG02	HG11	HG20	HG03	HG12	HG21	HG30	IL (dB)
HG00	NA	-23,0	-23,0	-24,3	-24,3	-24,3	-26,4	-26,4	-26,4	-26,4	1,2
HG10	-20,2	NA	NA	-22,3	-22,3	-22,3	-26,5	-26,5	-26,5	-26,5	1,8
HG01	-21,9	NA	NA	-22,1	-22,1	-22,1	-23,0	-23,0	-23,0	-23,0	2,2
HG20	-20,9	-21,7	-21,7	NA	NA	NA	-20,5	-20,5	-20,5	-20,5	1,9
HG11	-23,4	-23,1	-23,1	NA	NA	NA	-22,1	-22,1	-22,1	-22,1	1,8
HG02	-27,8	-26,5	-26,5	NA	NA	NA	-22,6	-22,6	-22,6	-22,6	1,6
HG30	-20,5	-23,7	-23,7	-18,8	-18,8	-18,8	NA	NA	NA	NA	2,3
HG21	-26,1	-24,9	-24,9	-21,1	-21,1	-21,1	NA	NA	NA	NA	2,0
HG12	-28,4	-28,0	-28,0	-22,1	-22,1	-22,1	NA	NA	NA	NA	1,8
HG03	-31,4	-27,2	-27,2	-23,8	-23,8	-23,8	NA	NA	NA	NA	1,9

Figure 3.4: Table given in the datasheet. The last column has the insertion loss provided by the manufacturer.

fundamental mode (LP_{00}) yielding 0.5–0.7 dB lower loss than the LP_{11} modes. In turn, the MLPC, as presented in Figure 3.3b, show a similar insertion loss in the fundamental mode (HG_{00}) but significantly reduced attenuation in the higher-order modes, with a maximum of ∼2 dB loss of the HG_{12} and HG_{30} modes, only ∼0.3 dB higher than the fundamental mode. Interestingly, the minimum insertion loss of the device is found at roughly 1.4–1.5 dB for the HG_{02}, HG_{21}, HG_{11} and HG_{20} modes.

The results of the MPLC were compared also with the last column given in the datasheet in Figure 3.4 and are found to be quite similar.

The experimental results highlight a significant improvement in the insertion loss performance when using the MPLC compared to that of the PL. This reduction of roughly 0.5 dB in terms of maximum insertion loss demonstrates the superior efficiency of the MPLC in mode coupling, making it a more suitable candidate for applications in mode-division multiplexed systems, especially in scenarios where minimizing power loss is critical.

Furthermore, the MLPC device provides support to a larger set of modes (10 modes) compared to the PL (3 modes), which can be advantageous to improve the coupling efficiency under severe turbulence effects. For those reasons, we will henceforth mainly focus the analysis on the MPLC device, using the PL as a comparison benchmark.

3.3 Characterization of Polarization Stability

Concerning the beam profile, it has been observed that, for some modes, it changes significantly with the polarization; in particular, in Figure 3.5 the mode HG_{03}, which is the most affected by the state of polarization, is presented in three different states and compared to the theoretical beam. This behaviour underlines the necessity to further

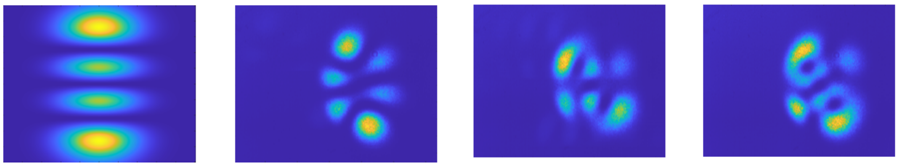

Figure 3.5: Comparing the theoretical shape of the HG$_0$3 mode (left) with three different acquired beam profiles obtained for different polarization perturbations applied manually (right).

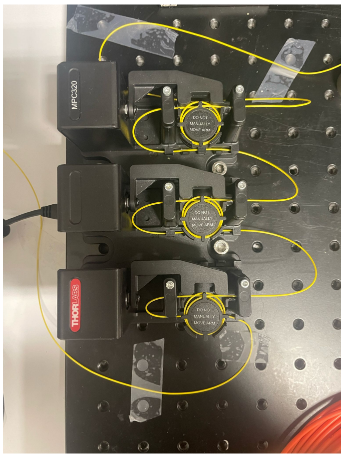

Figure 3.6: Photo of the Thorlabs motorized polarization controller (MPC320) utilized in this work.

investigate the impact of polarization on the system's performance. While the second beam (from left to right) in Figure 3.6 is the one that better approximates the theoretically expected shape for the HG$_0$3 mode, an improved polarization control might be needed to better match with the ideal mode distribution.. In order to gain finer control and enable systematic characterization of this effect, a Motorized Polarization Controller (MPC) was integrated into the setup. The following section describes its role and the methodology adopted to analyze the polarization-dependent behavior of the MPLC.

3.3.1 Motorized Polarization Controller

In the previous setup, the manual polarization controller is replaced with the Thorlabs MPC320 motorized polarization controller [21] in Figure 3.6 . The motorized polarization controller uses stress-induced birefrigence to alter polarization in a single-mode fiber that is looped around three independent spools to create three independent fractional wave plates [21]. To transform an arbitrary input polarization state into a fixed and defined output polarization state, the controller uses a combination of three paddles as a quarter-wave plate, half-wave plate and quarter-wave plate; to obtain this configuration, there are two loops in the first paddle, three loops in the second paddle, and two loops in the third paddle. The retardance of each paddle may be estimated from the following equations [21]:

$$\phi(\text{rad}) = \frac{2\pi^2 a N d^2}{\lambda D} \tag{3.1}$$

where:

- ϕ: retardance
- $a = 0.1333$ for silica fiber. The parameter a represents an empirical coefficient that quantifies how efficiently the mechanical stress induced by bending is converted into birefringence in an optical fiber. When the fiber is curved or wound into loops, the cladding undergoes mechanical deformation, which generates stress-induced birefringence. The coefficient a therefore expresses the sensitivity of the fiber to this deformation.
- N: number of loops
- d: fiber cladding diameter
- λ: wavelength
- D: loop diameter

The device insertion loss has been measured:

- $P_{in} = 6$ dBm
- $P_{out} = 3.80$ dBm
- $IL = P_{in} - P_{out} = 6 - 3.80 = 2.20$ dB

This loss can be partially attributed to the way the device controls polarization by mechanically deforming the fiber in a controlled manner. If the fiber bends are too tight or not properly managed, additional losses due to bending can occur. These bending losses happen because the optical field can leak out of the fiber core in curved regions, contributing to the overall insertion loss observed.

The control software was implemented in MATLAB. Since each controller offers 170° of movement [21], a simple script was developed to iterate over angle combinations. This approach enables the exploration of various paddle configurations in order to identify the optimal polarization state for each mode. Recalling mode HG_{03}, significantly improved experimental images were found as shown in Figure 3.7 . The motorized polarization controller is essential for two main reasons. Firstly, it enables a precise investigation of the polarization behavior by offering full control over the paddle angle combinations. Secondly, it ensures the repeatability of the experiment as specific angle configurations can be saved and reliably reproduced in future measurements.

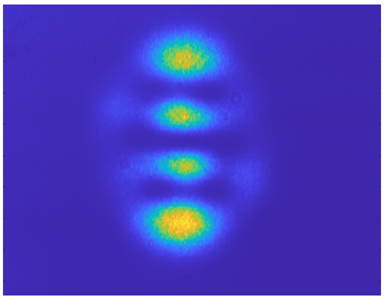

Figure 3.7: Improved retrieval of the HG$_0$3 mode from the MPLC by employing fine polarization control using a motorized controller. The depicted beam profile has been achieved by setting the three paddles of the polarization controller to 0º, 50º and 50º, respectively.

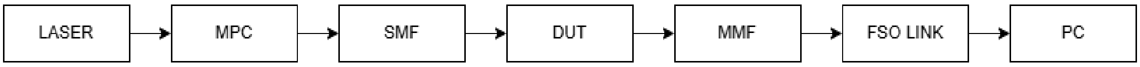

Figure 3.8: block scheme

3.3.2 First Experimental Assessment of the Impact of Polarization on Transmitted Beam Profiles

Setup

The laser used is a Distributed Feedback Laser (DFB) laser operating at $\lambda = 1554.130$ nm, which is connected to an OS2 9/125 SMF looped around the MPC in the configuration previously described. Here, there is the distinction depending on the DUT used in multiplexing mode: for what concerning the PL, there are three input ports, each one associated to a different mode:

- port 1: fundamental mode
- port 2: LP_{11b}
- port 3: LP_{11a}

On the other hand, the input of the MPLC is a SMF array with different input channels, 10 in this analysis. At the DUT output a few-mode fiber (FMF) (the orange one at the MPLC output in Figure . 3.9) that supports different spatial modes is used. The FSO link consists of one fiber collimator (Thorlabs F810APC-1550) at the transmitter side and a lens (Thorlabs LMR2/M) plus the Duma Optronics BeamOn Complete system [22] at 30 cm of distance. Images are collected directly on the PC using *BeamOnUSB* software integrated in a MATLAB script to acquire and store the images. The main goal of this experiment is to observe and validate the sensitivity of the modes to the polarization state and, if applicable, identify any interesting trends to better understand the relationship between polarization and mode behavior.

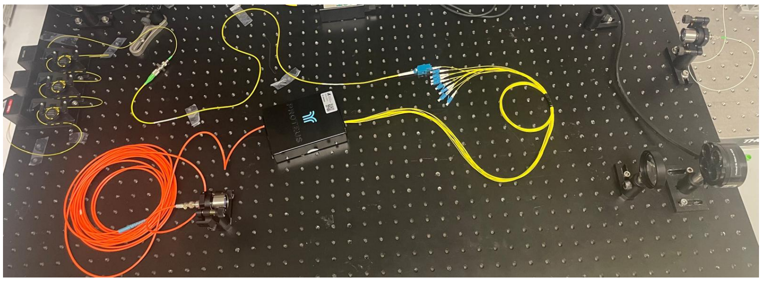

Figure 3.9: Complete fiber to free-space transmission setup using the MLPC to set the transmitted modes.

Pseudo-Code

In this initial stage, only the sensitivity of each mode to polarization was investigated. A limited number of images per mode were collected. To clarify the process, the following pseudo-code summarizes the MATLAB implementation:

Algorithm 1: MPC controller algorithm

```
for $a_1 = 5$ to $165$ $\Delta a$ do
    for $a_2 = 5$ to $165$ $\Delta a$ do
        for $a_3 = 5$ to $165$ $\Delta a$ do
            Set angles $(a_1, a_2, a_3)$;
            Take image;
            Store image;
        end
    end
end
```

A step size of $\Delta\theta = 40$ was chosen between the different a_n, the angles of the three MPC paddles, resulting in 5 discrete values per paddle, $\theta = [5°, 45°, 85°, 125°, 165°]$, and hence 125 angle combinations. Consequently, 125 images were acquired for each mode. The collection process for a single mode took approximately 20 minutes.

Results

As a metric for the sensitivity to polarization, the visual dispersion was evaluated. For each mode, all 125 images acquired at different polarization states were summed in absolute values, normalized, and compared to the theoretical mode profile. This approach provides a qualitative indication of how the shape of the beam varies with polarization and helps to identify which modes are most affected.

Photonic Lantern

In the case of the PL, the analysis focused on the higher-order modes LP_{11a} and LP_{11b}. The experimental results clearly show that these modes are highly sensitive to the state

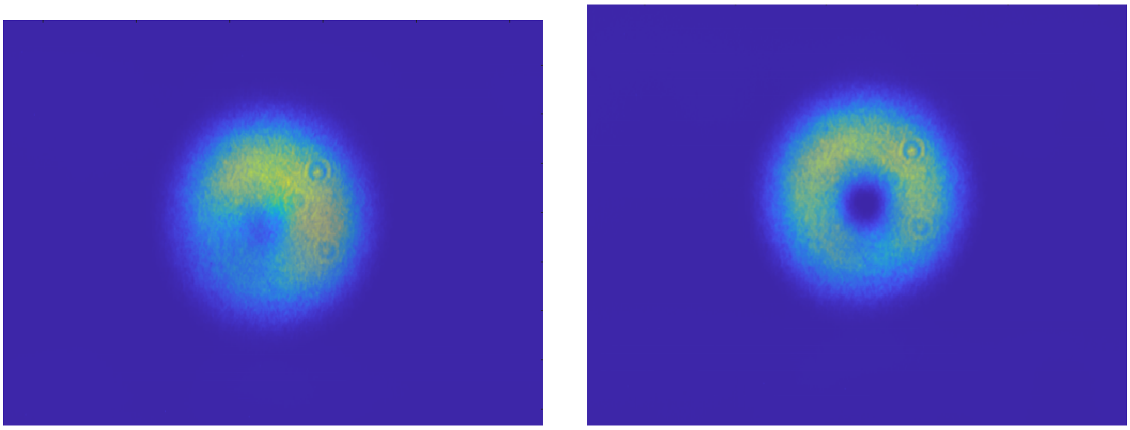

Figure 3.10: Obtained average beam profiles across all tested polarization states for the LP11a (left) and LP11b (right) modes using the PL device.

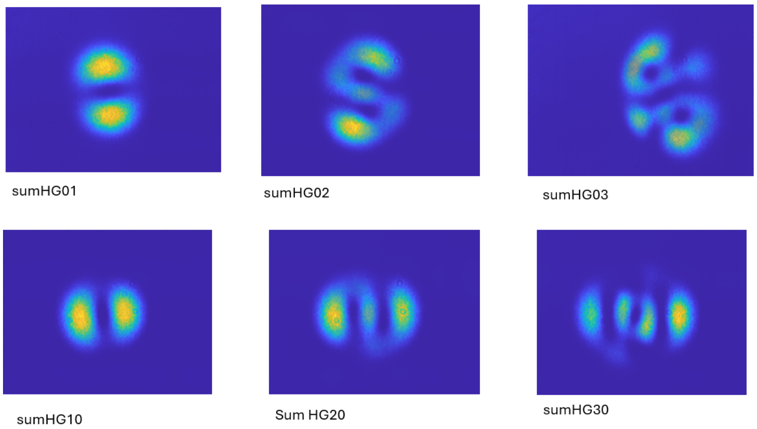

of polarization. In fact, almost every one of the 125 polarization combinations produces a different beam profile, often quite far from the expected theoretical shape. When these images are summed, the resulting beam appears significantly spread, confirming that polarization plays a crucial role in the behavior and stability of these modes.

Multi Plane Light Converter

From Figure 3.11, it can be concluded that the modes HG_{10} and HG_{01} exhibit negligible sensitivity to polarization, as their beam profiles remain consistent across different states. For modes HG_{20}, HG_{11}, HG_{02}, and HG_{30}, the overall behavior is satisfactory and closely matches the theoretical shape; however, certain polarization states cause significant deviations in the beam profile. In contrast, the modes HG_{03}, HG_{12}, and HG_{21} show a strong dependence on the polarization state. Their profiles often diverge significantly from the expected shape, appearing highly distorted and spatially spread. This highlights the necessity of identifying the optimal polarization state, potentially by reducing the step size

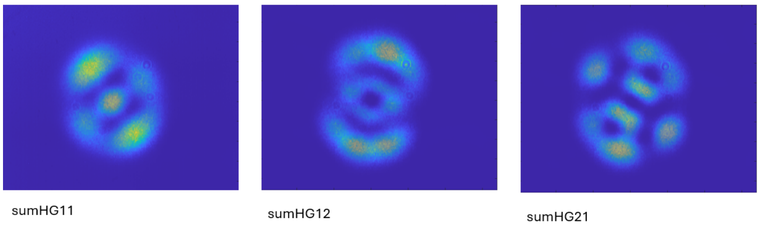

sumHG11 sumHG12 sumHG21

Figure 3.11: Obtained average beam profiles across all tested polarization states for the HG modes modes supported by the MPLC device.

in the angle sweep and by acquiring additional information such as the Stokes parameters and the corresponding point on the Poincaré sphere.

However, as expected, the MPLC exhibits a more robust response to polarization variations compared to the PL. Although the PL shows strong sensitivity, where virtually all polarization states result in significantly distorted beams, the MPLC behaves much more consistently. Several modes appear quite insensitive to the polarization and even the more affected ones maintain a resonable resemblance to the theoretical profiles. These observations confirm the anticipated advantage of the MPLC in terms of polarization tolerance. Although not completely immune, its superior performance makes it a more reliable and effective solution for mode multiplexing applications where polarization fluctuations are unavoidable.

3.3.3 Impact of Fiber Bending

To investigate the sensitivity of the mode propagation to mechanical deformations, a series of measurements were performed by keeping the polarization controller fixed while physically changing the shape of the fiber. Specifically, the same input mode and polarization configuration were used, and only the position and bending radius of the fiber were varied, either by slightly shifting the fiber path or by increasing the tightness of its coiling.

The resulting beam profiles showed a significant dependence on the fiber's mechanical configuration: despite identical input conditions in terms of laser wavelength and polarization, the output patterns changed noticeably with different fiber bends. This confirms that bending induces mode coupling and alters the effective propagation constants of the supported modes, ultimately affecting the spatial distribution at the output. The presented images in Figure 3.12 illustrate this effect, highlighting how variations in fiber placement or coiling can distort or redistribute the beam intensity. In this example the input mode is HG_{21} with the MPC in the configuration: $P_1 = 20°$, $P_2 = 160°$, $P_3 = 160°$

In light of these results, it is important to emphasize that the beam profile measurements are strictly valid for the specific fiber configuration and setup used during the acquisition. Variations in the fiber's position or curvature can significantly alter the observed profiles, underlining the need for a consistent experimental setup when comparing polarization-dependent effects.

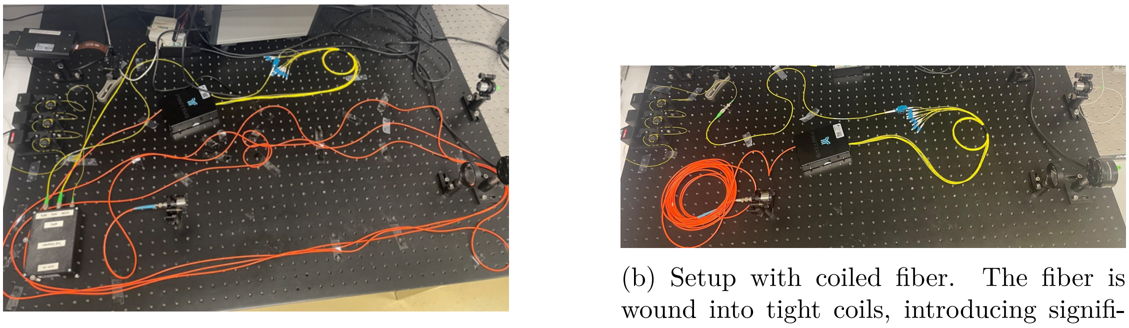

(a) Setup with mildly bent fiber.

(b) Setup with coiled fiber. The fiber is wound into tight coils, introducing significant bending.

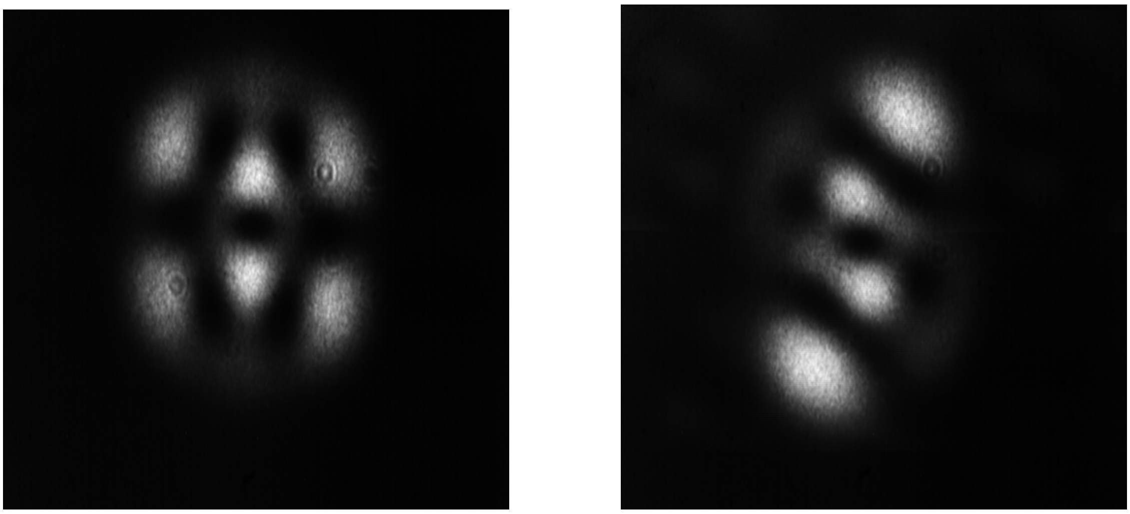

(c) Beam profile with mildly bent fiber. The beam profile shows a symmetric and well-defined distribution.

(d) Beam profile with coiled fiber. The beam profile exhibits distortions and an altered intensity distribution.

Figure 3.12: Comparison of the setups and corresponding beam profiles for the linear and coiled fiber configurations.

3.3.4 Polarimeter

In this work, different states of polarization were investigated in order to analyze their impact on the measured beam profiles. Moreover, a controlled and repeatable method was required to ensure that all measurements could be reliably compared.

The PAX5720VIS-T polarimeter is a terminating wave plate-based that modulates for free space and fiber-based measurements of the State of Polarization (SOP) [23]. All four Stokes values, which fully characterize an SOP, are provided either as analog output voltages or as digital values to the PC [23]. The polarimeter analyzes the state of polarization and the degree of polarization of optical signals in either free space or optical fibers. The resulting data can be viewed using the Graphical User Interface and are presented in a number of forms, on the Poincaré sphere, or as Stokes parameters [24] and visualized on the given PC as shown in Figure 3.13. The first test was to simply

Figure 3.13: Polarimeter and PC. Image adapted from Thorlabs datasheet [24].

connect the polarimeter to the MPC in order to follow the SOP on the Poincaré sphere and the Stokes parameters evolution depending on the MPC paddles in order to find some correlation. The first idea was to move one paddle at a time to see the effect on the sphere and what kind of rotation it generates and if there is any kind of relationship. To enable the communication between MATLAB and the polarimeter, the NI USB-6009 Data Acquisition (DAQ) device was employed. The NI USB-6009 is a multifunction DAQ module produced by National Instruments that provides analog and digital I/O capabilities through a USB interface. In this setup, the USB-6009 acts as an intermediary that allows MATLAB to read analog voltage signals from the polarimeter. The following methodology was used for each paddle:

1. move paddle with angle $a = 0° : 10° : 170°$
2. save S1, S2, S3 on a .txt file
3. plot the points on the Poincaré sphere

Based on the plots in Figure 3.14, the following observations can be made:

- The three paddles are not linked with the three main axis of the sphere.
- The points are not arranged following a structured pattern such as the meridians and parallels of a sphere.
- The points are not equi-spaced on the sphere despite that the step angle is constant.

Combining the three paddles does not result in a uniform coverage of the Poincaré sphere, as cleared shown in Figure 3.15. Achieving uniform coverage is crucial for two main reasons. First, it increases the diversity of the beam profiles, improving the chances of identifying the configuration that best matches the theoretical image. Second, it reduces the number of required measurements: the accuracy and the resulting profiles depend less on the number of sampled points and more on how they are distributed across the sphere. Therefore, it is necessary to develop an algorithm capable of uniformly covering the Poincaré sphere for a certain setup.

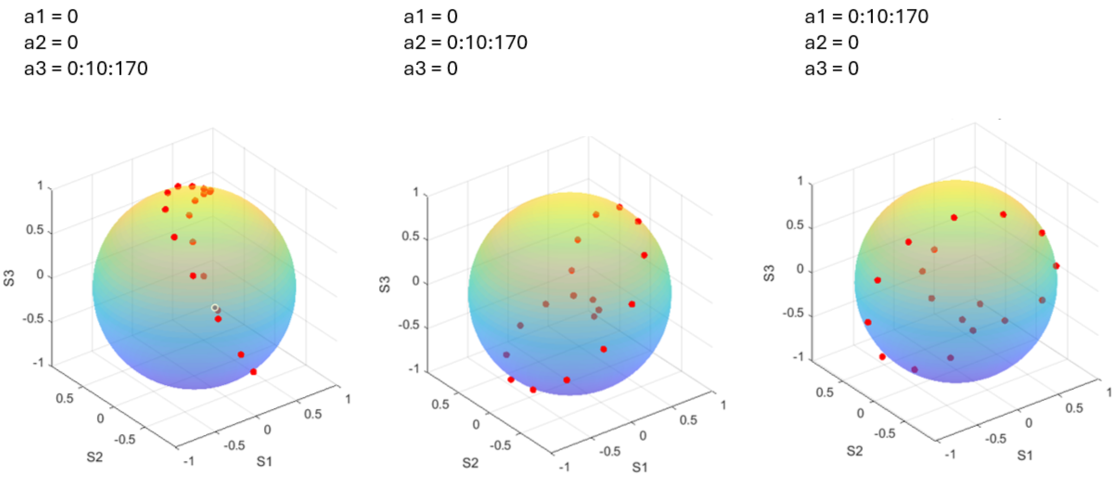

Figure 3.14: Polarimeter test. Sweeping one paddle at time.

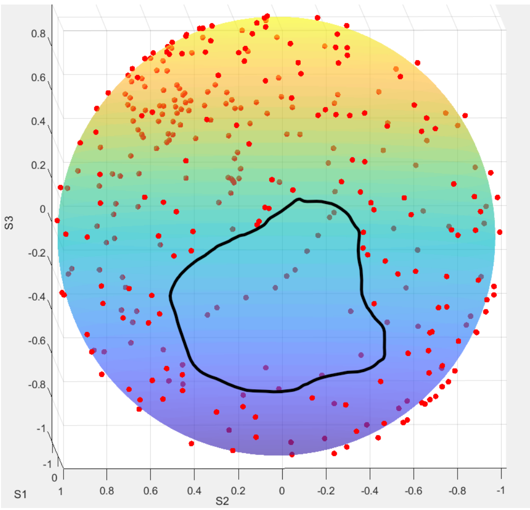

Figure 3.15: Sphere coverage map. The highlighted area clearly shows a lack of coverage.

Matching Algorithm

In light of the limitation highlighted, a custom algorithm was developed to enable a more uniform and efficient exploration of the Poincaré sphere. The algorithm generates a predefined set of uniformly distributed points over the sphere. These points are then used as target polarization states. The algorithm strongly relies on the repeatability of the measurements: it was, indeed, crucial to observe that to the same angle combination corresponds the same SOP. The repeatability allows to do just one massive data acquisition instead of repeating the matching algorithm for each point. The goal of the algorithm is to build a Look-Up Table to map a theoretical grid and has three steps:

1. **Generation of the theoretical grid**: this was achieved by implementing a golden

section spiral algorithm, a well-known method for evenly distributing points over the surface of a sphere. The algorithm computes a set of N points, where N is the parameter of the function `poincare_grid(N)` representing Stokes vectors, using the golden ratio. In addition to these points, six characteristic polarization states were added: Horizontal(H), Vertical (V), Diagonal (D), Anti-diagonal (A), Right-Handed Circular (RHC), and Left-Handed Circular (LHC).

2. **Points acquisition**: run the algorithm to sweep the MPC paddles in order to take an important number of points, map them ($a_1, a_2, a_3 \longleftrightarrow S_1, S_2, S_3$) and save them. The greater the number of measured points are taken, the more accurate the reconstruction of the experimental polarization grid.
3. **Minimum distance matching**: For each point in the theoretical grid, the corresponding experimental point is identified by searching for the one with the minimum Euclidean distance. This association is then stored in the Look-Up Table (LUT). Some lines of the final LUT are reported in table 3.1

a_1	a_2	a_3	S_1	S_2	S_3
160	60	140	0.011523	-0.065889	0.996589
140	0	120	-0.104363	0.107414	0.996632
100	160	140	0.141787	-0.131664	0.989343
0	0	120	-0.228910	0.010903	0.987119
140	100	160	0.210612	0.139741	0.972756
20	0	140	-0.194409	-0.263104	0.961312
60	140	160	-0.198564	0.281698	0.950916
20	140	0	0.349558	-0.159611	0.929687

Table 3.1: Some examples of the final LUT.

The algorithm is computationally efficient, as its three steps are straightforward to implement and do not involve significant processing overhead. Moreover, it can be easily adjusted to achieve higher accuracy, depending on the desired level of precision changing the number of points of the theoretical grid and the number of acquired points. As a final result, as shown in Figure 3.16, in order to validate the algorithm, the two plots were compared.

This algorithm concludes the analysis on polarization effects. Now that a uniform coverage of the Poincaré sphere has been achieved, it is possible to systematically search for the SOP that yields the best experimental beam profile. This optimal configuration can then be correlated with the corresponding theoretical mode and with other experimental modes, enabling a deeper investigation into mode discrimination and potential crosstalk levels.

3.4 Characterization of Modal Crosstalk

This section focuses on analyzing the correlation between the optimal SOP and the corresponding theoretical mode, as well as the correlation between the optimal SOP and other

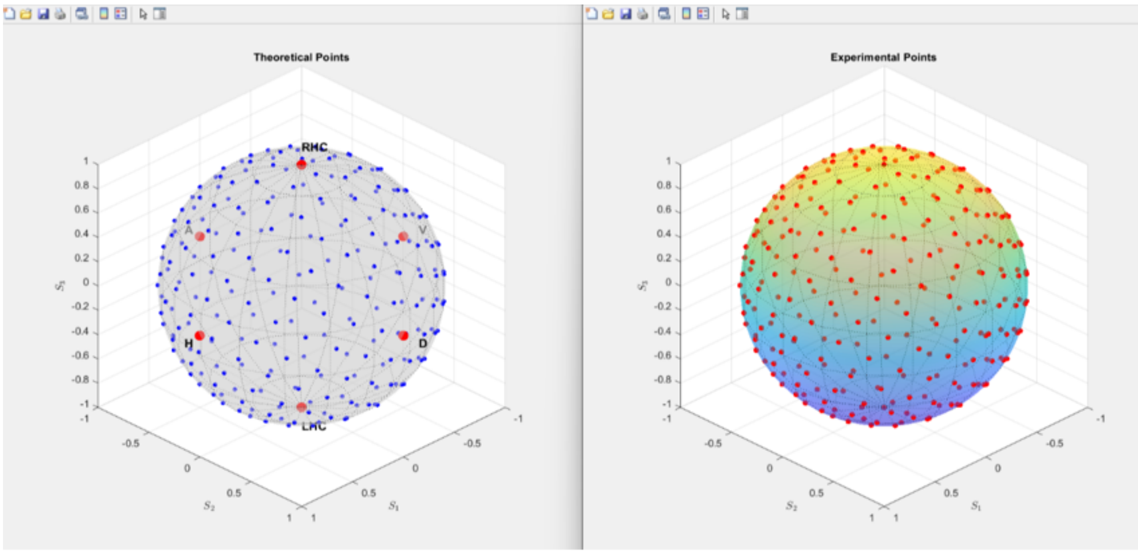

Figure 3.16: Coverage of states-of-polarization on the Poincarè sphere: theoretical grid on the left, plot of the minimum distance points on the right.

experimental modes. The aim is to investigate and draw insights about mode crosstalk, which plays a crucial role in the context of the subsequent communication part. The ultimate goal is to build a correlation matrix for entire mode set based on [25], where each element represents the correlation value between an input mode and all other modes. In the ideal case, where modes are perfectly orthogonal, this matrix would be diagonal. The analysis is based on the images collected, each image for each point on the uniformly covered Poincaré sphere.

3.4.1 Setup and parameters

As previously discussed, the following analysis is highly dependent on the specific experimental setup employed which is illustrated in Figure 3.17. The laser source used is DFB laser operating at a wavelength of 1554.130 nm (S/N: 5Y107464), with an input power of $P_{in} = 7$ dBm. This laser is connected to a Thorlabs MPC320 motorized polarization controller [21].

The optical signal is then fed into an asymmetric 1x2 optical power splitter 90/10 ratio, where 90% of the power is directed to the MPLC device configured as a mode multiplexer, while the remaining 10% is routed to the Thorlabs PAX5720VIS-T polarimeter to monitor the state of polarization, both via the graphical user interface and through MATLAB using a National Instrument USB-6009 DAQ device.

The output of the MPLC is coupled into an FMF which is terminated by a Thorlabs F810APC-1550 collimator acting as the optical transmitter.

At the receiver side, the optical beam is collected using a Thorlabs LMR2/M lens and analyzed by a Duma Optronics BeamOn Complete system. This system includes a CCD camera head, a post, a built-in filter wheel with a set of 3xNG Schott colored filters (NG4, NG9, NG10) [22].

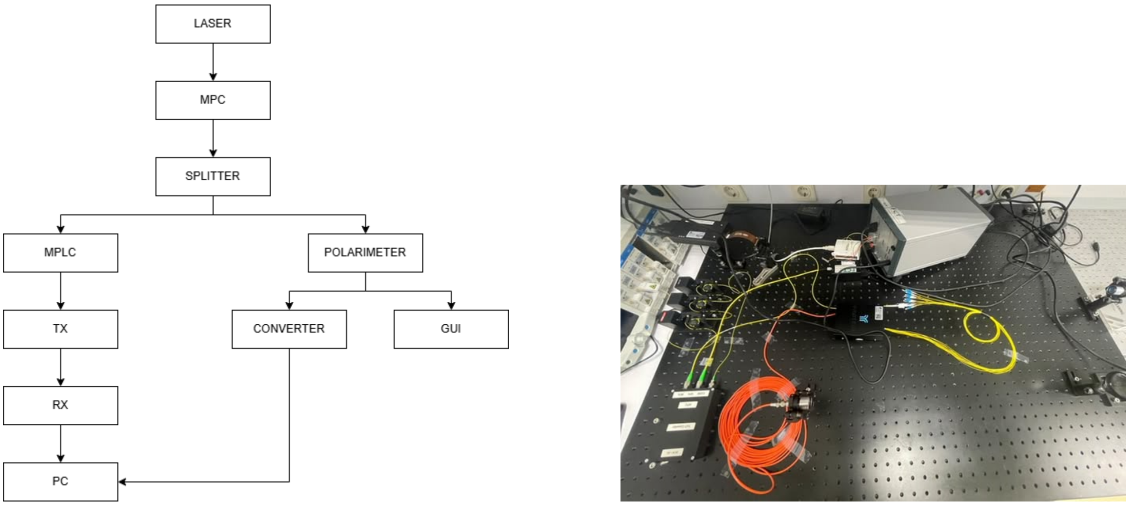

Figure 3.17: Experimental setup: source and MPC are on the left, while in the bottom left there is the splitter. The gray box is the polarimeter followed by the converter.

The BeamOn system, connected to MATLAB for image acquisition and storage, is designed for real-time measurement of continuous or pulsed laser beams. It measures laser beam parameters, such as: intensity profiles, beam width, shape, position and power [22]. The choice of image parameters—such as format, color, shape, and resolution—was the result of several trials aimed at optimizing the correlation between the input modes and their theoretical references. These parameters were selected to maximize the correlation score and ensure consistency during the characterization process. After extensive testing, the following configuration was adopted:

- **Format**: PNG
- **Color**: Black and white
- **Shape**: Square
- **Resolution**: 512 × 512 pixels
- **Points**: 250

3.4.2 Generation of Theoretical Hermite-Gaussian Modes

Before performing the experimental correlation analysis between the MPLC output and HG modes, it was necessary to generate accurate theoretical reference profiles for each target mode. These reference profile are essential for quantifying the degree of mode purity and for validating the correct operation of the MPLC. For this purpose, a numerical simulation was implemented to synthesize the transverse intensity distributions of HG modes.

To numerically generate the transverse modes of the HG family shown in Figure 3.18, a custom MATLAB simulation was implemented. These optical field distributions are solutions of the paraxial wave equation [15] in Cartesian coordinates and are widely used to model beam propagation in free-space optical communication systems involving mode division multiplexing.

The simulation is based on the physical definition of HG beams and includes the implementation of a custom function to compute Hermite polynomials of arbitrary order [26]. The visualization and spatial modeling were adapted from open-source scripts available on MATLAB Central File Exchange [27]. The beam parameters were initialized by setting the wavelength λ, the Rayleigh range z_0, and the beam waist W_0, derived from the relation $W_0 = \sqrt{\frac{\lambda z_0}{\pi}}$.

A two-dimensional spatial grid was created using `meshgrid` function, covering a square region in both x and y directions. The beam field $U(x, y)$ was computed by summing HG modes of order (l, m) according to a coefficient matrix A, which defined the amplitude weight for each mode. In this analysis, only one mode was considered at a time, meaning that there was no intentional overlap between modes in the generated field. This approach allowed for isolated evaluation of each mode's profile and facilitated mode-by-mode comparison with theoretical references.

After summing the contributions of the selected HG mode, the resulting complex field was reshaped and visualized using a grayscale intensity plot of $|U(x, y)|^2$. These images serve as theoretical reference modes for the correlation-based detection process: they are used both in same-mode correlation, to evaluate matching accuracy, and in cross-mode correlation.

To fully validate the orthogonality among the simulated Hermite-Gaussian modes, a complete matrix of Overlap Integral (OI)s was computed. Each mode, previously saved as a separate `.mat` file containing the complex field distribution $U(x, y)$, was loaded into MATLAB. The overlap between every pair of modes was then calculated using the normalized overlap integral formula:

$$\mathrm{OI} = \frac{\left| \int\int U_i(x,y) \cdot U_j^*(x,y)\, dx\, dy \right|^2}{\left(\int\int |U_i(x,y)|^2\, dx\, dy\right) \cdot \left(\int\int |U_(x,y)|^2\, dx\, dy\right)} \tag{3.2}$$

This quantity was computed for all combinations of the generated modes, resulting in a square matrix **OI**, where each entry (i, j) corresponds to the normalized overlap between the i-th and j-th mode.

3.4.3 Metric Selection Process

In order to accurately match experimental beam profiles to their theoretical Hermite-Gaussian counterparts, a reliable image similarity metric was essential. The selection of this metric was not immediate and required extensive testing and comparison. This subsection is structured as a step-by-step account of the process, highlighting both the strenghths and limitations of each tested method. The aim is to justify the final adoption of the Complex Wavelet Structural Similarity Index (CW-SSIM) as the most effective tool for this specific task.

Rather than directly presenting only the final result, it is important to show the rationale, the experimental attempts and the challenges encountered during this selection.

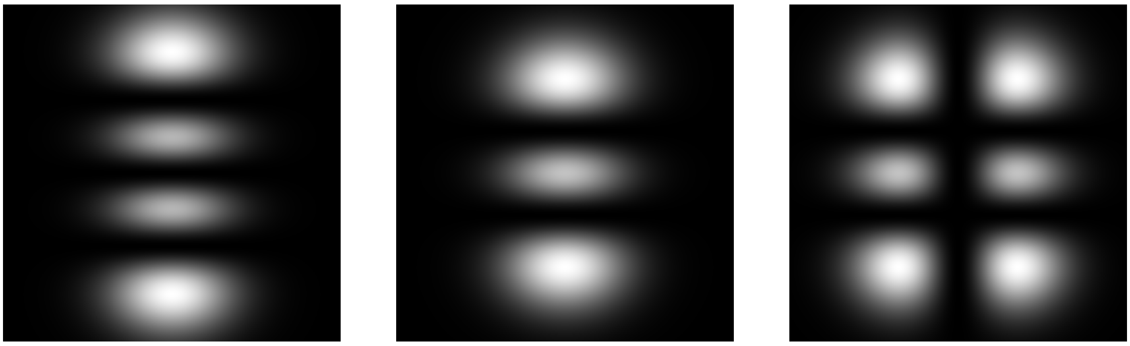

(a) HG$_{03}$ (b) HG$_{02}$ (c) HG$_{12}$

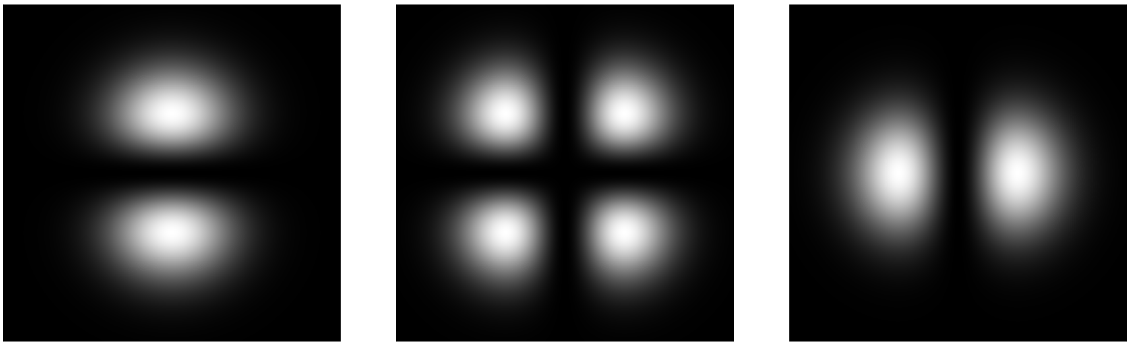

(d) HG$_{01}$ (e) HG$_{11}$ (f) HG$_{10}$

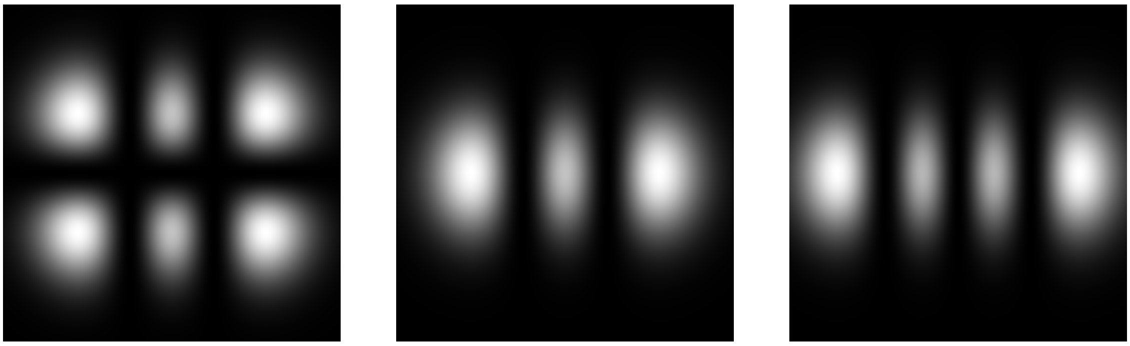

(g) HG$_{21}$ (h) HG$_{20}$ (i) HG$_{30}$

Figure 3.18: Simulated Hermite-Gaussian beam intensity profiles for different mode orders (l, m), generated via MATLAB.

Since the images were acquired experimentally, their intensity profiles were extracted as numerical matrices using MATLAB. All similarity metrics evaluated in this work operate on these matrices, comparing their spatial patterns and intensity distributions.

Correlation coefficient `corr2`

The first metric evaluated for matching the experimental intensity patterns to their theoretical HG modes was the normalized 2D cross-correlation, implemented via the MATLAB function `corr2` [28]. This method computes the linear coefficient between two matrices of the same size, returning a score in the range [−1,1] where 1 indicates perfect similarity.

From the mathematic point of view, the correlation coefficient r is defined as:

$$r = \frac{\sum_m \sum_n (A_{mn} - \bar{A})(B_{mn} - \bar{B})}{\sqrt{\sum_m \sum_n (A_{mn} - \bar{A})^2} \cdot \sqrt{\sum_m \sum_n (B_{mn} - \bar{B})^2}} \tag{3.3}$$

where A_{mn} and B_{mn} are the pixel intensities at position (m, n) in the experimental and theoretical images, respectively, and $\bar{A}$ and $\bar{B}$ are their mean intensities. This coefficient measures the linear relationship between the two intensity maps, essentially quantifying how much one image can be predicted from the other using a linear model.

Despite its simplicity and computational efficiency, the results obtained were not enough. In particular, even visually good matches often yielded low correlation scores; the highest one was on mode HG_{03} for which $r = 0.4235$. This poor performances is largely due to the high sensitivity of `corr2` to spatial shifts and angular misalignments: even a slight rotation or displacement of the experimental beam profile causes a significant drop in the computed scores, excessively penalizing the rotated image despite its overall similarity. As a result, the metric may favor a better-aligned rotation over an image that is visually more similar.

To mitigate this limitation, a second attempt was made by combining **corr2** with a brute-force rotation alignment procedure. The experimental image was rotated over a predefined range of angle predefined in discrete steps, and for each angle the correlation score was computed. The maximum score across all angles was then retained as a representative value for that mode.

Algorithm 2: Correlation with Rotation Alignment

```
Data: Theoretical image $I_{theory}$, experimental images set $\{I^k_{exp}\}$, rotation angles set $\Theta$
Result: Best matching image, best rotation angle, best correlation score
foreach $I^k_{exp}$ in experimental images do
    foreach $\theta \in \Theta$ do
        $I_{rot} \leftarrow$ rotate $I^k_{exp}$ by angle $\theta$;
        $score \leftarrow corr2(I_{theory}, I_{rot})$;
        if $score > bestScore_k$ then
            $bestScore_k \leftarrow score$;
            $bestAngle_k \leftarrow \theta$;
        end
    end
    if $bestScore_k > bestScore$ then
        $bestScore \leftarrow bestScore_k$;
        $bestImage \leftarrow I^k_{exp}$;
        $bestAngle \leftarrow bestAngle_k$;
    end
end
return $bestImage, bestAngle, bestScore$
```

While this second approach yielded visually better results-especially in the "best-case" correlation, where the correct theoretical match was identified-it still suffered form low overall scores and instability in ranking, particularly for higher-order modes such as HG_{21} and HG_{12}. Moreover, the brute-force rotation search significantly increased the computation time, making this method inefficient for practical use in case of a huge number of images.

For these reasons, `corr2`, with or without rotation, was ultimately discarded as the primary metric.

Overlap Integral

While the Overlap Integral, introduced in Eq.3.2, is physically motivated and theoretically robust when the complete field information is available since it accurately reflects mode orthogonality and energy overlap, making it particularly suitable for validating the quality and independence of numerically generated Hermite-Gaussian modes using the full complex field distributions $U(x, y)$, its application to experimental data is far less straightforward. The captured images in the experiment represent only the optical intensity $|U(x, y)^2|$, lacking the phase information necessary for a true overlap computation.

As a result, when applied to intensity-only data, the Overlap Integral loses much of its discriminative power. Without access to the complex field, the computed score becomes an approximation, and its ability to detect subtle differences between beam shapes is significantly reduced. Moreover, this metric is inherently sensitive to spatial misalignments, such as translations and rotations, which further deteriorates its effectiveness when comparing imperfect experimental profiles to ideal references.

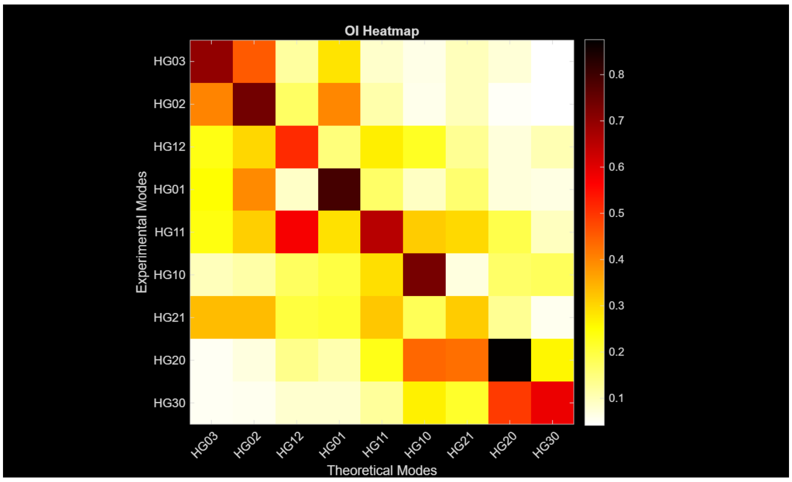

Figure 3.19: Heatmap of the OI matrix. Each row and each column correspond to a specific mode; their intersection represents the crosstalk value, which is here visualized using a color code.

Interestingly, in contrast to `corr2`, the Overlap Integral tends to penalize dissimilar modes more strongly. This is especially evident when comparing modes, such as HG_{10} and HG_{01}, where the score drops significantly, reflecting their theoretical orthogonality more faithfully than simpler correlation metric.

To further illustrate the behaviour of the OI in distinguishing different Hermite-Gaussian modes, Figure 3.19 visually summarizes the numerical values reported in Table 3.2, which contains a sample matrix of OI values computed between pairs of modes. The experimental modes on the columns were selected by computing the OI between the different experimental image and its corresponding theoretical mode. The diagonal values are not sufficiently high; moreover for mode HG_{21} the diagonal element is not the highest, indicating that this metric is not reliable for quantifying image similarity. On the other hand, the off-diagonal elements—representing the overlap between distinct modes—are significantly lower, often well below 0.5. This highlights how the OI metric strongly penalizes modes that differ substantially, such as orthogonal or higher-order modes.

In conclusion, the Overlap Integral is excellent for simulating and quantifying the theoretical differences between modes, as it provides a physically meaningful measure of similarity and penalizes strongly modes that are significantly different, such as orthogonal Hermite-Gaussian modes. However, it is not well suited for identifying the closest experimental image to a theoretical mode, since experimental images represent intensity patterns without phase information and can be affected by noise, misalignment, and other distortions, which limit the effectiveness of the OI metric in practical image comparison tasks.

Structural Similarity Index (SSIM)

The Structural Similarity Index (SSIM) is a perceptual image quality metric developed to evaluate the similarity between two images by modeling the degradation of structural

Table 3.2: Overlap Integral matrix between Hermite-Gaussian modes

Rows: Theoretical Modes **Columns: Experimental Modes**

	HG03	HG02	HG12	HG01	HG11	HG10	HG21	HG20	HG30
HG03	0.697	0.454	0.123	0.284	0.085	0.063	0.098	0.074	0.044
HG02	0.403	0.739	0.171	0.397	0.112	0.061	0.098	0.050	0.041
HG12	0.236	0.301	0.511	0.150	0.270	0.221	0.131	0.073	0.104
HG01	0.253	0.396	0.089	0.792	0.166	0.092	0.161	0.071	0.067
HG11	0.240	0.312	0.575	0.289	0.653	0.312	0.299	0.189	0.096
HG10	0.100	0.114	0.174	0.196	0.289	0.731	0.069	0.169	0.178
HG21	0.334	0.333	0.200	0.211	0.320	0.179	0.315	0.131	0.056
HG20	0.052	0.068	0.137	0.109	0.234	0.436	0.426	0.876	0.261
HG30	0.052	0.056	0.083	0.082	0.123	0.269	0.217	0.494	0.587

information, which is critical to human visual perception [29]. Unlike simpler metrics such as correlation coefficient or overlap integrals, SSIM quality assessment index is based on the computation of three terms, namely the luminance term, the contrast term and the structural term. The overall index is a multiplicative combination of the three terms [30] in order to model human visual perception.

Formally, given two image patches x and y, the SSIM index is computed as:

$$\text{SSIM}(x,y) = [l(x,y)]^{\alpha} \cdot [c(x,y)]^{\beta} \cdot [s(x,y)]^{\gamma} \tag{3.4}$$

where the three components are defined as follows:

1. The **luminance** comparison function evaluates the similarity of mean intensities:

$$l(x,y) = \frac{2\mu_x\mu_y + C_1}{\mu_x^2 + \mu_y^2 + C_1} \tag{3.5}$$

   where μ_x, μ_y are the average intensities of patches x and y, respectively and $C_1 = (K_1L)^2$ is a small constant to stabilize the division with typical parameters $K_1 = 0.01$ and L being the dynamic range of pixel values.

2. The **contrast** comparison function measures similarity of local contrast using standard deviations:

$$c(x,y) = \frac{2\sigma_x\sigma_y + C_2}{\sigma_x^2 + \sigma_y^2 + C_2} \tag{3.6}$$

   where σ_x^2, σ_y^2 are the variances of x and y, and $C_2 = (K_2L)^2$ with default $K_2 = 0.03$

3. the **structural** comparision function assesses the normalized correlation (covariance) of zero-mean patches:

$$s(x,y) = \frac{\sigma_{xy} + C_3}{\sigma_x\sigma_y + C_3} \tag{3.7}$$

   where σ_{xy} is the covariance between x and y, and $C_3 = \frac{C_2}{2}$

In the MATLAB implementation [30], the exponents α, β, γ are set to 1 by default, resulting in a simplified multiplicative form:

$$\mathrm{SSIM}(x,y) = \frac{(2\mu_x\mu_y + C_1)(2\sigma_{xy} + C_2)}{(\mu_x^2 + \mu_y^2 + C_1)(\sigma_x^2 + \sigma_y^2 + C_2)} \tag{3.8}$$

The key insight behind SSIM is that the human visual system is highly sensitive to structural information, i.e., how pixel intensities are organized and related spatially, rather than absolute intensity differences alone. The structural component $s(x,y)$ captures this by comparing the correlation of the local patterns between two patches after normalizing luminance and contrast, thereby providing a more perceptually relevant similarity measure. Compared to the correlation coefficient **corr2** and OI metrics, SSIM has several advantages in the context of comparing experimental beam profiles with theoretical models. It accounts for local luminance and contrast variations, is more robust to uniform intensity shifts, and provides a better correlation with human perceptual judgement of similatrity. This makes SSIM particularly useful when dealing with intensity images from experiments, where phase information is absent. However, SSIM is still sensitive to geometric distortions such as translation and rotations, which can degrade the similarity score even when the underlying mode structure is preserved.

Given the limitations related to image misalignment and rotation sensitivity, during the selection of the best matching image, the same rotational correction applied in the `corr2` method was also employed here, after carefully centering the images. While this approach improved the matching accuracy, it came at the cost of a significantly increased computational time-approximately 35 to 40 minutes were needed to select the best image from a dataset of 250 candidates. Considering the need for intra-mode comparisons and more efficient processing, a faster solution was subsequently sought to optimize the comparison procedure.

Complex Wavelet SSIM (CW-SSIM)

To overcome the sensitivity of SSIM to geometric distortions as small translations and small rotations-common issues in experimental image acquisition-an enhanced version called the CW-SSIM was developed [31] [32]. CW-SSIM operates in the complex wavelet domain, where it exploits the stability of local phase patterns under mild geometric deformations. Instead of comparing pixel intensities directly, it measures similarity between the complex wavelet coefficients of the two images, which encode both magnitude and phase information at multiple scales and orientations.

The key idea is that phase structures of natural images are often more stable than intensities, and carry significant perceptual importance. In this context, phase structure refers to the relative alignment of complex wavelet responses across multiple scales and orientations. When an image is decomposed using complex wavelets (as in CW-SSIM), each local region yields coefficients that encode both amplitude and phase information.

Even under changes in lighting or contrast, the relative phase—which determines the positioning of edges, textures, and structural details—tends to remain consistent, whereas global intensities can vary significantly. Therefore, CW-SSIM measures structural similarity by evaluating the consistency of these local phase patterns, making it robust to

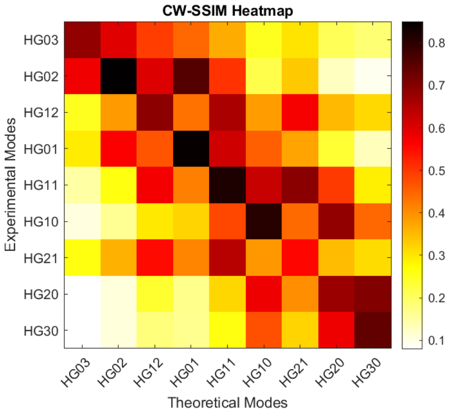

Figure 3.20: Heatmap of the CW-SSIM

small translations, scalings, and rotations that would otherwise degrade SSIM scores. Given two sets of complex wavelet coefficients $c_x = c_{x,i}$ and $c_y = c_{y,i}$ at the same spatial location and scale, the CW-SSIM index is defined as:

$$\text{CW-SSIM}(c_x, c_y) = \frac{2\left|\sum_i c_{x,i} c_{y,i}^*\right| + K}{\sum_i |c_{x,i}|^2 + \sum_i |c_{y,i}|^2 + K} \tag{3.9}$$

where $c_{y,i}^*$ denotes the complex conjugate of $c_{y,i}$, and K is a small constant used to avoid instability in low-energy regions.

Compared to SSIM, CW-SSIM is thus more robust to spatial misalignments, which significantly improves matching reliability in experimental contexts where image centering and orientation cannot be perfectly controlled.

In this work, CW-SSIM has been selected as the algorithm of choice for the intra-mode image comparison task, in order to reduce computational time and maximize similarity score. The index was computed using the publicly available MATLAB implementation provided by Mehul on the MathWorks File Exchange [33], which applies a steerable pyramid decomposition followed by CW-SSIM computation across subbands. This change allowed image comparisons to be performed without the need for manual centering or exhaustive rotation alignment, cutting processing time from over 35 minutes to under 2 minutes for the same dataset of 250 candidate images—an improvement that proved essential for scaling the mode classification pipeline. While the CW-SSIM index proves highly effective in selecting the best matching SOP from a set of acquired images, its robustness to small geometric distortions can become a limitation when the goal is to penalize dissimilarities between distinct HG modes. In this work CW-SSIM exhibited outstanding performance in identifying the best image corresponding to a given theoretical mode as shown in Figure 3.20 where the highest score are very close to 1, and, overall, has higher scores than the one showed in Figure 3.19.

However, the same geometric insensitivity also reduces CW-SSIM's discriminative power when comparing structurally distinct modes. Indeed, even comparisons between different HG modes can yield relatively high CW-SSIM scores, especially when intensity distributions share qualitative structural features or when the phase information is

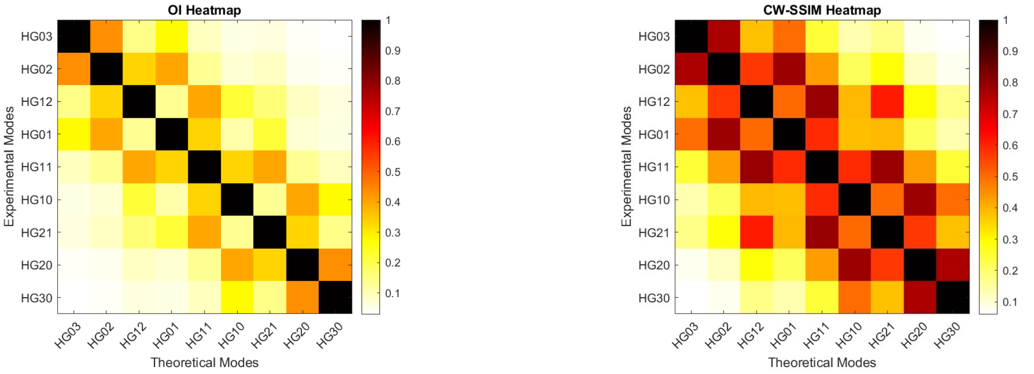

(a) Heatmap of the OI with theoretical modes compared with themselves

(b) Heatmap of the CW-SSIM with theoretical modes compared with themselves

Figure 3.21: Theoretical comparison

ambiguous due to the use of only intensity images. Unlike metrics such as the overlap integral, which rapidly decay as modal overlap diminishes, CW-SSIM may overestimate similarity between modes with similar energy distributions but distinct nodal structures. This behavior becomes even more evident in Figure 3.21, where a similarity matrix is computed among purely theoretical modes. It is apparent that off-diagonal values are significantly lower when using the OI, which highlights its ability to strongly penalize structural differences between distinct modes. This makes OI a more suitable figure of merit when quantifying modal crosstalk, as it provides a clearer separation between non-matching modes. In contrast, CW-SSIM exhibits relatively higher off-diagonal values due to its tolerance to small structural and phase variations, making it less effective for distinguishing between different mode patterns. However, this same robustness makes CW-SSIM particularly well-suited for identifying the best-matching SOP.

Hybrid Approach

The actual metric exploits the hybrid approach presented before:

1. CW-SSIM to pick the best SOP over the diagonal.

2. OI as figure of merit to build the correlation matrix

3. Finally, since the theoretical OI heatmap shown in Figure 3.19 is not ideal due to the absence of phase information,not all its off-diagonal elements are not exactly zero, as would be expected in a perfectly orthogonal modal basis. For this reason, the heatmap is used as a theoretical baseline and subtracted from the final results, excluding the diagonal elements, which are preserved. This correction helps to compensate for the residual overlaps between theoretical modes and ensures a more accurate evaluation of experimental crosstalk.

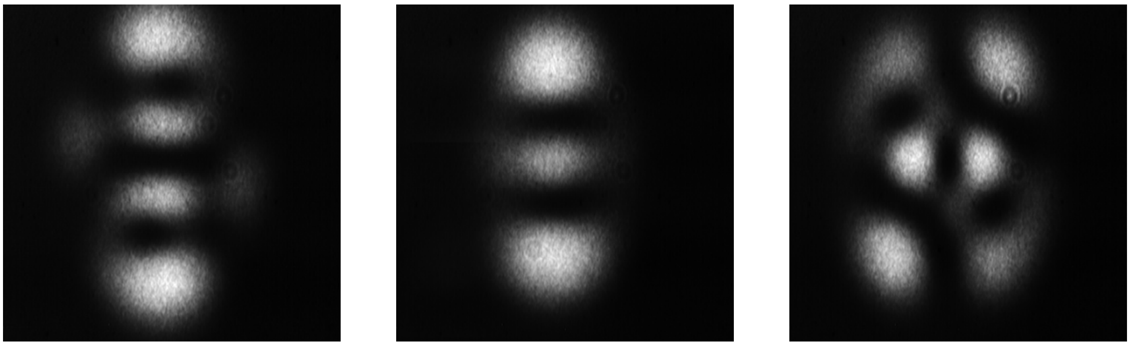

(a) HG_{03} (b) HG_{02} (c) HG_{12}

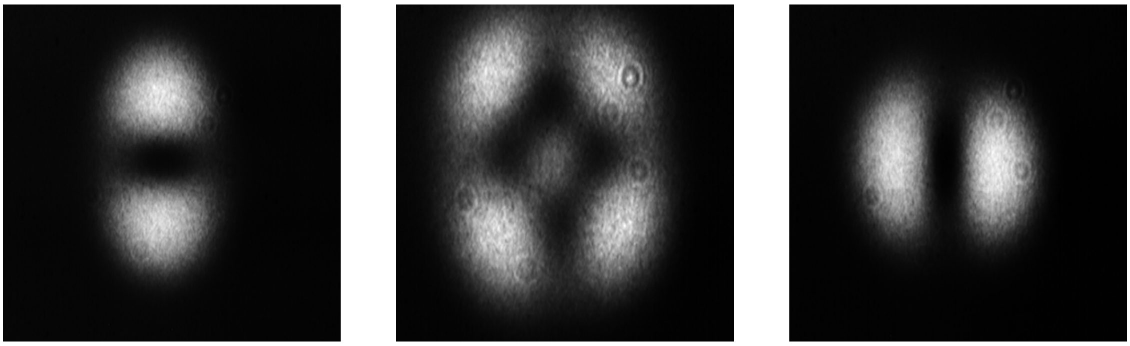

(d) HG_{01} (e) HG_{11} (f) HG_{10}

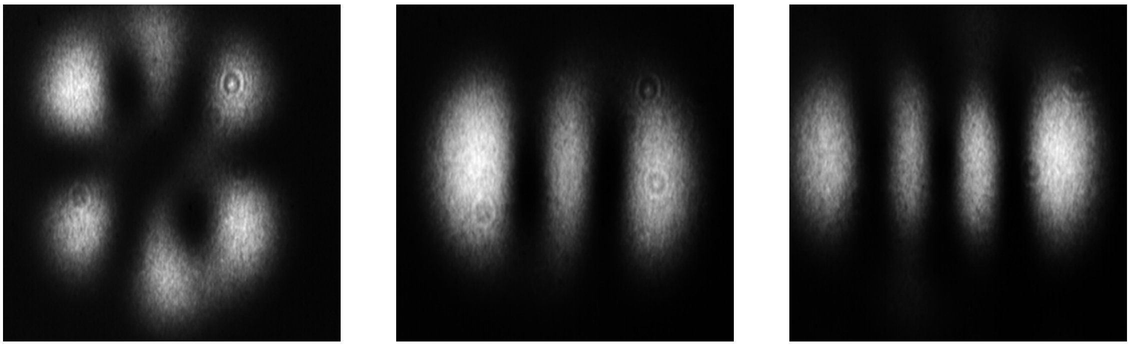

(g) HG_{21} (h) HG_{20} (i) HG_{30}

Figure 3.22: Best cases selected with CW-SSIM

3.5 Conclusion

Although the presented analysis does not account for phase information, thus providing only a partial picture of the full mode orthogonality, the results obtained are already sufficient to draw meaningful conclusions regarding the crosstalk performance of the MPLC. Overlap integrals computed on intensity-only data reveal that off-diagonal terms in mode comparison matrices remain consistently low. This indicates that the generated modes

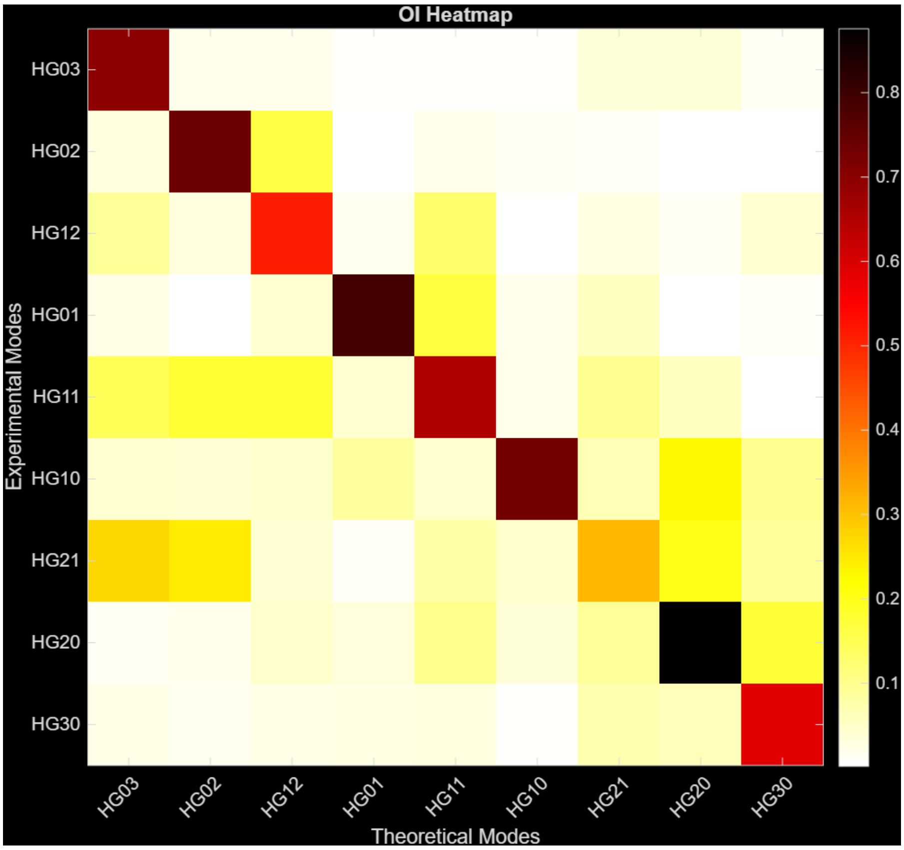

Figure 3.23: Correlation matrix obtained with the hybrid approach: CW-SSIM was used to select the best case and the overlap integral to compute the correlation. The measured matrix more closely approaches the ideal diagonal reference expected for a perfectly performing MPLC device, i.e., one without modal distortion or crosstalk.

are well-separated in the spatial domain and mantain a high degree of orthogonality.

A a low intermodal crosstalk is essential for applications such as mode-division multiplexing. While a full-field characterization would be required to capture residual phase-induced coupling, the current results already validate the effectiveness of the MPLC design in maintaining modal purity.

These findings support the conclusion that the MPLC offers sufficient isolation between modes and is thus a suitable platform for high-dimensional optical systems, where minimizing crosstalk is a critical requirement.

Chapter 4

Impact of Atmospheric Turbulence on Fiber Coupling Efficiency

This chapter focuses on the analysis of the optical power fluctuations and their impact on the received optical beam under conditions of atmospheric turbulence. Furthermore, three coupling modalities will be presented: SMF, PL and MPLC. The primary objective of this chapter is to validate and demonstrate the advantages of employing the MPLC in terms of received power and Rytov variance which will be the two figures of merit.

4.1 Experimental Setup for Atmospheric Turbulence Emulation

The experimental setup, shown in Figure 4.1 and in the diagram of Figure 4.2 is identical for all the three tests up to the receiver collimator. On the transmitter side, a laser output power of 13 dBm at a wavelength of 1550 nm is used. The FSO link consists of a fiber collimator (Thorlabs F810FC-1550) which is separated from the receiver collimator-dependent on the specific Rx device-by two custom-made atmospheric chambers, each 1.2 meters in length. Each chamber is equipped with two heaters, two fans, and two humidity/temperature sensors. The two atmospheric chambers are separated by a 10 cm free-space gap. The insertion loss introduced by the two atmospheric chambers is approximately 5-6 dB. The received optical power was measured using fast optical power meters like the one in Figure 4.3 with a sampling frequency $F_s = 10000$ samples per second and, subsequently processed in MATLAB.

Manual alignment was carried out by adjusting the position of the collimator, as well as the screws controlling its height and tilt angle, in order to maximize the received power measured at the receiver. The alignment was considered optimal when the measured power was consistent with the expected insertion losses. The test conditions are:

- The time of the emulation is 25 minutes; the plots will show less than the 25 minutes on the x-axis since some seconds were used at the start and in the middle of the

Figure 4.1: In this experiment the FSO link is composed of two fiber collimators, separated by two atmospheric chambers.

Figure 4.2: Block diagram of the setup until the fiber after the receiver

emulation to syncronize the fast optical power meters.

- temperature: Figure 4.4 shows the average temperature measured from the four fans in the chambers, two per each.

4.2 Coupling Efficiency using a Standard Single-Mode Fiber

In this configuration, the receiver consists of a SMF preceded by a Thorlabs F810FC-1550 fiber collimator. Since only the fundamental spatial mode is supported, the system is particularly sensitive to wavefront distortions and beam misalignments caused by atmospheric turbulence.

4.2.1 Optical Power Analysis

Figure 4.5 shows the temporal evolution of the received optical power under turbulent conditions. The red trace represents the instantaneous power while the white curve corresponds to the moving average, highlighting the overall trend.

The moving average shows a noticeable drop withing the first minutes of measurement, with a big decrease of power. In the central part of the acquisition, between 10 and 15 minutes, the received power stabilizes around an intermediate level, before gradually decreasing again to about -10 dBm in the final minutes.

4.2.2 Rytov Variance

The Rytov variance trend follows the same temporal behaviour previously observed in the received power trace. As shown in Figure 4.6, the peak values of the Rytov variance are found during the initial and final minutes of the measurements, corresponding to the deeps in the power trace. The peaks of the Rytov variance, indeed, corresponds to periods of strong turbulence. In contrast, the minima indicate intervals of weaker turbulence

Figure 4.3: One of the fast optical power meters.

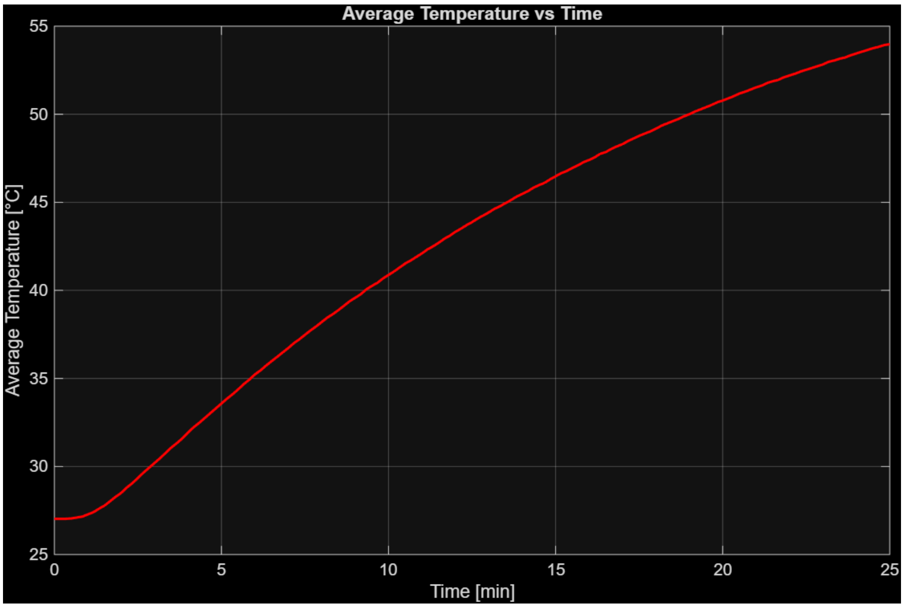

Figure 4.4: Temperature increase over time

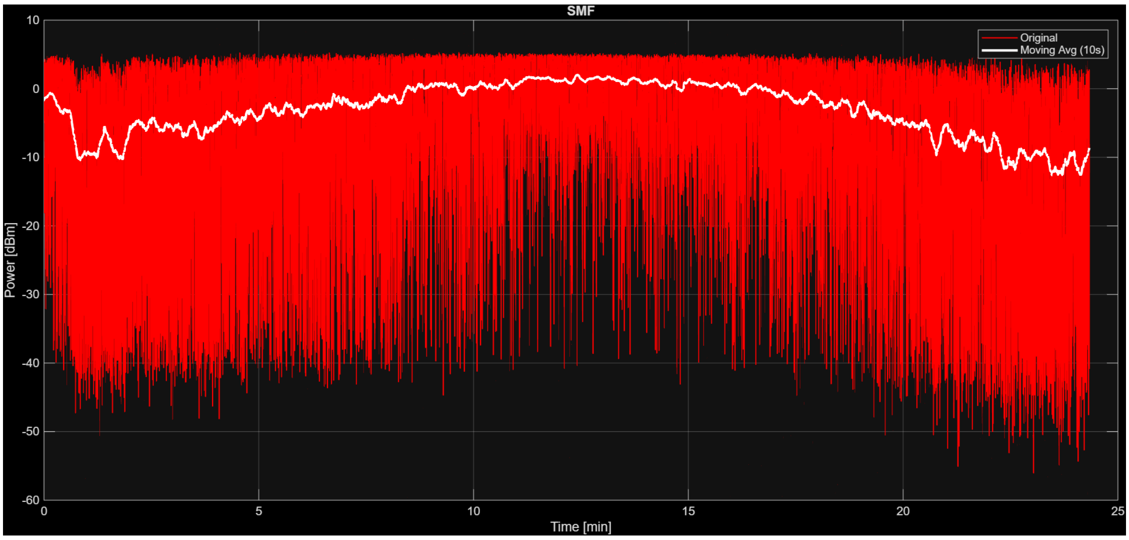

Figure 4.5: Power fluctuation for SMF at the receiver.

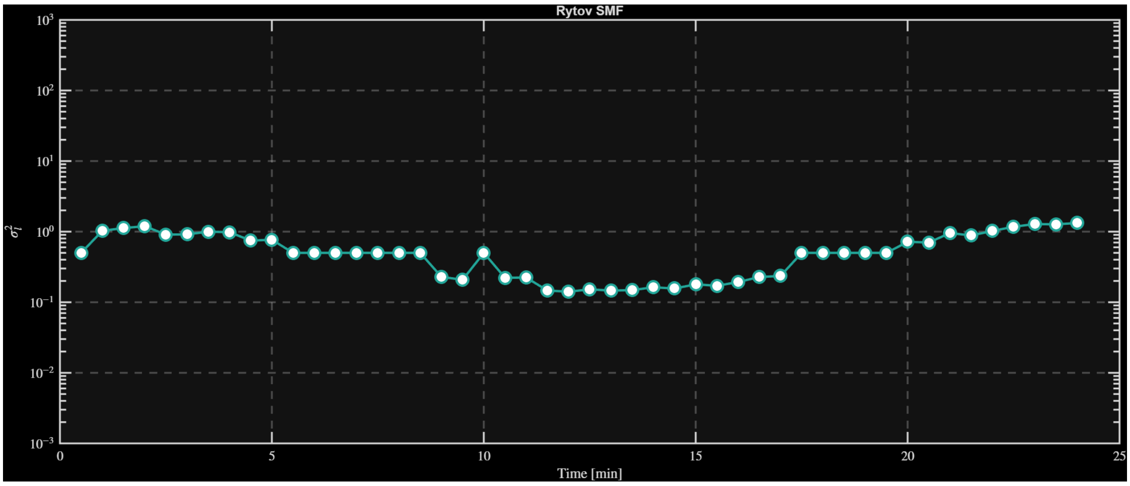

Figure 4.6: Rytov variance for SMF at the receiver

during which the coupling efficiency improves and the received power remains more stable. This correspondence between power fluctuations and Rytov variance validates the measurements and confirms that the temporal variations in received power are primarly driven by changes in the turbulence strenght within the atmospheric chambers.

To conclude, the SMF configuration represents the baseline for this study. This case serves as the common benchmark against which the PL and MPLC results will be compared, allowing a clear assessment of how mode diversity and spatial demultiplexing can mitigate turbulence-induced fading in free-space optical links.

4.3 Coupling Efficiency using a Few-Mode Fiber Followed by a Photonic Lantern

In this configuration, the receiver consists of a PL preceded by an FMF connected to the Thorlabs F810FC-1550 fiber collimator. The FMF supports three spatial modes, which are efficiently separated by the PL into distinct single-mode outputs. The three modes analyzed are:

- the fundamental mode LP_{01}
- LP_{11a}
- LP_{11b}

Each output of the PL is connected to an individual fast optical power meter interface with a computer for acquisition.

First, the temporal evolution of the received power is discussed for each mode individually. Then, the moving averages of the three modes are compared. Subsequently, the Rytov variance is anayzed for each mode to quantify the turbulence-induced fluctuations. Finally, a comparative discussion of the Rytov variance among the three modes is presented to evaluate differences in their response to atmospheric perturbations.

4.3.1 Optical Power Analysis

Figure 4.7 shows that the three channels exhibit correlated power fluctuations caused by the increase of the atmospheric turbulence. The modes are associated to the power meter used (pmX).

The LP_{01} mode, represented by the red trace, maintains the highest average power throughout the measurement, while the higher-order modes present lower mean levels. Overall, the three traces follow a similar pattern to that observed in Figure 4.5 also for what concerns the peaks and the minima. An interesting observation can be made at the end of the experiment: during the last three minutes, the LP_{11b} mode exhibits higher received power than the fundamental mode, indicating that a portion of the optical power has been coupled into higher-order modes due to increased turbulence.

Moving to the sum of the power traces shown in Figure 4.8 it is important to notice that the overall trend closely resembles the one presented in Figure 4.5. However, the average power level is higher, with minima around -5 dBm instead of -10 dBm. This behavior can be explained by the improved coupling efficiency provided by the photonic lantern: the optical power that would otherwise be lost at the receiver when using a SMF is now efficiently collected through the higher-order modes, resulting in a higher total received power.

4.3.2 Rytov Variance

In this section, the Rytov variance is analyzed to evaluate the impact of atmospheric turbulence on the different spatial modes at the receiver. The individual Rytov variances of the three modal channels are first compared to assess how turbulence affects each

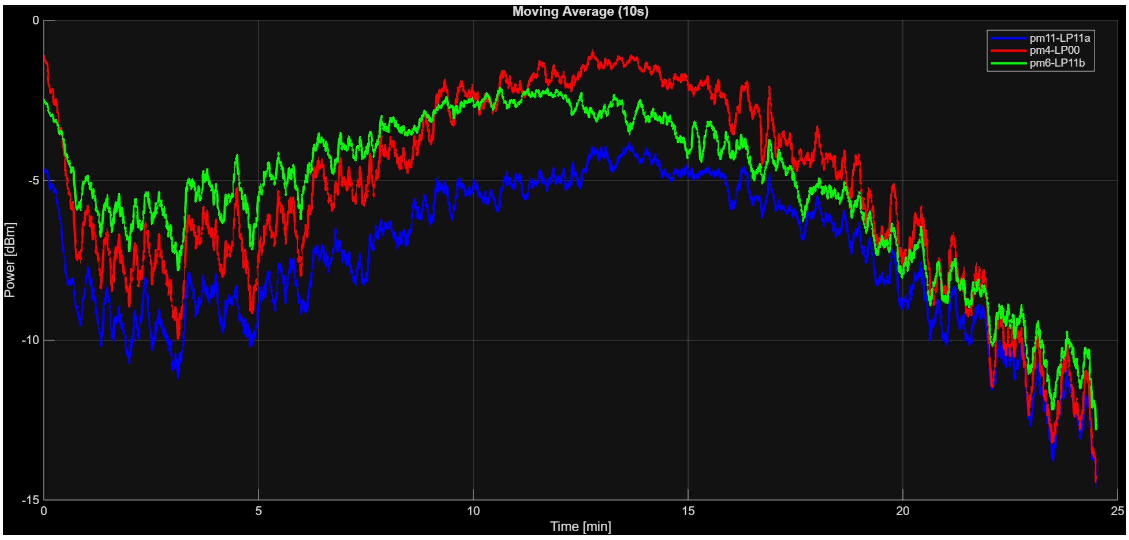

Figure 4.7: Moving average of power fluctuations for PL at the receiver

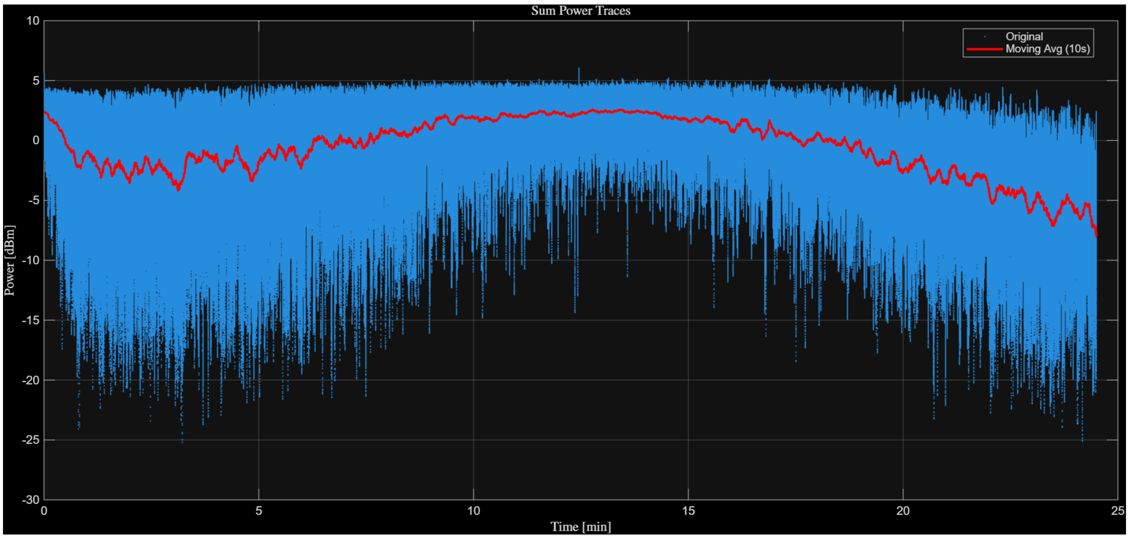

Figure 4.8: Sum of the optical power coupled into the photonic lantern outputs.

propagation mode differently. Subsequently, the Rytov variance computed from the sum of all received powers is presented, providing an overall estimation of the turbulence-induced intensity fluctuations on the total collected signal. Figure 4.9 compares the Rytov variance computed for the three spatial modes. As expected, the overall trend follows the behaviour of the received power traces, since stronger power fluctuations correspond to higher Rytov values. An interesting observation can be made in the last 5/6 minutes of the measurement: the Rytov variance of the fundamental mode (the red trace, pm4-LP_{00}) becomes the highest among the three. This validates what already discussed before: under stronger turbulence conditions, the fundamental mode is more affected by intensity

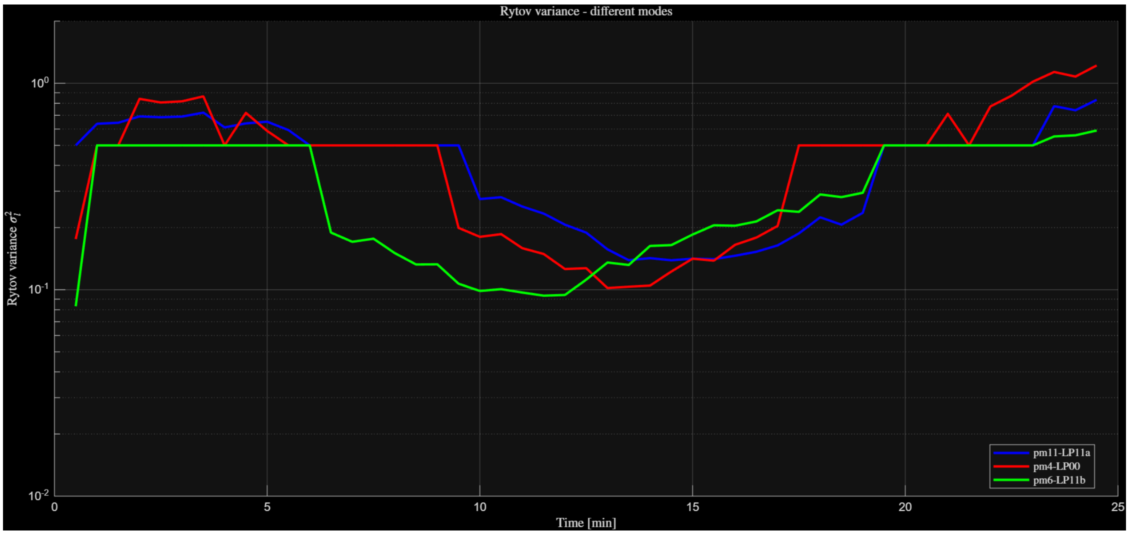

Figure 4.9: Rytov variance for PL at the receiver

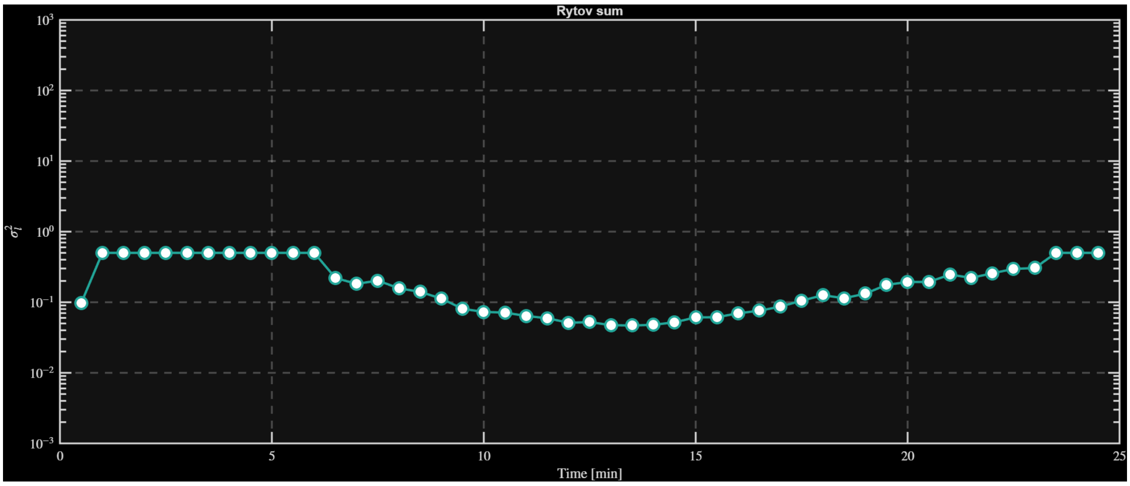

Figure 4.10: Rytov variance computed from the total received power coupled into the PL.

fluctuations, while the higher-order modes (pm11-LP_{11a} and pm6-LP_{11b}) appear slightly less sensitive. Figure 4.10 shows the Rytov variance computed from the total received power. The Rytov variance obtained with the PL remains consistently below 1, while in the SMF shown in Figure 4.6 it reaches values around 1. This indicates that the overall intensity fluctuations are lower when using the PL. This result is consistent with the behavior observed in the summed power traces in Figure 4.8 , where the total received power was higher and exhibited reduced fluctuations. It confirms again that the PL provides improved coupling stability under atmospheric turbulence, as part of the optical power that would otherwise be lost in the SMF is collected by the higher-order modes.

These results and findings suggest that increasing the number of supported modes,

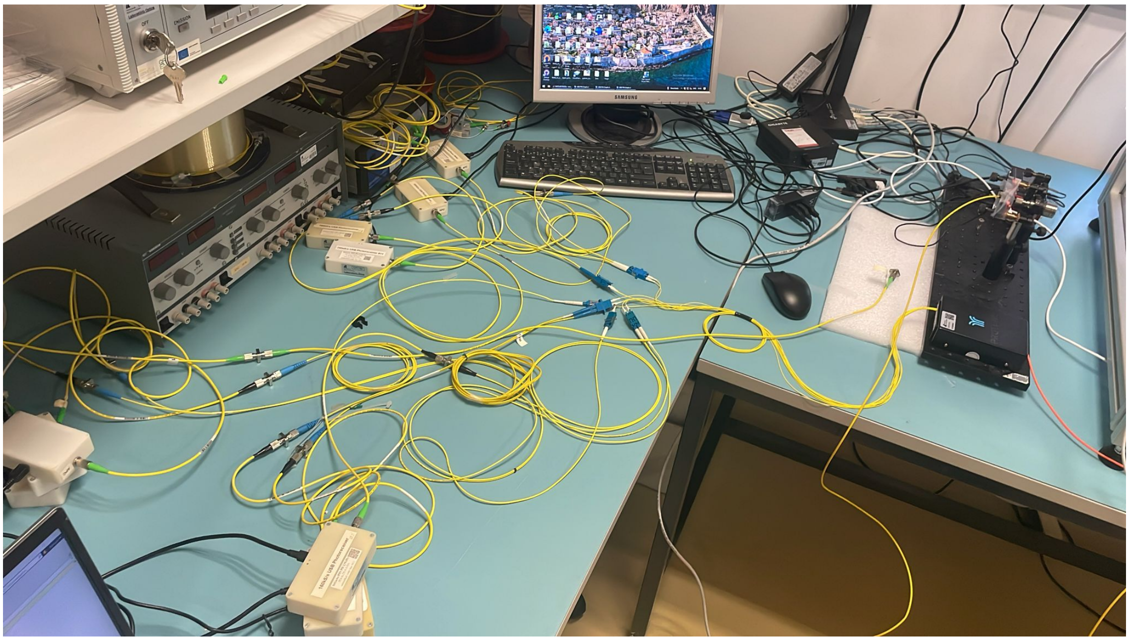

Figure 4.11: Fast optical power meters used for the different modes

such as with the MPLC device that supports up to ten modes, could further enhance system performance under turbulence, as will be discussed and analyzed in the following section.

4.4 Coupling Efficiency using a Few-Mode Fiber Followed by an MPLC

In this section, the performance of the receiver equipped with the MPLC is analyzed. In this configuration, the receiver consists of an MPLC preceded by an FMF connected to the Thorlabs F810FC-1550 fiber collimator. The MPLC device supports ten spatial modes, which are efficiently separated into dinstinct single-mode outputs. The ten modes are recalled here: [HG_{00}, HG_{10}, HG_{01}, HG_{11}, HG_{20}, HG_{02}, HG_{21}, HG_{12}, HG_{30}, HG_{03}].

Each of these outputs is connected to a different fast optical power meter to acquire the data as shown in Figure 4.11. The objective of this analysis is twofold. First, to demonstrate the improved robustness of the MPLC-based receiver under atmospheric turbulence, highlighting its ability to collect and separate multiple spatial modes with reduced power fluctuations. Second, to identify the four modes that exhibit the best performance in terms of stability and average received power, which will later be employed in the communication experiments, where the Waveshaper can process only four input modes.

The section is organized as follows. The first part presents the moving average of the received power for all ten modes, followed by the analysis of the total received power obtained by their sum. Subsequently, the Rytov variance is evaluated for each individual

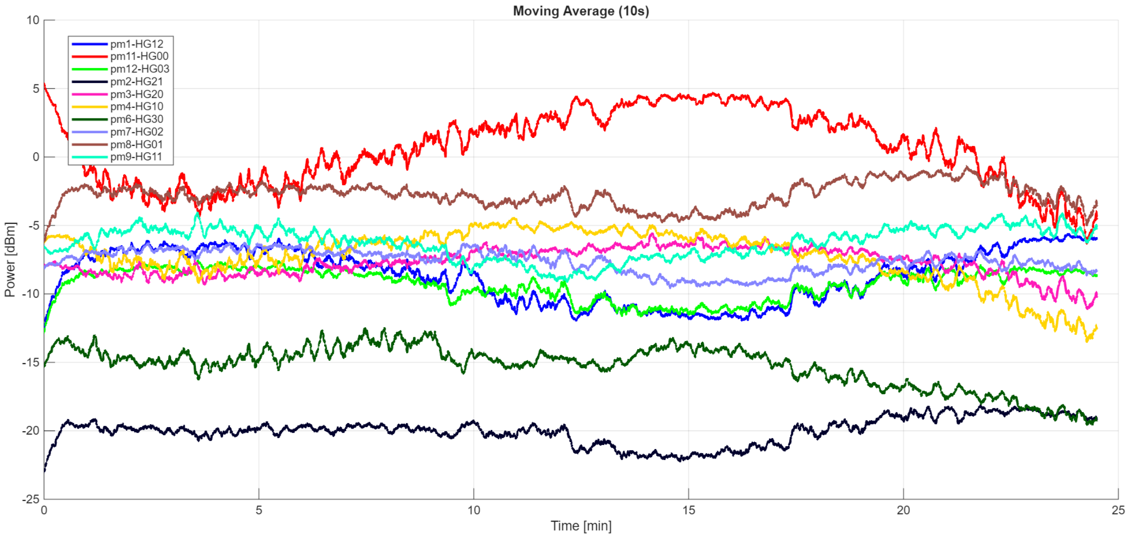

Figure 4.12: Moving average of the received power for the different modes

mode and for the total power, allowing a comprehensive comparison with the results obtained using the PL and SMF receivers.

4.4.1 Optical Power Analysis

Figure 4.12 shows the moving average of the received power for all ten modes associated to the corresponding power meters supported. In general, the highest average received power is associated with the fundamental mode HG_{00}, the red trace, which dominates the overall power distribution through the entire measurement.

The first-order modes, HG_{10} and HG_{01}, exhibit slightly different behaviors. The HG_{10} mode, represented by the brown trace, performs similarly to the fundamental mode and, together with it, represents the mode that collects the highest average power over the duration of the experiment. In contrast, HG_{10}, which is presented in yellow, shows a significant loss of received power starting from approximately the 15th minute, becoming one of the weakest modes by the end of the test. The HG_{11} mode, cyan trace, the HG_{02} mode, violet trace, and the HG_{20} mode display a rather stable trend, maintaining nearly constant power levels and showing limited sensitivity to turbulence-induced fluctuations as the emulation progresses. An interesting behavior can be observed for the HG_{12} and HG_{03} modes, in blue and in light green, which exhibit a pronounced drop in average received power during initial and central phases of the experiment, followed by a clear improvement from around the 17th minute onward. In the final part of the emulation, these modes perform remarkably well, with average power levels comparable to those of the more dominant modes. Finally, the modes HG_{30} and HG_{21}, in dark green and in black, show the lowest received power values during the experiment, confirming that they were not sufficiently excited under the analyzed experimental conditions. These modes are therefore the least representative in terms of collected energy and contribute minimally to the total received signal. To better understand the overall power collected

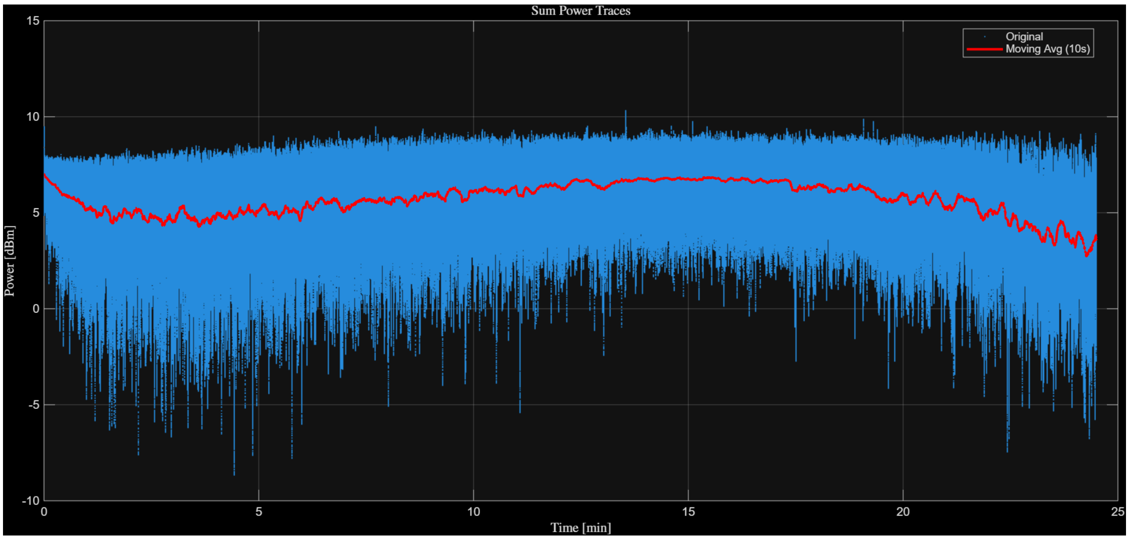

Figure 4.13: Sum of the received power across the modes

by the MPLC receiver, Figure 4.13 presents the sum of the received power across all ten modes. This combined trace provides a global view of the system's performance and allows a direct comparison with the results obtained using the photonic lantern and the single-mode fiber.

The plot shows the instantaneous power in blue and the moving average of the total power obtained by summing the ten modes in red. Two main observations can be made from this plot. First, the average received power is significantly higher compared to both configurations, either the SMF and the PL. This confirms the superior coupling efficiency provided by the MPLC receiver part, which is able to collect a larger fraction of the optical energy transmitted through the more and more turbulent channel by efficiently separating and collecting multiple spatial modes. Second, the overall behavior of the received signal appears much more stable. The trace does not exhibit abrupt power changes or deep fades, indicating reduced sensitivity to turbulence-induced fluctuations. These two characteristics - higher mean power and improved temporal stability - validate the optimal performance of the MPLC-based receiver under the same atmospheric conditions.

4.4.2 Rytov Variance

In the following analysis, the Rytov variance is evaluated both for the individual modes and for the total received power obtained by summing all ten MPLC outputs. The purpose of this study can be summed in three crucial points.

The first one is to validate the observations previously made on the received power traces by quantifying the turbulence-induced fluctuations in a statistical manner. Second point is to investigate how atmospheric turbulence affects each spatial mode differently, highlighting possible variations in sensitivity among the modal set supported by the MPLC and understand the possible gain while exploiting higher order modes. Finally,

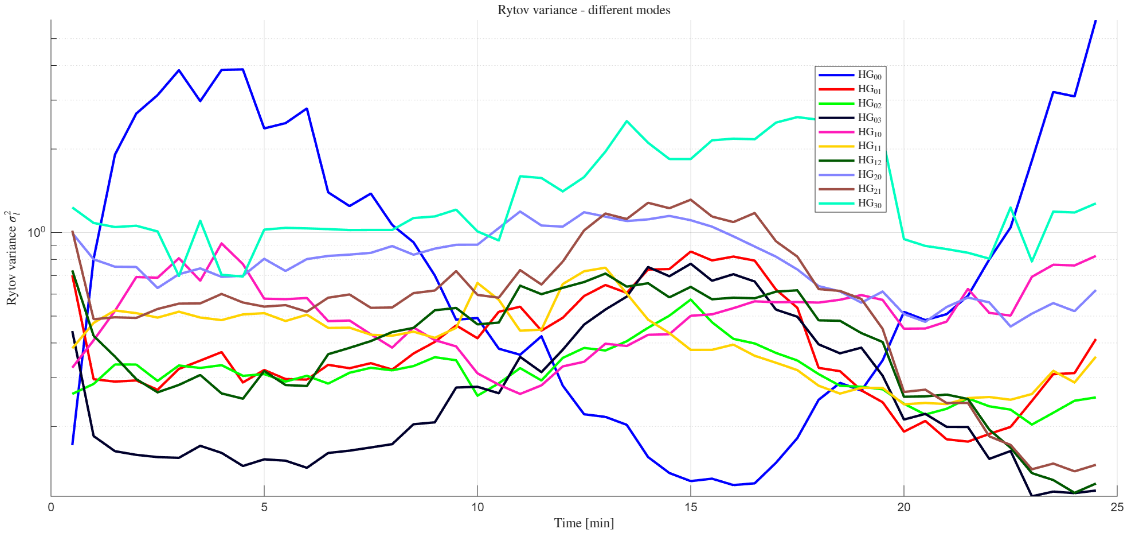

Figure 4.14: Comparison of Rytov variance of each mode of the MPLC

to assess the potential benefit of modal diversity by analyzing the Rytov variance of the summed signal, which provides an overall indication of the system's robustness under turbulent propagation conditions. Figure 4.14 shows the Rytov variance calculated for each of the ten spatial modes separately, with each curve corresponding to a specific mode. Starting with the fundamental mode HG_{00}, in blue, an interesting trend can be observed: during the first nine minutes approximately, this mode exhibits the highest Rytov variance, indicating strong intensity fluctuations. Between minutes 12 to 19, its variance decreases to become the lowest among all modes, before rising again towards the end of the test, where it once more becomes the most affected by turbulence. A similar behavior is observed for the HG_{10} mode, in pink, although its variance remains more stable in the final part of the experiment, without the sharp increase seen in the fundamental mode. The HG_{03} mode, in black, and the HG_{12} curve, in dark green, modes show an opposite trend: their variance peaks in the central part of the test, while in the last few minutes they display the lowest Rytov variance values, suggesting better stability under strong turbulence. A comparable pattern is found for the HG_{21} mode, in brown, which, even if it shows higher absolute variance level, becomes the third most stable mode at the end of the test. The HG_{11} mode, in yellow, gradually decreases in variance from minute 11 until the end. On the other hand, the HG_{01} mode, in red, exhibits low variance in the initial and final segments of the experiment, with a maximum in the central part. Finally, HG_{02}, in bright green, HG_{20}, in violet, and HG_{30}, in cyan, show relatively constant trends, with HG_{30} being consistently the worst-performing mode in terms of variance amplitude.

From this analysis, it can be observed that by the end of the emulation, the lower-order modes, such as the fundamental and HG_{10}, exhibit the highest Rytov variances, while some higher-order modes — in particular, HG_{03}, HG_{12} and HG_{21} — show the lowest values. This outcome indicates that the higher-order modes are less affected by

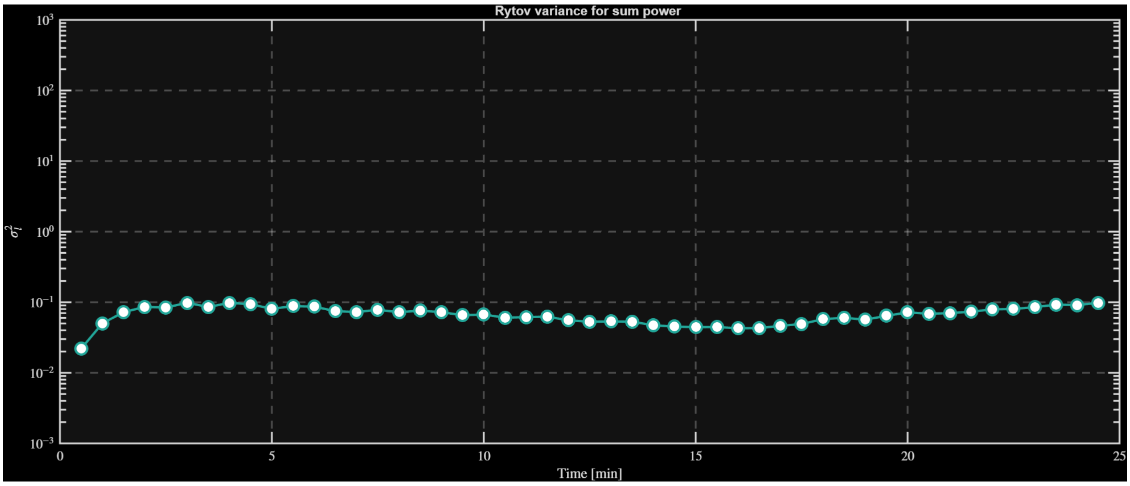

Figure 4.15: Rytov variance computed from the total received power coupled into the MPLC

turbulence-induced intensity fluctuations, meaning they are more resilient to the refractive index perturbations introduced by the heated chambers. Physically, this can be explained by the fact that higher-order modes have broader and more complex intensity distributions, which effectively average out local turbulence-induced distortions. In contrast, lower-order modes are more susceptible to phase and amplitude perturbations, leading to higher Rytov variance.

Overall, these results confirm that under the same turbulence conditions, higher-order modes demonstrate a greater robustness. Figure 4.15 reports the Rytov variance computed from the total received power, obtained by summing the contributions of all ten modes at the MPLC output. Two main considerations can be drawn from this result.

First, the overall behavior appears significantly more stable compared to the previous configurations based on SMF and PL receivers. In particular, no abrupt power drops or sudden fluctuations are visible, confirming that the intensity variations are well mitigated in this setup. Second, the Rytov variance values are notably lower, with a maximum around 10^{-1}, which represents a substantial improvement over the PL configuration, where the variance reached unity levels.

This outcome clearly demonstrates again that the use of multiple spatial modes through the MPLC leads to a more robust and turbulence-tolerant system. Each mode contributes to the total received power, compensating and balancing the fluctuations of those modes that are more affected by the atmospheric distortions. As a result, the combined signal benefits from a form of natural diversity gain.

In summary, employing the full set of ten modes not only increases the total received power but also ensures a lower and more stable Rytov variance, validating the superior performance of the MPLC receiver in this scenario. To provide a more detailed view of the incremental improvement introduced by each spatial mode, Figure 4.16 shows how the Rytov variance progressively decreases as additional modes are included in the summation. This representation allows to identify the most significant contributions

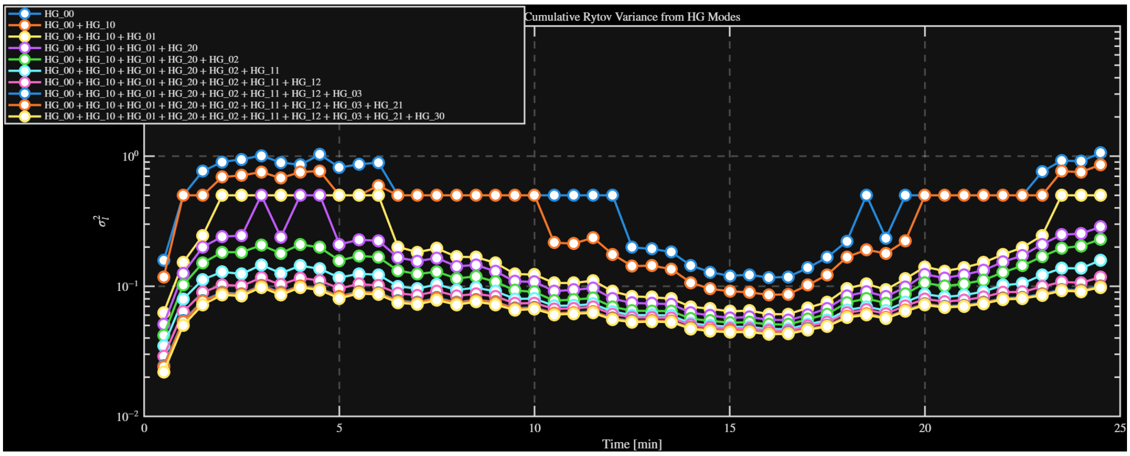

Figure 4.16: Progressive sum of the Rytov variance

and to better understand the trade-off between the number of modes employed and the effective turbulence mitigation achieved.

An initial improvement is clearly observed when adding the HG_{10} mode to the fundamental one, which already provides a noticeable reduction in the overall Rytov variance. The largest gain, however, is achieved when four modes are combined, namely the fundamental HG_{00}, the two first-order modes HG_{10} and HG_{01}, and the HG_{20} mode. A further significant reduction occurs when, to the bright green curve — corresponding to the combination of HG_{00}, HG_{10}, HG_{01}, HG_{20}, and HG_{02} — the HG_{11} mode is added. Finally, the inclusion of the third-order modes still provides a small yet measurable improvement, leading to the final curve reported in Figure 4.15, particularly noticeable during the last few minutes of the test. Nevertheless, even with the six modes mentioned above, a very stable behavior and low Rytov variance values can already be observed. This result is particularly important for two reasons. First, it validates the observations made in Figure 4.15, showing how the global curve is progressively reached as more modes are included. Second, it provides practical insights into the effective gain introduced by each additional mode, allowing one to identify the point beyond which the performance improvement becomes marginal, thus determining the optimal number of modes to be employed for a given turbulence condition.

4.5 Selection of Most Relevant Modes for Turbulence Mitigation

4.5.1 Optical Power Analysis

In the next chapter, the received signal will be processed using a Waveshaper device, which provides four input ports. For this reason, it is necessary to select a subset of four spatial modes among those supported by the MPLC. The selection must be based on the result presented in the previous analysis, taking into account both the average received power and the Rytov variance of each mode. In particular, the four modes that present

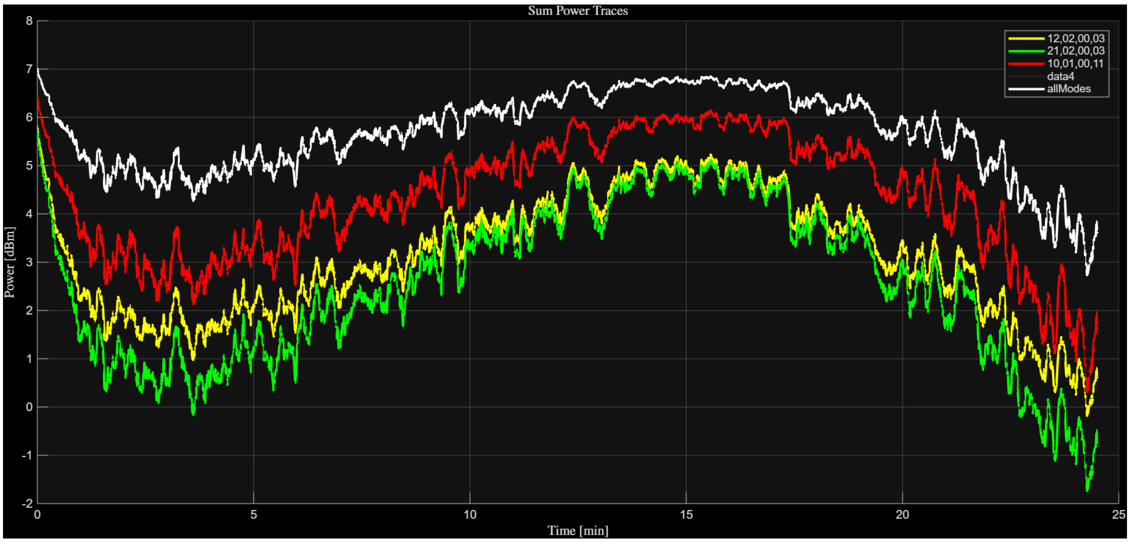

Figure 4.17: Comparison between the power of different combination of modes and the trace of the total sum

lower Rytov variance are preferable. At the same time, it is important to ensure that the selected modes contribute a non-negligible portion of the total received power, so that the resulting signal maintains a sufficiently high optical budget.

The aim of this section is to identify the four modes that provide the best performance. Once this subset has been determined, it will serve as the input configuration for the communication part. The first comparison focuses on the moving average of the received power for different mode combinations, benchmarked against the sum of all ten modes supported by the MPLC. In Figure 4.17, only the three best-performing combinations are shown for clarity, selected among the several possible configurations evaluated during the experiment. From this comparison, it is clear that the red curve, which is the combination composed of modes [HG_{00}, HG_{10}, HG_{01}, HG_{11}] achieves the highest average received power over the entire duration of the test. This four-mode combination represents a practical and well-balanced configuration and forms a strong candidate to be used in the communication experiments.

4.5.2 Rytov variance

The analysis of the Rytov variance is necessary to validate and confirm the observations previously made on the received power. Figure 4.18 presents a zoom on the final minutes of the experiment, which is the interval where the differences between the mode combinations become most evident. As a reference, the Rytov variance of the total sum of all modes, in green, is also reported, in order to assess which combination deviates least from the overall optimal stability. Here, the label Base refers to the set composed of the fundamental mode with HG_{10} and HG_{01} modes.

From the plot, it is clear that the four-mode combination identified earlier also provides the best performance in terms of turbulence resilience. The curve corresponding to

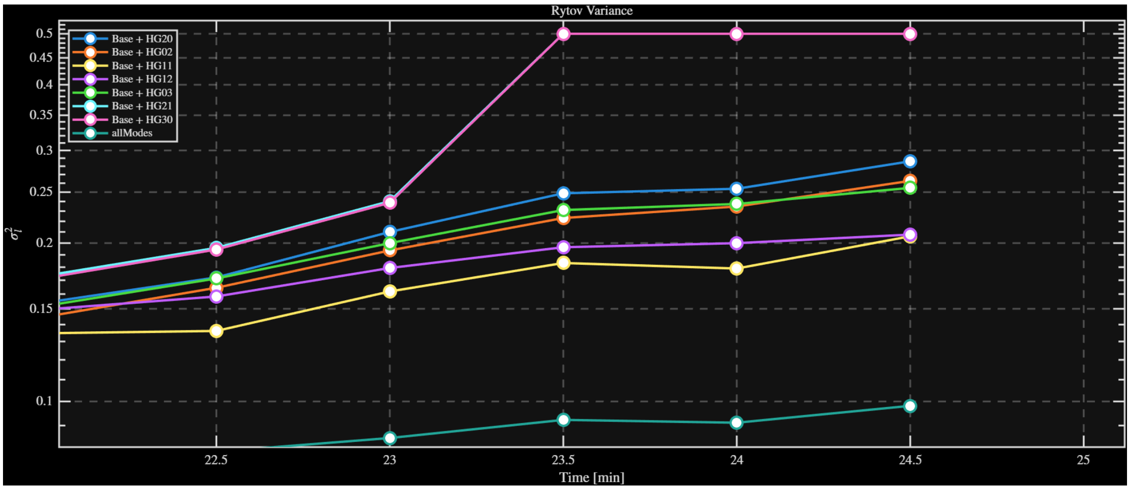

Figure 4.18: Rytov variace: zoom on the final minutes. 'Base' is the combination of the fundamental mode with HG_{10} and HG_{01}

this set, the yellow one, exhibits the lowest Rytov variance across the observed interval, confirming that this mode group experiences the least intensity fluctuations and therefore the weakest impact of atmospheric turbulence.

Based on both the received power analysis and the Rytov variance comparison, the set of modes:

- HG_{00}
- HG_{10}
- HG_{01}
- HG_{11}

is selected for the communication part.

4.6 Comparison

To conclude this chapter, a comparative analysis is presented between all receiver configurations examined throughout the experimental campaign. Specifically, the received power and the corresponding Rytov variance are reported for the following cases: the SMF baseline, the PL, the MPLC with all ten modes enabled, and the MPLC operating with the four selected modes identified in the previous section. For completeness, the behavior of the MPLC fundamental mode alone is also included as a reference.

The purpose of this comparison is to provide a clear and direct visualization of the performance improvements introduced by mode-division multiplexing techniques, highlighting the benefits in terms of both collected optical power and resilience to atmospheric turbulence. Starting from the power comparison shown in Figure 4.19, it is possible to observe that, in the most critical phases of the test—namely the initial interval (0–10

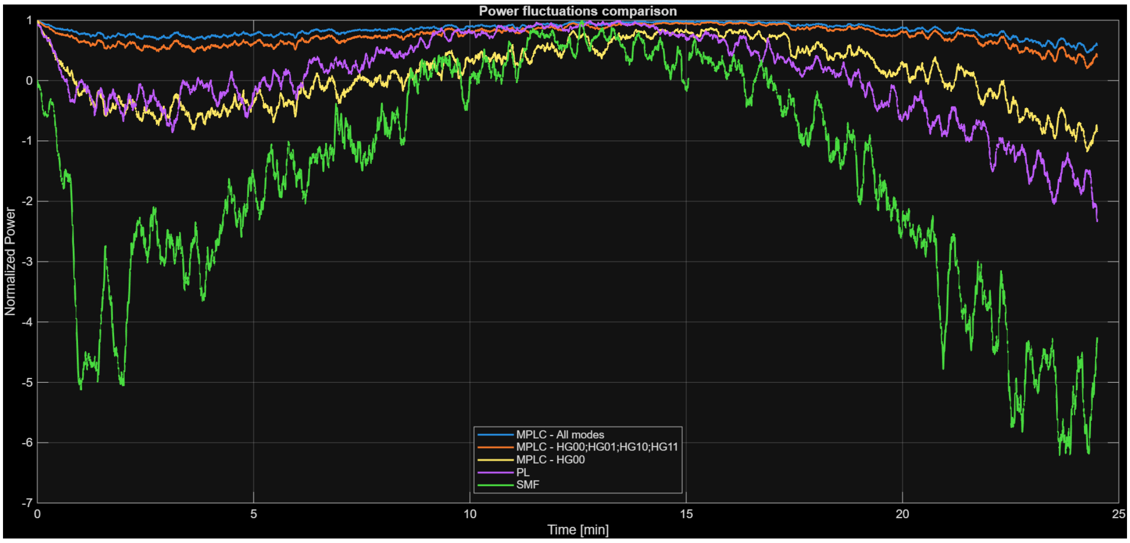

Figure 4.19: Power comparison

minutes) and the final interval (15–25 minutes)—the MPLC-based configurations clearly outperform the SMF and PL setups. In particular, it is noteworthy that the performance of the MPLC when all modes are enabled is very similar to the performance obtained when only the four selected modes are used. This confirms that the selected subset is capable of capturing most of the available power, while maintaining a more compact mode set.

A similar trend can be observed when comparing the PL configuration with the fundamental mode of the MPLC. The MPLC fundamental mode performs worse than the PL in the first part of the test, but provides better power levels in the final segment, where turbulence becomes more significant.

Finally, the SMF configuration consistently exhibits the poorest performance, with pronounced power drops that indicate limited robustness to turbulence and reduced coupling efficiency under misalignment and wavefront distortions. While the power comparison provides an initial indication of the performance differences between the tested configurations, a more complete evaluation requires examining the impact of turbulence on the received signal. By comparing the Rytov variance across the same configurations in Figure 4.20, it is possible to confirm whether the advantages observed in terms of received power also translate into improved robustness to turbulence.

Looking at the Rytov variance, the difference in performance between the MPLC using all modes and the MPLC operating with only the four selected modes becomes slightly more evident, with the full-mode configuration naturally achieving the lowest fluctuation levels. This result is consistent with the expectation that a larger number of spatial modes provides increased diversity and averaging against turbulence-induced distortions.

Regarding the PL configuration, its performance is noticeably better than that of the MPLC fundamental mode alone, in contrast to what was observed in the power

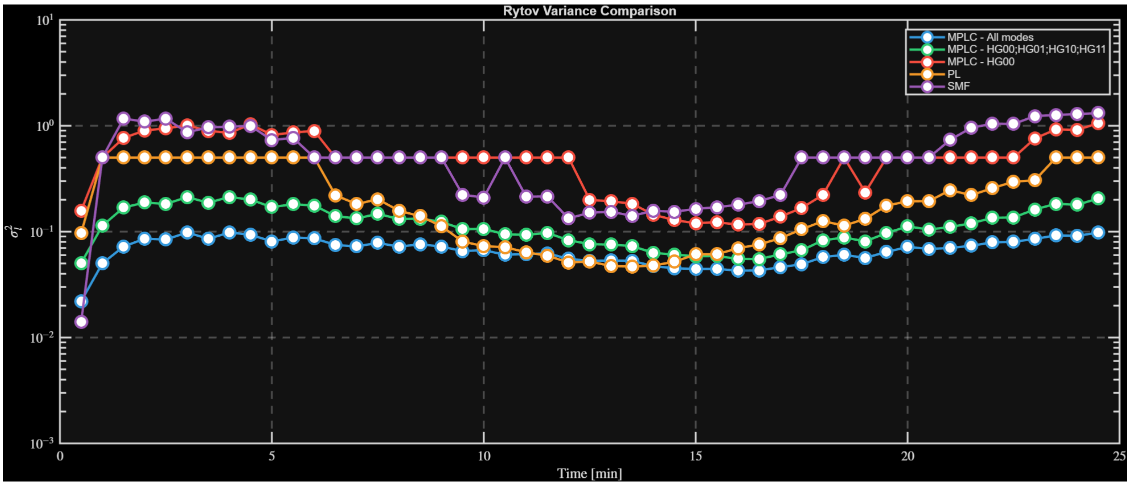

Figure 4.20: Comparison of the Rytov variance

comparison. This highlights once again that the use of multiple spatial modes plays a key role in mitigating the effects of atmospheric turbulence.

The worst performance in terms of Rytov variance is observed for the two configurations that do not exploit mode aggregation, namely the SMF and the MPLC fundamental mode. These cases experience stronger intensity fluctuations under turbulence, confirming the clear advantage of mode-division multiplexing in free-space optical links.

4.7 Conclusion

This chapter presented a comparative evaluation of different receiver configurations under controlled turbulence conditions, analyzing both the received optical power and the Rytov variance. The results clearly demonstrate the benefits of mode-division multiplexing in free-space optical links: the use of multiple spatial modes allows the system to recover power that would otherwise be lost and significantly reduces the impact of turbulence-induced intensity fluctuations.

Among all tested configurations, the MPLC operating with the four selected modes:

- HG_{00}
- HG_{10}
- HG_{01}
- HG_{11}

provided a favorable balance between performance and system dimensionality. These modes performed better primarily because they are efficiently excited at the transmitter and experience lower coupling losses at the receiver, while also benefiting from turbulence-driven power redistribution that transfers part of the energy from the fundamental mode to nearby low-order modes. As a result, this four-mode subset captures most of the useful received power while exhibiting reduced sensitivity to turbulence, achieving performance close to the full ten-mode configuration but with reduced system complexity.

It is important to note, however, that this optimal mode set is linked to the specific turbulence regime, launch conditions, and receiver alignment used in this experimental campaign. In different scenarios—such as stronger turbulence, misalignment, or longer propagation times—the distribution of modal power and the turbulence coupling dynamics may change, potentially shifting the set of modes that provides the best performance. Therefore, the selected four-mode configuration is optimal for the conditions tested, but the methodology established here can be directly applied to identify the optimal mode subset in different operating environments.

Based on this result this set of modes will be adopted in the communication experiments presented in the next chapter.

Chapter 5

Analysis of FSO communication systems

In this chapter, we present a structured experimental investigation aimed at evaluating the performance of a FSO communication link under increasingly realistic and turbulence-impacted propagation conditions. The ultimate objective is to assess how different receiving strategies ranging from the SMF to the multi-mode architecture based on a MPLC-affect the recovery of a high-order modulated optical signal after propagation through the two atmospheric chambers. All experiments with the Single-Carrier use a modulation at 64 Gbaud, while the experiment with the Multi-Carrier uses a modulation at 60 Gbaud. Both of them exploit 16-QAM constallation. Afterwards, the signal is pulse-shaped using a RRC filter with 0.1 roll-off. Each measurement campaign consists of a continuous 25-minutes acquisition, enabling statistically meaningful performance estimates.

The chapter is organized around five experimental stages, each introducing additional channel effects or enchanced modal-processing capabilities. This incremental approach allows for isolating the impact of individual system components while maintaining a consistent transmitter chain and digital signal processing framework.

Across all the scenarios, system performance is assessed through three complementary metrics:

- SNR;
- BER;
- NGMI.

These metrics provide a comprehensive understanding of the channel quality ranging from physical SNR impairments to FEC-relevant information-theoretic performance.

5.1 General Setup

All experiments are based on coherent transceiver. Only the propagation and receiving architectures differ between the various measurements campaings. These are the main components: first, a Keysight M8194A AWG is used to generate the electrical baseband waveforms driving the IQ modulator. It provides 45 GHz analog bandwidth and 120 GS/s sampling rate. The optical modulation stage employs a dual-polarization IQ modulator with 35 GHz bandwidth. Then, a narrow-linewidth nano-ITLA laser at 1550 nm serves as the optical source for all experiments. Before the atmospheric chambers, an Erbium-Doped Fiber Amplifier is used to compensate for modulator insertion losses and to adjust output power levels. All experiments employ a 40 GHz-bandwidth coherent receiver, with the optical power at its input carefully maintained between approximately −2 dBm and 0 dBm to avoid saturation or damage to the receiver front-end. Finally, 4 real-rime oscilloscopes (RTO, DPO77002SXR3) perform digitization/quantization with 70GHz bandwidth operating at 200 GS/s.

5.2 Digital Signal Processing Workflow

All acquired datasets are processed through the DSP pipeline, slightly different depending on the scenario, having the same main stages. The DSP chain compensates for linear and nonlinear receiver imperfections, residual frequency offsets, timing errors, polarization mixing and phase noise. The processing stages are applied in the following order:

1. signal Truncation if necessary to remove transients and non-stationary samples;
2. receiver deskew correction to compensate differetial delay between I and Q branches;
3. Gram-Schmidt orthonormalization;
4. DC offset removal;
5. data-aided carrier frequency recovery;
6. static equalization;
7. subcarrier demultiplexing and matched filtering when subcarrier multiplexing is present;
8. adaptive equalization;
9. transmitter/receiver clock synchronization;
10. two-stage adaptive equalization;
11. two-stage carrier-frequency recovery;
12. three-stage timing synchronization;
13. two-stage carrier-phase recovery.

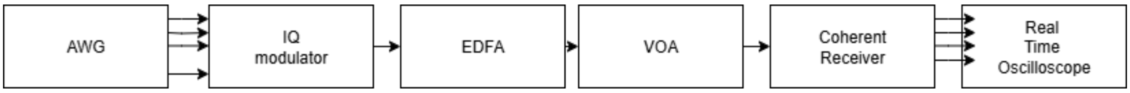

Figure 5.1: Back to back setup

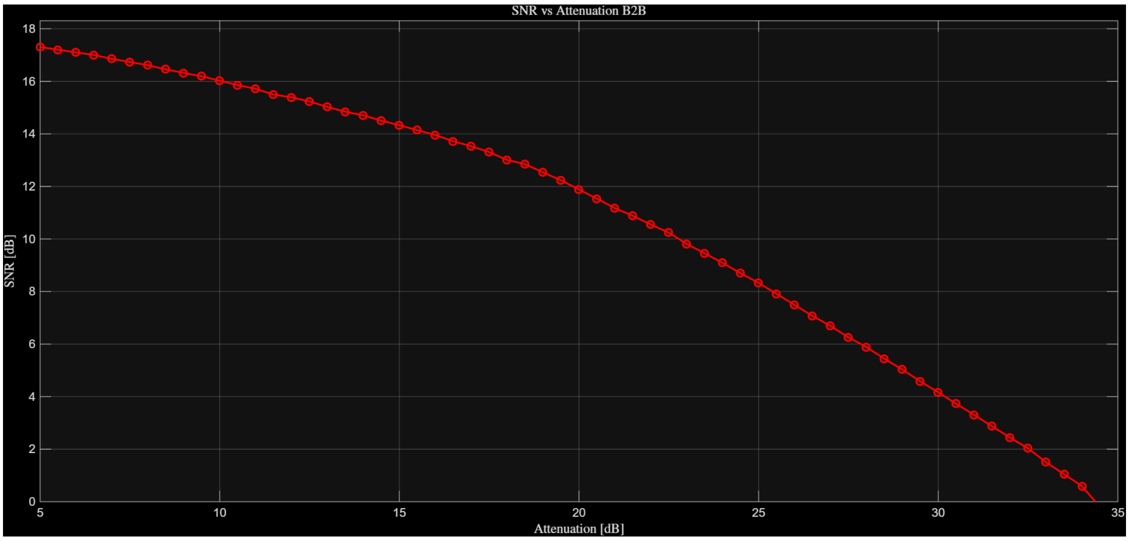

Figure 5.2: Plot of the SNR evolution against attenuation in B2B conditions.

5.3 Back to Back

The first experiment consists of a Back-to-Back (B2B) configuration, in which the transmitter output is directly connected to the coherent receiver through a Variable Optical Attenuator (VOA), as depicted in Figure 5.1. This scenario establishes the baseline performance of the system in the absence of any free-space propagation or turbulence effects. The VOA introduces a controlled optical attenuation ranging from 5 to 35 dB in 0.5 steps, effectively emulating the signal power losses that would be induced by atmospheric turbulence in subsequent experiments. This allows for a systematic characterization of the receiver's sensitivity and the determination of the maximum tolerable channel loss for reliable signal transmission. Figure 5.2 shows the SNR curve which exhibits a monotonic degradation as the attenuation introduced by the VOA increases. Starting from a maximum value of about 17 dB, the SNR progressively decreases as expected in a power-limited regime. For instance, at an attenuation of 23 dB, the SNR reduces to about 10 dB, and eventually approaches 2 dB at 32 dB of attenuation.

This behavior is consistent with the expected power-limited regime: in the absence of atmospheric distortion, the received signal quality is almost entirely dictated by the optical power at the receiver. The linear decay of the SNR confirms that the transmitter–receiver chain is operating properly and it is free from significant nonlinear or bandwidth-limitation penalties.

Most importantly, this B2B characterization is crucial for establishing the operational

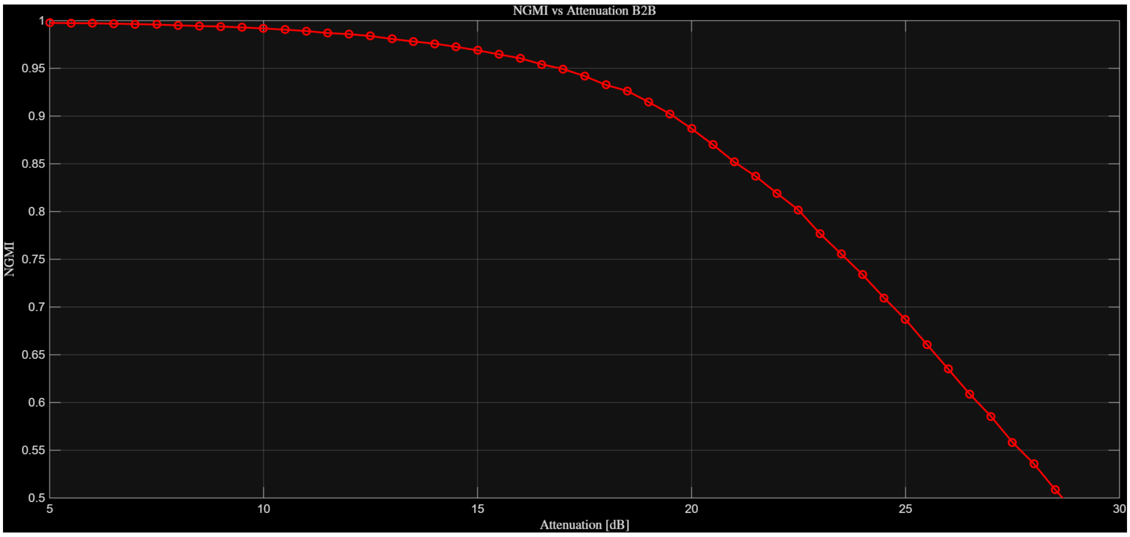

Figure 5.3: Plot of the NGMI evolution against attenuation in B2B condition.

power margin of the entire system. By observing the SNR values corresponding to different attenuation levels the attenuation levels where the link begins to operate near or below its required SNR threshold.

These baseline results serve as a reference for all subsequent experiments: any additional penalty observed under atmospheric propagation can be directly mapped to an equivalent "effective attenuation", enabling a clear quantification of turbulence-induced degradation. The NGMI showed in Figure 5.3 remains essentially flat and close to 1 up to about 10 dB attenuation, indicating that in this region the system operates with significant performance margin.

At approximately 19 dB attenuation , the NGMI crosses the 0.9 threshold, marking the transition to a regime where decoding is no longer guaranteed for typical FEC overhead (20–25%). Beyond this point, NGMI exhibits a rapid decline: it falls to 0.7 around 20 dB, and eventually reaches 0.5 near 27 dB attenuation.

This steep falloff illustrates the intrinsic sensitivity of high-order 16-QAM modulation to SNR reduction and reveals a sharp boundary between fully-correctable and non-correctable signal conditions.

From a system design perspective, this B2B NGMI trend is fundamental for identifying the critical attenuation levels beyond which the link becomes uncorrectable. It allows us to delineate the safe operating region of the system and provides a clear benchmark to assess the penalties introduced by atmospheric turbulence in the subsequent chapters. Any deviation from the B2B curve directly quantifies the turbulence-induced degradation and the improvement provided by modal diversity architectures.

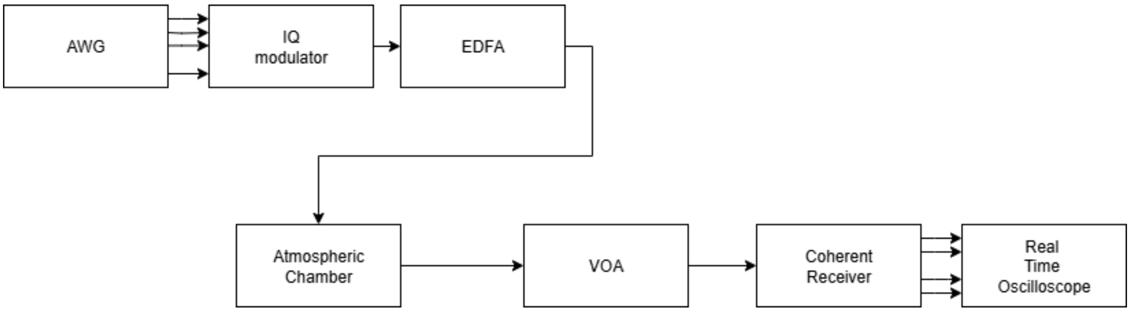

Figure 5.4: Setup of the free space propagation test without turbulence. The receiver is SMF-based.

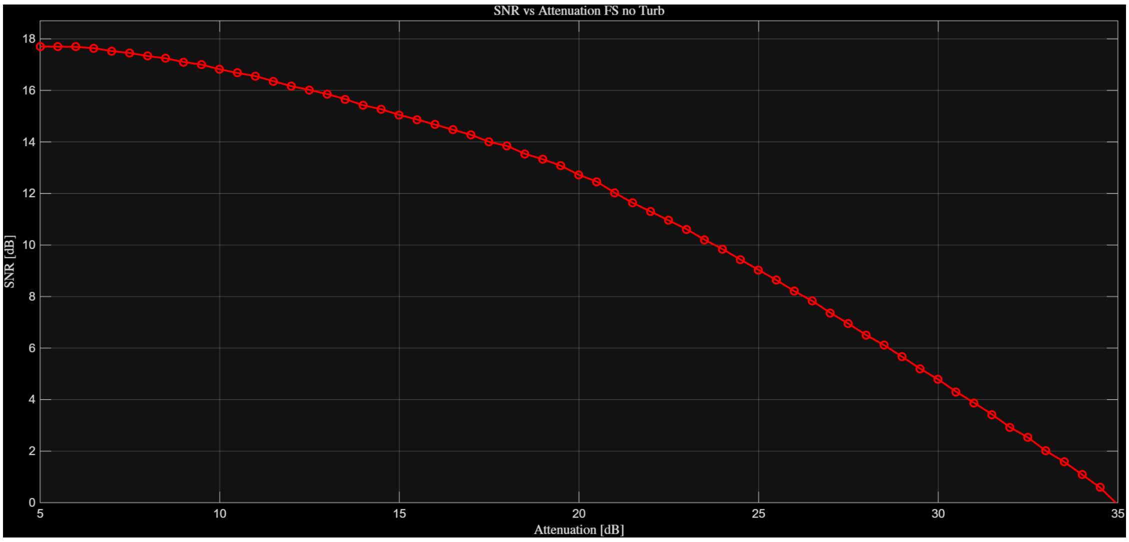

Figure 5.5: Plot of the SNR evolution against attenuation when propagating through the atmospheric chambers, without heating.

5.4 Experiment with Single-Carrier signal and without Turbulence

The second configuration, shown in Figure 5.4, introduces the atmospheric chambers in their non-heated state, allowing the optical beam to propagate through free space while avoiding any turbulence-induced fluctuations. This setup isolates deterministic effects—such as fixed insertion loss, residual misalignment, and coupling imperfections—while preserving an otherwise stable propagation path. The VOA is again employed to emulate controlled received power levels, enabling a direct comparison with the B2B results and verifying that the free-space section does not introduce additional impairments beyond its intrinsic insertion loss.

The SNR in Figure 5.5 profile closely matches the B2B baseline, confirming that the introduction of the two atmospheric chambers, when unheated, does not introduce

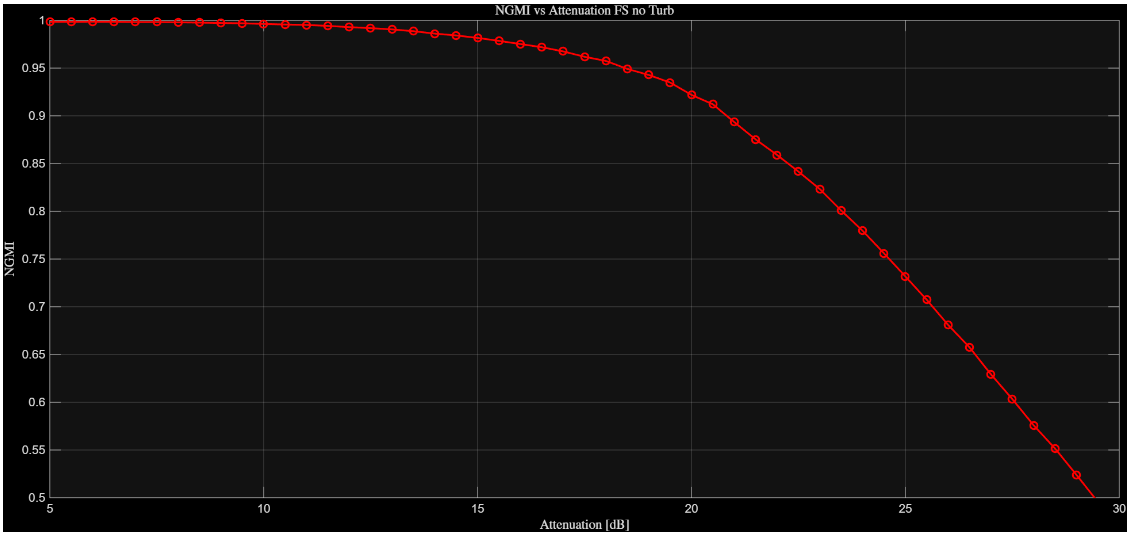

Figure 5.6: Plot of the NGMI evolution against attenuation when propagating through the atmospheric chambers, without heating

measurable distortion beyond their intrinsic insertion loss. The additional 5-6 dB loss is effectively compensated by the preceding EDFA, resulting in an SNR curve that overlaps almost perfectly with the direct-connection case.

This preliminary test is essential to validate the integrity of the free-space propagation stage: it ensures that all optical interfaces, alignments, and coupling stages are properly configured before introducing turbulence-induced fluctuations in the subsquent experiments.

Similarly, the NGMI in Figure 5.6 evolution remains substantially unchanged with respect to the B2B reference, maintaining degradation trends across the attenuation sweep. This confirms that, in the absence of heating, the chambers act as passive optical elements with no measurable impact on the signal quality after processing.

The consistency between the two NGMI curves validates the correct operation of the transmitter, receiver, DSP pipeline, and the free-space insertion path, providing a solid baseline for isolating the effects of atmospheric turbulence when the chambers are later activated.

5.5 Experiment with Single-Carrier signal and SMF at the receiver

The third experiment activates thermal turbulence inside the chamber, representing the first realistic turbulence-impaired FSO test. The receiver employs a SMF as shown in Figure 5.7, corresponding to the classical coherent communication architecture, which is directly connected to the receiving collimator as described in Chapter 4. This stage reveals the performance degradation caused by turbulence-induced scintillation, beam wander, and wavefront distortions when mode division demultiplexing is not exploited.

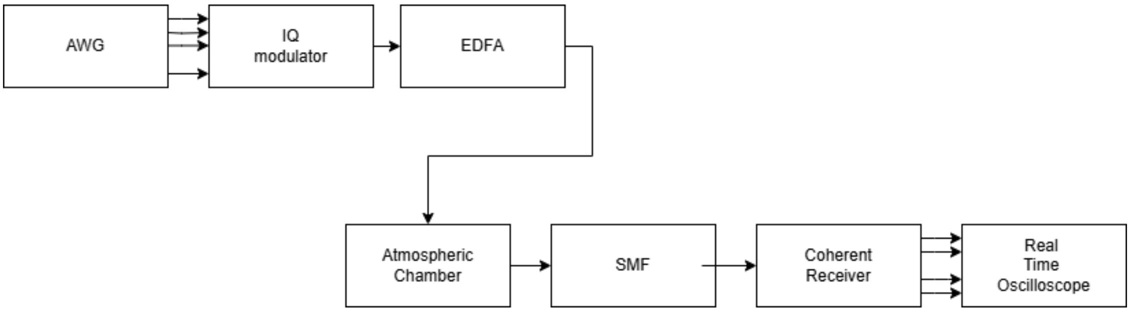

Figure 5.7: Setup with the SMF-based receiver. The setup is the same of the previous experiment, but with turbulence generated by the atmospheric chambers.

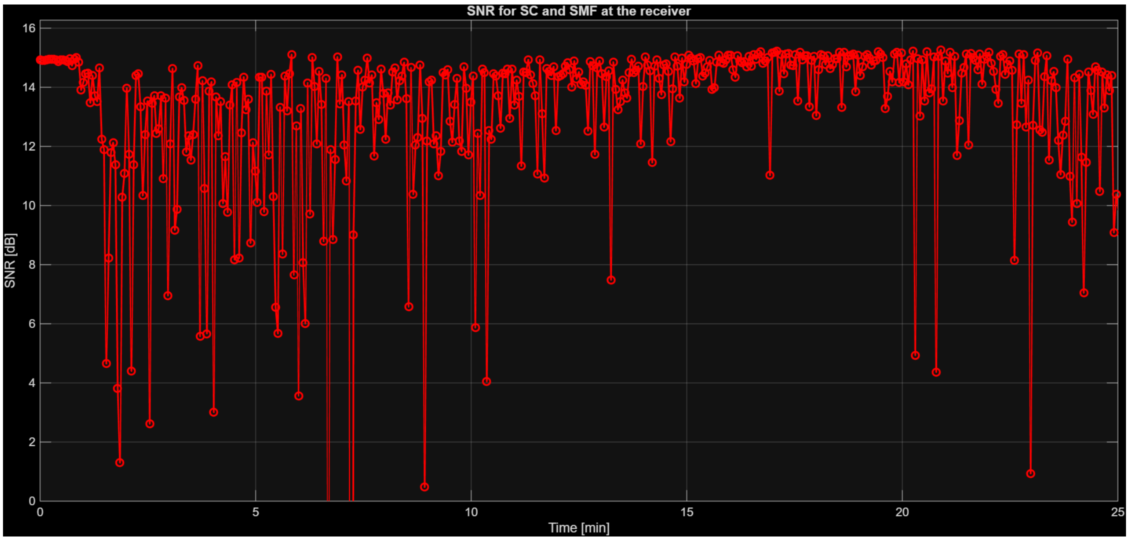

Figure 5.8: Plot of the SNR evolution with respect to time under turbulence with SMF-based receiver.

Furthermore, in addition to SNR and NGMI, in this stage also there is also an analysis of the BER as a direct indicator of decoding feasibility under turbulence-impaired conditions.

The SNR evolution in Figure 5.8 clearly reflects the turbulence-induced power fluctuations described in Chapter 4. In the first 10 minutes, the received signal experiences several deep fades: starting from about 15 dB, the SNR exhibits abrupt drops, reaching values close to 0 dB around minute 7. These events are consistent with strong scintillation and beam wander at the chamber inlet, where the optical spot occasionally moves outside the effective core area of the SMF.

In the central portion of the acquisition (approximately minutes 11 to 22), the received power becomes significantly more stable, and the SNR remains higher then 10 dB most of the time. Toward the end of the experiment, additional fading events again reduce the link quality, confirming the inherently time-varying nature of turbulence in heated-chamber conditions.

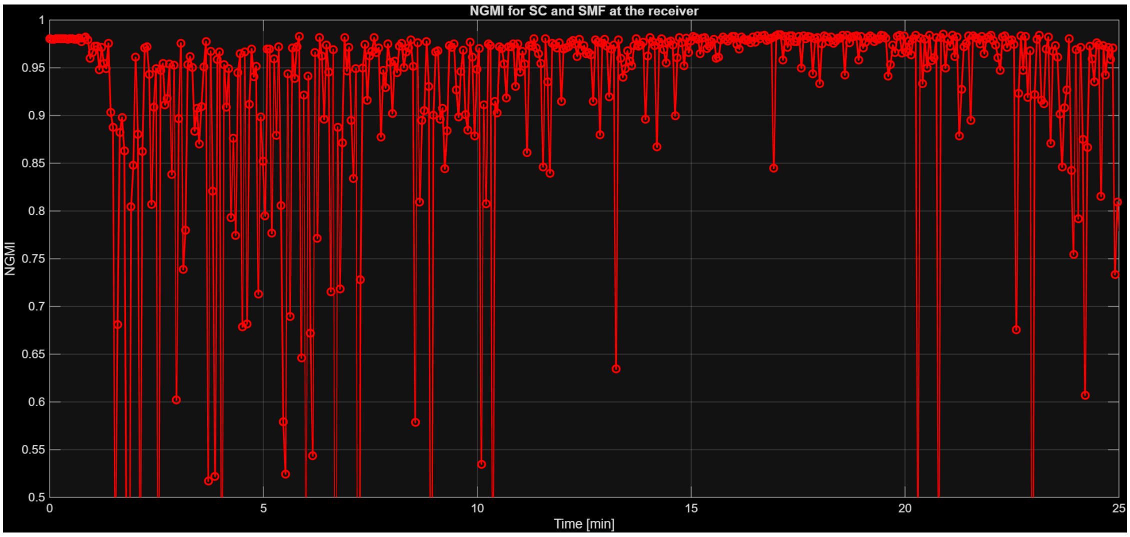

Figure 5.9: Plot of the NGMI evolution with respect to time under turbulence with SMF-based receiver.

The NGMI in Figure 5.9 profile closely follows the SNR dynamics, as expected for a 16-QAM system operating under varying received power. During the initial phase, turbulence-induced fading causes the NGMI to drop rapidly, mirroring the severe SNR dips. However, in the central part of the time window, the more stable interval of the experiment, the NGMI remains consistently above 0.8, indicating that the modulation format remains well within typical soft-decision FEC operating regions. The subsequent degradation at the end of the experiment further confirms that performance is dominated by the temporal fluctuations of the received optical power.

The BER in Figure 5.10 curve also reflects the same temporal structure observed in the SNR and NGMI trends. In the first part of the acquisition, severe turbulence leads to high error rates, reaching the 0.5 threshold around minute 7, which corresponds to a completely unreliable symbol detection regime. In the central section of the test, where SNR and NGMI are stable, the BER significantly improves and remains in a region compatible with FEC-assisted recovery. Toward the end of the experiment, the BER worsens again as additional deep fades occur. Overall, the BER confirms that link reliability heavily depends on the temporal statistics of turbulence when only a SMF is used at the receiver.

5.6 Experiment with Single-Carrier signal with Turbulence and Analysis of the Fundamental Mode of the MPLC

In the fourth experimental stage, the same turbulence-impaired propagation conditions are maintained, but the reception is now performed through the MPLC-based spatial demultiplexer, as depicted in Figure 5.11, operated initially in single-carrier mode. Only the fundamental HG_{00} output of the MPLC is used, enabling a direct comparison with

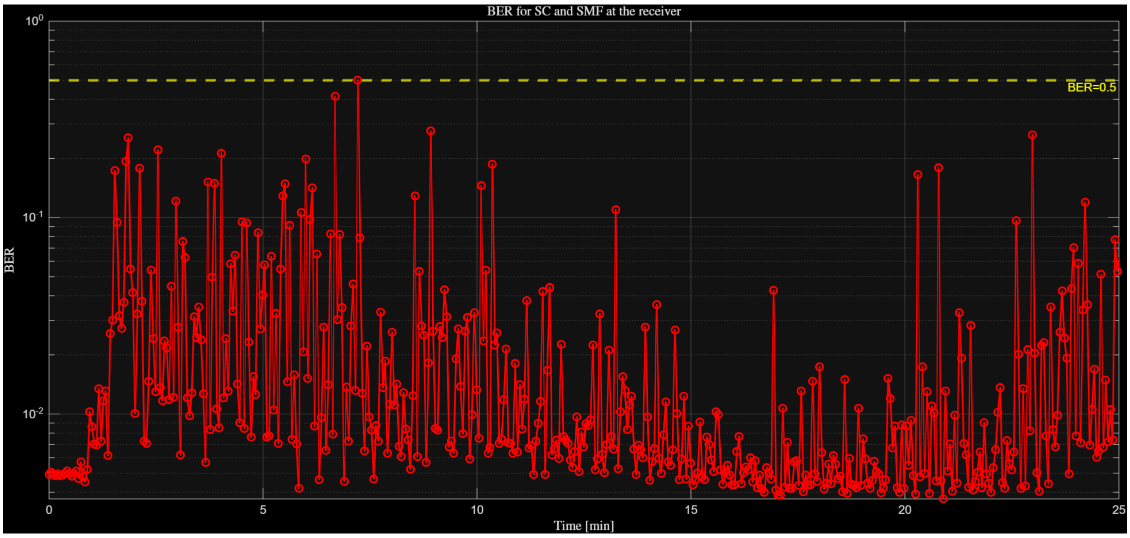

Figure 5.10: Plot of the BER evolution with respect to time under turbulence with SMF-based receiver.

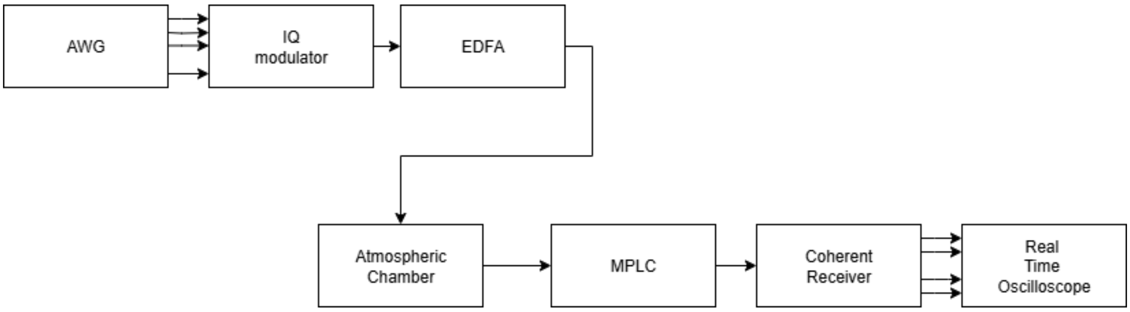

Figure 5.11: MPLC-based receiver setup.

the SMF-based reception while highlighting the insertion loss, modal filtering, and spatial selectivity inherent to the MPLC. In this configuration, the few-mode fiber (FMF) feeding the MPLC is directly connected to the receiving collimator, whereas the HG_{00} output fiber is routed to the coherent receiver.

The SNR profile in Figure 5.12 for the fundamental HG_{00} mode detected through the MPLC shows similar performance compared to the SMF case. While the initial portion of the acquisition still exhibits some turbulence-induced fluctuations, the amplitude of SNR drops is reduced, rarely falling below 4 dB. In the central section of the experiment (minutes 11–22), the SNR stabilizes over 12 dB, slightly higher and more consistent than the SMF results. This indicates that even when only the fundamental mode is selected, the MPLC provides intrinsic modal filtering and mitigates part of the wavefront distortions, reducing the severity of fading events.

The NGMI trend largely mirrors the improved SNR behavior. During the early minutes, NGMI again dips very much, but during the central part of the test it goes only once below 0.9 corresponding to moderate turbulence events, demonstrating a robust

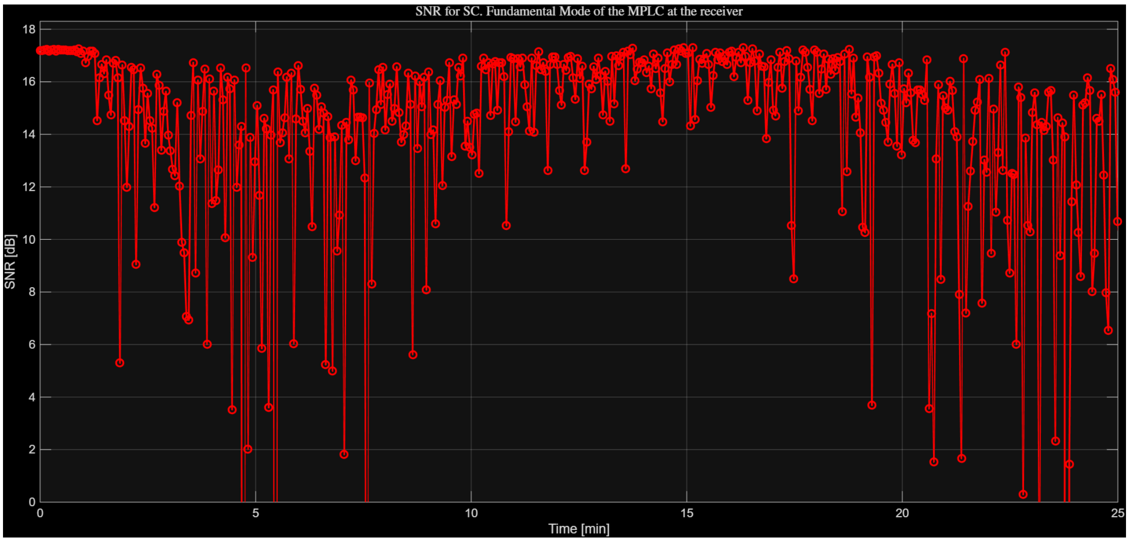

Figure 5.12: Plot of the SNR with respect to time for the fundamental HG_{00} mode detected through MPLC

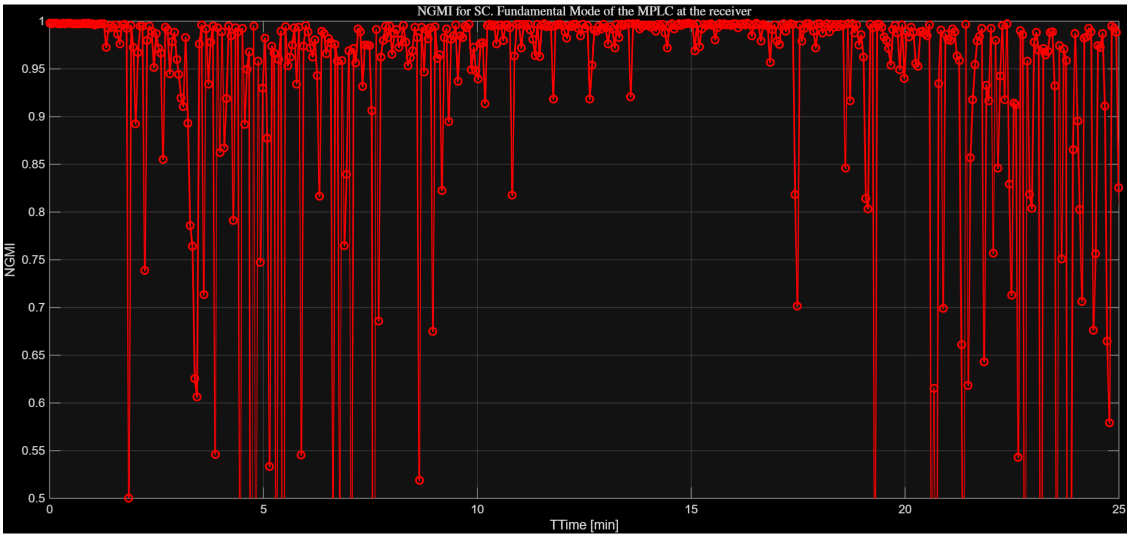

Figure 5.13: Plot of the NGMI with respect to time for the fundamental HG_{00} mode detected through MPLC

information-theoretic performance. This contrasts with the SMF scenario, where NGMI exhibited deeper and more frequent drops, highlighting the MPLC's ability to selectively transmit the least affected spatial component of the wavefront.

The BER evolution confirms the trends observed in SNR and NGMI. Initial fluctuations produce transient error spikes, also approaching the critical 0.5 threshold. In the central portion of the test, BER remains consistently low, indicating reliable symbol detection. Overall, using the fundamental mode of the MPLC provides a tangible

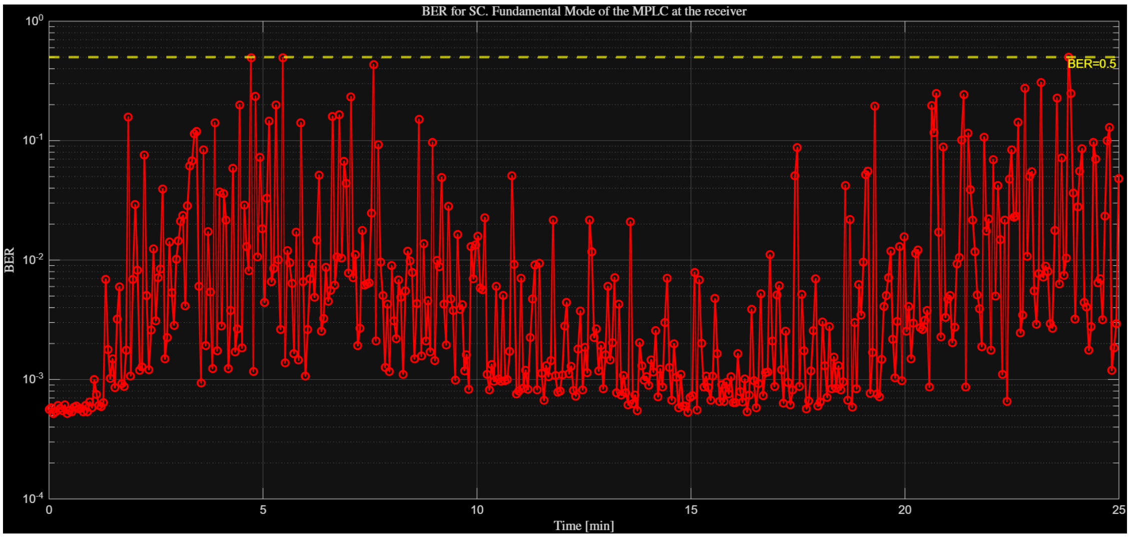

Figure 5.14: Plot of the BER with respect to time for the fundamental HG_{00} mode detected through MPLC

improvement in link reliability under thermal turbulence, even without employing multimode combination strategies.

5.6.1 Comparison: Fundamental Mode vs SMF

In this subsection, the system performance of the SMF and the fundamental HG_{00} mode detected through the MPLC is directly compared under very similar turbulent propagation conditions. The comparison is shown across three complementary metrics: SNR (Figure 5.21), NGMI (Figure 5.22), and BER (Figure 5.23).

In all plots, the SMF trace is displayed in red, while the fundamental mode of the MPLC is shown in white, allowing a clear visual assessment of the performance differences introduced by modal filtering.

There is a The SNR profile highlights a tangible advantage of the fundamental mode: it remains higher throughout the acquisition and exhibits reduced amplitude fluctuations compared to the SMF. Deep fades are less frequent, and the central portion of the measurement shows a more stable SNR around 16–17 dB. This improvement is attributable to the MPLC's ability to project the incoming distorted wavefront onto the least-affected spatial component, effectively mitigating some turbulence-induced fading events.

The NGMI trend mirrors the SNR behavior, confirming the improved information-theoretic performance. While both the SMF and the fundamental mode experience early turbulence-induced degradations, the MPLC output rarely dips below 0.9 during the central segment of the acquisition, whereas the SMF exhibits more frequent and deeper reductions. This demonstrates that even selecting a single mode at the receiver provides a notable enhancement in link reliability and capacity utilization.

Finally, the BER evolution reinforces these observations. The fundamental mode maintains consistently lower error rates, with only transient spikes approaching the 0.5

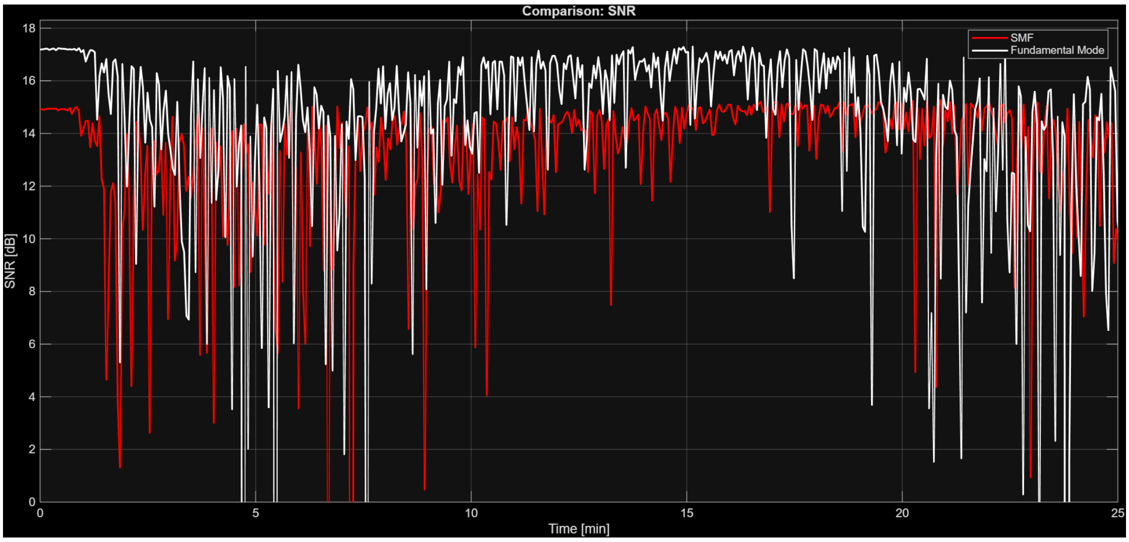

Figure 5.15: Plot of the SNR variations with respect to time: comparison of the SMF-based receiver (red curve) with MPLC-based receiver employing only the fundamental HG_{00} mode (white curve).

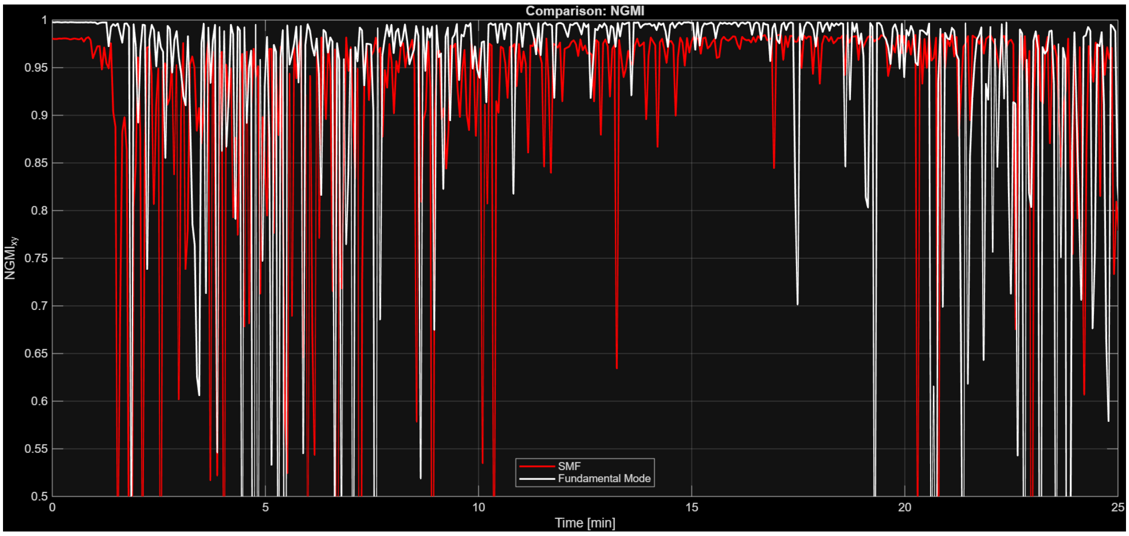

Figure 5.16: Plot of the NGMI variations with respect to time: comparison of the SMF-based receiver (red curve) with MPLC-based receiver employing only the fundamental HG_{00} mode (white curve).

threshold in the first few minutes, whereas the SMF shows more pronounced and frequent error increases. Across the entire measurement, the fundamental mode selected by the MPLC (HG_{00}) ensures a more robust symbol detection, validating the practical benefit of using MPLC-based modal selection to mitigate the effects of turbulence, even when no multi-mode combination is applied.

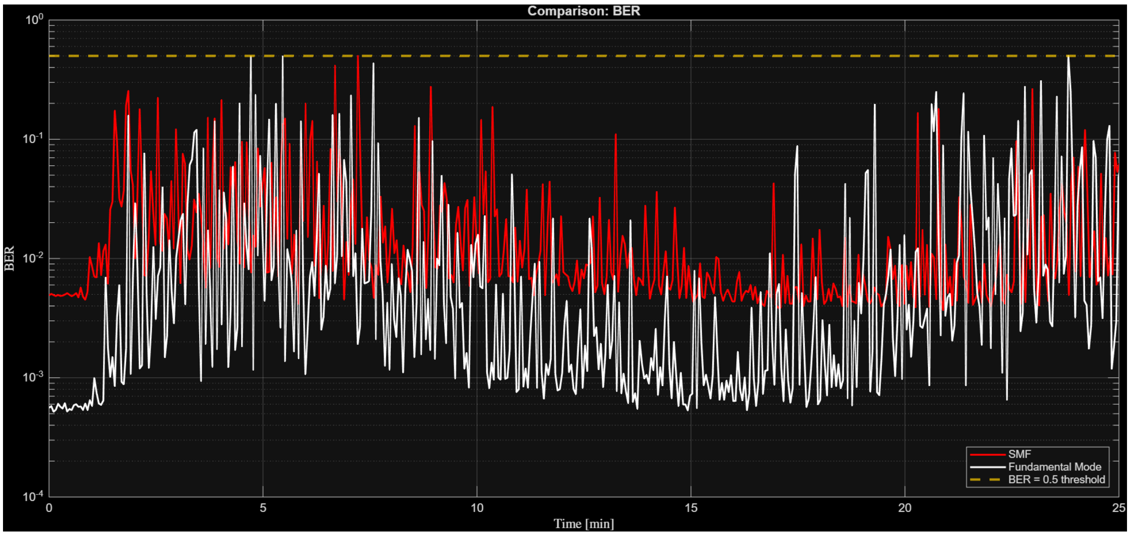

Figure 5.17: Plot of the BER variations with respect to time: comparison of the SMF-based receiver (red curve) with MPLC-based receiver employing only the fundamental HG_{00} mode (white curve).

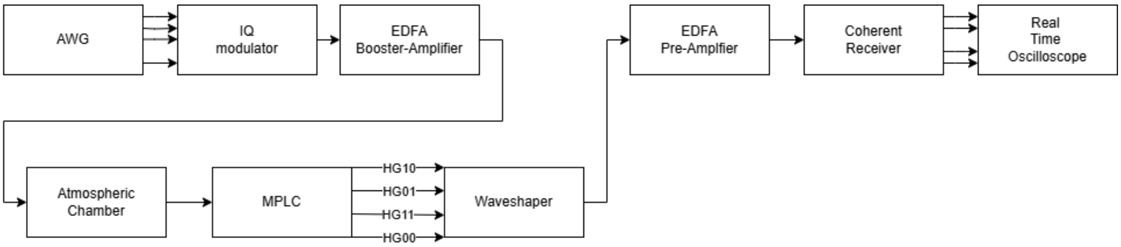

Figure 5.18: MPLC demultiplexing based receiver setup with the four selected modes.

5.7 Experiment with Multi-Carrier signal with Turbulence and Analysis of the Four best modes selected by the MPLC

In the final and most relevant experimental configuration, a four-subcarrier diversity scheme is implemented to counteract turbulence-induced fading in a coherent FSO link. The transmission remains strictly single-mode: no spatial multiplexing is used, and the entire optical field is launched in the fundamental Gaussian mode.

The diversity comes from the electrical domain. Instead of transmitting different data streams, the same information is replicated over four independent subcarriers. Each subcarrier experiences the turbulence-induced fading slightly differently. By repeating the same data over multiple subcarriers and combining the corresponding received signals, the system effectively averages out the independent fading contributions, reducing the probability of deep fades and improving the overall robustness of the link.

In this thesis, SCM is not employed to increase spectral efficiency but to introduce controlled redundancy for diversity purposes. Building upon the diversity-enabled subcarrier multiplexing approach previously demonstrated using three LP modes and a photonic lantern, the present work extends the concept to a four-branch scheme operating on a set of orthogonal HG modes and using an MPLC device as the mode demultiplexer.

The transmitted information block is replicated over four subcarriers.. After free-space propagation through turbulence, the received field is coupled into the mode demultiplexing stage, where the MPLC separates the optical signal into the HG_{00}, HG_{10}, HG_{01}, and HG_{11} modal components. Because the four subcarriers occupy different frequencies, their spectra remain non-overlapping after demultiplexing, preventing intermodal interference even though all subcarriers propagate in the same spatial mode at transmission.

Each HG branch carries a single assigned subcarrier, which is filtered and individually detected. Owing to turbulence-induced fading being only partially correlated across spatial modes, the four independently faded replicas of the same information can be recombined at the digital stage. After coherent detection and digital demultiplexing, the baseband subcarrier components are processed by a MISO equalizer that performs coherent combining, compensating for residual amplitude, phase, and polarization mismatches among the modal branches.

This SCM-enabled non-interfering diversity-combining scheme therefore generalizes previous 3-branch LP-based demonstrations to a four-branch HG-based architecture using an MPLC receiver. The approach provides enhanced robustness to turbulence at the expense of reduced spectral efficiency, as part of the available bandwidth is intentionally used to transmit redundant copies of the same data. This approach conceptually extends previous multi-subcarrier experiments reported in the literature [13], where three subcarriers were launched over a turbulent FSO channel and subsequently demultiplexed by a photonic lantern into their respective constituent LP modes (LP01, LP11a, LP11b). The key idea behind this diversity-oriented approach is that different spatial modes experience partially uncorrelated turbulence-induced fading. As a result, when multiple modes are captured at the receiver, their fluctuations do not add coherently: deep fades affecting one mode are often compensated by higher power in the others. By recombining these modal components, the receiver effectively averages out the scintillation, achieving a more stable optical power compared with using a single spatial mode only. In contrast, this implementation employs four SCs, demultiplexing is performed by a MPLC, and the spatial decomposition is realized over the Hermite–Gaussian basis HG_{00}, HG_{10}, HG_{01}, HG_{11}, selected according to the modal projection of the received wavefront.

The entire setup is depicted in Figure 5.18. The modal processing occurs entirely at the receiver: the free-space beam collected by the collimator is coupled into the FMF feeding the MPLC, which operates in demultiplexing mode. Each HG spatial component is delivered to a dedicated SMF output, subsequently entering the Waveshaper (Finisar WS4000S), a programmable optical filter whose channels can be configured in MATLAB to select and shape specific spectral bands. The Waveshaper's four inputs act as narrowband filters, isolating each SC and associating it with the HG mode through which it is predominantly received. No weighting, shaping, or equalization is applied at this stage, the Waveshaper performs selection only. The filtered outputs are then recombined into the single output (4-in / 1-out) of the Waveshaper, but they are still spectrally separated,

Figure 5.19: Fiber fixed to the outside wall.

and sent through a pre-amplifier EDFA, ensuring a constant received power between –3 and –1 dBm at the coherent receiver front-end.

After coherent detection, the DSP digitally separates the four modal sub-carriers and performs MISO-style combining of the four replicas of the same transmitted waveform, implementing modal diversity combining. Although the transmission is single-mode, the receiver exploits multiple spatial projections of the same signal, each experiencing distinct turbulence-induced fading due to the differential propagation sensitivity of the HG modes. Pre-channel power measurements confirm that HG_{00} starts with the highest received power, HG_{10} and HG_{01} exhibit intermediate and comparable levels, and HG_{11} is initially the weakest.

This architecture enables a diversity-combining coherent FSO receiver under thermal turbulence. Beyond comparing the overall performance against single-branch reception, the MISO-based DSP allows enabling or disabling each of the four spatial branches individually, providing a controlled assessment of the incremental contribution of each HG mode to the final combined signal. By progressively summing the SC replicas—first two modes, then three, and finally all four—it is possible to quantify the robustness improvement each spatial component contributes against scintillation and deep fades.

5.7.1 Measured Optical Power Levels Across the Modal-Diversity Chain

Before conducting the four-branch modal-diversity experiment, all optical power levels along the transmission and reception chain were carefully characterized to ensure correct operation of the MPLC demultiplexer, the Waveshaper, and the coherent receiver. Table 5.1 summarizes the measured powers at the key points of the setup. At the transmitter side, the modulator provides an output power of −13 dBm, which is boosted by

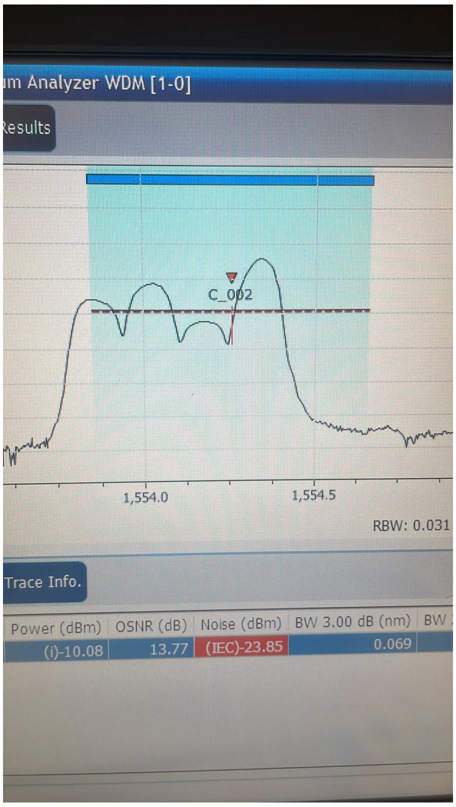

Power (dBm)	OSNR (dB)	Noise (dBm)	BW 3.00 dB (nm)	BW
(i)-10.08	13.77	(IEC)-23.85	0.069	

Figure 5.20: Power levels in the Waveshaper measured at the output of the MPLC before starting the test.

an EDFA with a gain of 27 dB, yielding 13.2 dBm at its output and 11.9 dBm at the entrance of the atmospheric chamber. This loss is induced by the long fiber showed in Figure 5.19 employed to go from the first lab, where the signal is generated, to the second lab where there are the atmospheric chambers.

Before starting the emulation with turbulent propagation and coupling into the FMF feeding the MPLC, the four spatial modes emerge with significantly different power levels. At the input of the Waveshaper, the measured modal powers are:

$$P_{HG_{10}} = -3.0 \text{ dBm}, \quad P_{HG_{01}} = -1.8 \text{ dBm}, \quad P_{HG_{11}} = -6.2 \text{ dBm}, \quad P_{HG_{00}} = 3.2 \text{ dBm},$$

confirming the dominance of the fundamental mode and the progressively lower power carried by higher-order modes.

This difference of power has been measured with an optical spectrum analyzer, as shown in Figure 5.20.

The output power of the Waveshaper is −11.5 dBm, further reduced to −12.8 dBm at the input of the pre-amplifier due to the long fiber used to come back to the first lab. An EDFA with 11 dB gain is therefore used to restore the received power to the desired range required for safe operation of the coherent receiver, in particular the power at the input of the receiver was set to be −2.5 dBm.

Table 5.1: Measured optical power levels along the modal-diversity measurement setup.

Measurement point	**Power [dBm]**
Modulator output	−13
EDFA booster output	13.2
Input to atmospheric chamber	11.9
Waveshaper input — per mode:	
HG_{00}	3.2
HG_{01}	−1.8
HG_{10}	−3.0
HG_{11}	−6.2
Waveshaper output	−11.5
Input to pre-amplifier	−12.8
Input to coherent receiver (after pre-amp)	−2.5

These measurements provide the reference operating conditions for the diversity-combining analysis and explain the relative contributions expected from each modal branch in the MISO DSP.

5.7.2 Results of Multi-Carrier Modal-Diversity Application

In this section, we present the temporal evolution of the key performance metrics—SNR, NGMI, and BER—for the multi-sub-carrier (MSC) modal-diversity emulation. Two distinct cases are analyzed to show the improvemets:

- the input to the MISO DSP consists only of the two spatial modes with the lowest initial power, namely HG_{10} and HG_{11};
- the input includes all four selected spatial modes, HG_{00}, HG_{01}, HG_{10}, and HG_{11}, allowing full diversity combining.

An intermediate scenario, in which three modes (HG_{10}, HG_{11}, HG_{01}) were combined, did not provide significant improvements relative to the white-curve case. For clarity and conciseness, it has therefore been omitted from the figures. This approach highlights the progressive performance enhancement achievable by increasing the number of modes in the diversity combination, directly illustrating the impact of modal selection on mitigating turbulence-induced impairments in the FSO link.

The results of the multi-carrier modal-diversity emulation clearly demonstrate the advantage of combining multiple spatial modes at the receiver. Figure 5.21 shows the SNR evolution over time. The red curve, representing the combination of all four modes, is consistently higher than the white curve, which includes only the two weaker modes. Notably, the red curve exhibits smaller and less frequent drops in SNR, besides the one after 3 minutes, which is present in all cases and it's probably due to some misalignments. It demonstrates the benefit of including additional spatial modes to mitigate turbulence-induced fading and distortions. As depicted in Figure 5.22, the NGMI trend closely follows the improvements observed in SNR. The red curve remains near unity for most

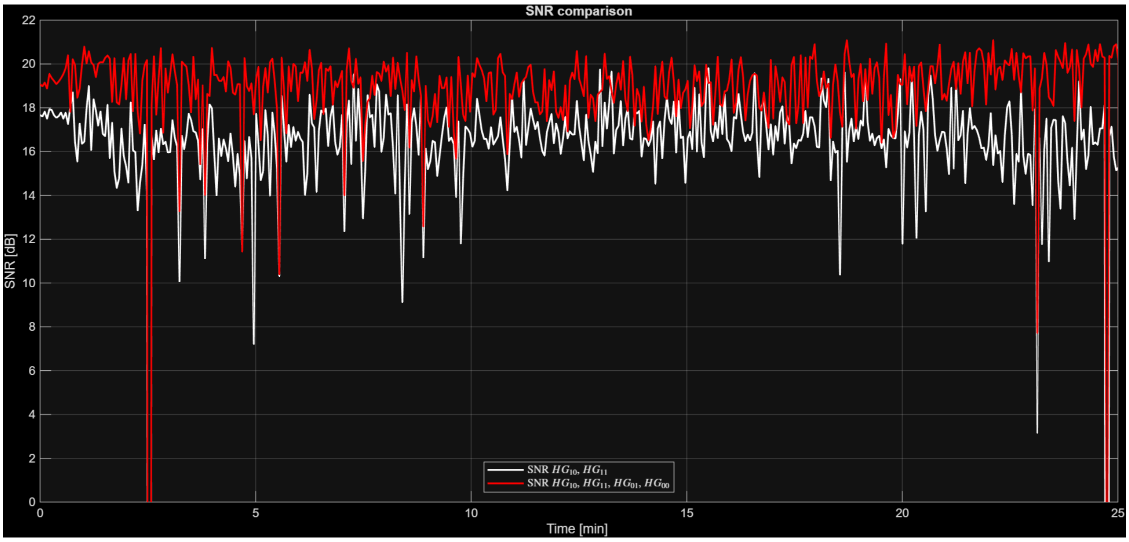

Figure 5.21: Plot of the SNR evolution over time for the MISO multi-carrier emulation. The curve of the two spatial modes with the lowest initial power (white curve) is compared with the case with the four selected modes (red curve).

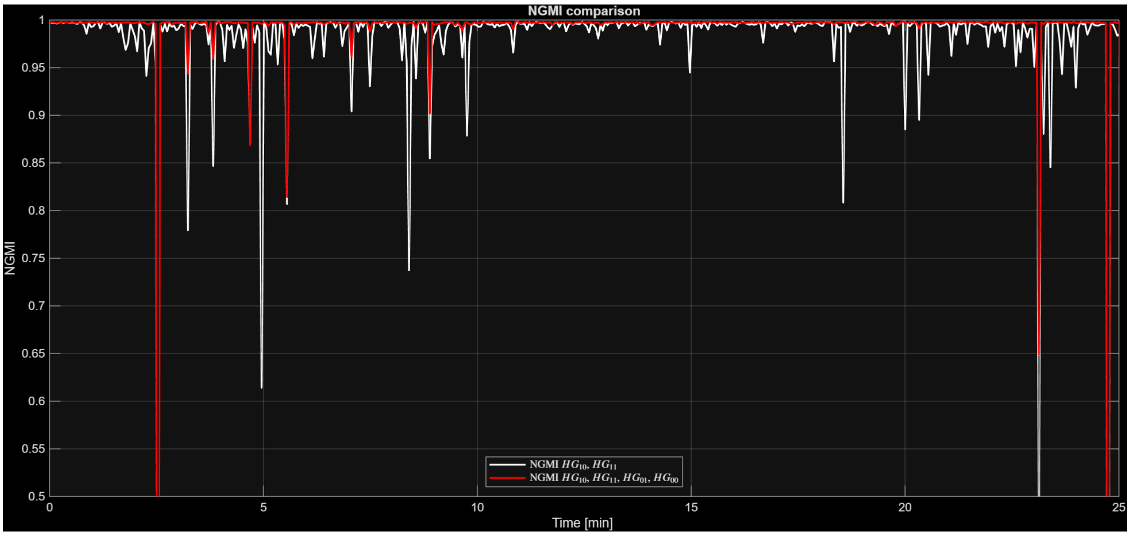

Figure 5.22: Plot of the NGMI evolution over time for the MISO multi-carrier emulation. The curve of the two spatial modes with the lowest initial power (white curve) is compared with the case with the four selected modes (red curve).

of the 25-minute acquisition, falling below the 0.8 threshold only once at the beginning during a strong turbulence event and twice towards the end. The white curve shows deeper and more frequent drops, highlighting the advantage of combining multiple modes to enhance information-theoretic performance under turbulent conditions. Figure 5.23 illustrates the BER evolution. The red curve, corresponding to all four modes, remains

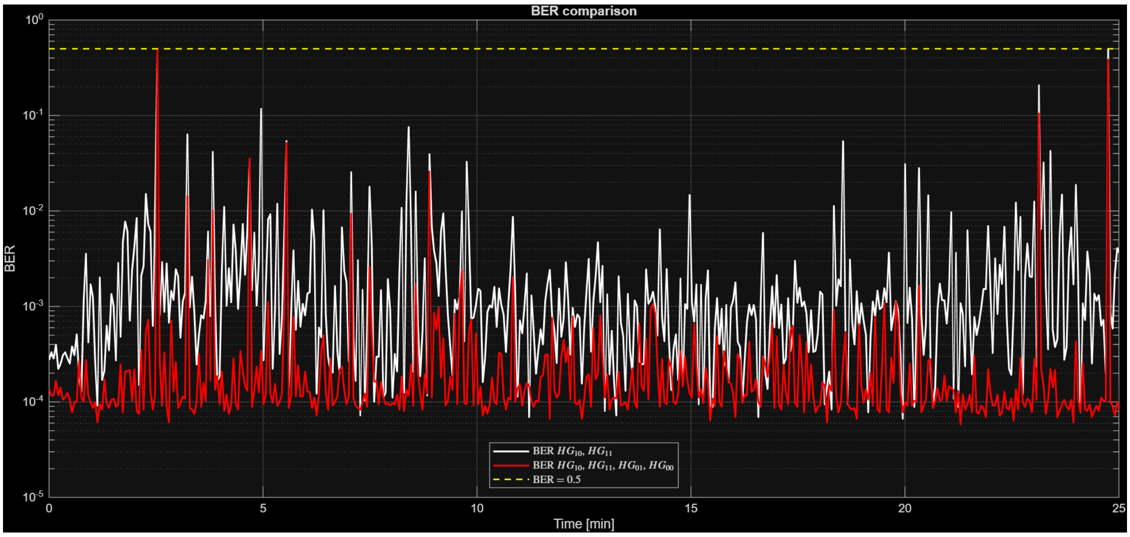

Figure 5.23: Plot of the BER evolution over time for the MISO multi-carrier emulation. The curve of the two spatial modes with the lowest initial power (white curve) is compared with the case with the four selected modes (red curve).

consistently lower than the white curve. Many of the transient error peaks observed in the white curve are suppressed in the red curve. This demonstrates that using multiple HG modes reduces severe error events and enhances the reliability of symbol detection.

Overall, the performance gains are attributed to the increased number of inputs to the MISO DSP and the exploitation of multiple spatial modes, which effectively average out mode-specific turbulence distortions, implementing a form of spatial diversity.

Chapter 6

Conclusion

6.1 Overview

This thesis presented a comprehensive experimental investigation focused on improving the resilience of coherent FSO communication links through receiver-side spatial-mode processing. The overarching objective was to demonstrate how modal diversity—enabled by an MPLC—can mitigate turbulence-induced impairments without requiring multiple transmitters.

The work was structured across three progressively connected experimental stages. First, the MPLC was characterized in a controlled environment to assess its practical suitability as a spatial demultiplexer. Measurements of insertion loss, polarization dependence, fiber bending sensitivity, and inter-modal crosstalk provided a detailed understanding of its operational behavior. This analysis was instrumental in identifying the most suitable spatial modes—specifically the first four Hermite–Gaussian modes—used in the subsequent communication experiments. The second stage examined the effects of thermal turbulence on optical power fluctuations using a dual-chamber atmospheric emulator. Three receiver configurations were compared: a standard SMF, a photonic lantern, and the MPLC. By analyzing instantaneous power, moving averages, and the Rytov variance, this stage quantified the fading behavior of each architecture and demonstrated how spatial demultiplexing inherently captures partially uncorrelated fluctuations across modes. Finally, the full communication chain was tested under coherent detection. A 16-QAM signal was propagated through the turbulent channel, and the received signal was processed through advanced DSP. Performance was evaluated in terms of SNR, BER, and NGMI across progressively more capable reception schemes: SMF detection, MPLC-based single-mode extraction, and ultimately a four-branch modal-diversity configuration in which multiple Hermite–Gaussian modes were recombined through MISO DSP. This final stage showed the concrete benefit of modal diversity, significantly improving link stability and error performance.

Taken together, these three stages form a cohesive experimental framework that bridges device-level characterization, turbulence modeling, and system-level communication performance. The results confirm that MPLC-enabled mode decomposition is not merely a theoretical construct, but a viable and powerful approach for enhancing the robustness of coherent FSO systems operating in the presence of atmospheric turbulence.

6.2 Summary of Main Experimental Contributions

The experimental work developed in this thesis can be grouped into three major contributions, each addressing a different layer of the problem: device-level behavior, turbulence-induced fading, and coherent communication under atmospheric distortion. Taken together, these results not only validate the use of MPLC-based receivers for FSO systems, but demonstrate a progressive and quantifiable improvement in link stability and robustness as spatial processing is introduced and expanded.

(1) MPLC Characterization and Benchmarking The first experimental campaign provided a detailed laboratory characterization of the MPLC, establishing its suitability as a spatial-mode demultiplexing unit for Hermite–Gaussian modes. The measured insertion loss confirmed its compatibility with practical receiver chains, while the analysis of polarization sensitivity demonstrated a clear advantage over photonic lanterns in scenarios where the input state of polarization is not actively controlled. Additionally, the modal correlation analysis revealed low cross-talk among the selected HG basis, validating the orthogonality and stability of the modal set HG_{03}, HG_{02}, HG_{12}, HG_{01}, HG_{00}, HG_{11}, HG_{10}, HG_{21}, HG_{20}, HG_{30}.

This provided the foundation for later communication experiments by confirming that the MPLC can reliably decompose distorted wavefronts into well-isolated spatial channels.

(2) Power Distribution and Turbulence Impact via Atmospheric Chamber The second contribution involved the controlled emulation of thermal turbulence using a dual-chamber setup. Here, received power fluctuations were measured over 25-minute sequences using three different receiver configurations: a single-mode fiber, a photonic lantern, and an MPLC. The comparison demonstrated the limitations of classical SMF reception under scintillation and beam wander, while the PL offered partial modal capture but suffered from polarization-dependent coupling and mode imbalance. The MPLC, on the other hand, provided a richer and more informative modal decomposition, enabling a finer understanding of turbulence-induced fading mechanisms. The Rytov variance was used to quantify the turbulence strength and link it to the temporal received power patterns, marking one of the first detailed comparisons of modal receivers under controlled thermal turbulence for coherent FSO links. Crucially, these measurements enabled the selection of the four most resilient HG modes, which were subsequently used in the final communication experiments presented in Chapter 5.

(3) Coherent Communication Under Progressive Receiver Architectures The final contribution extended the analysis to full coherent transmission at 64 Gbaud or 60 Gbaud using 16-QAM modulation. Beginning with back-to-back tests and chamber-only propagation, the experiments then progressed to turbulence-impaired reception through SMF, MPLC fundamental-mode filtering, and ultimately a four-branch modal-diversity emulation. In each scenario, SNR, BER, and NGMI were extracted over time, revealing a clear hierarchy of performance: SMF suffered deep fades and unstable decoding, MPLC fundamental-mode detection mitigated fading and reduced error bursts, and the multi-carrier modal diversity approach provided the highest robustness, maintaining high NGMI and low BER for the majority of the experiment. Importantly, the DSP framework allowed also selective enabling of modal branches, making it possible to quantify the incremental diversity gain introduced by each spatial mode.

6.3 Critical Discussion

The experimental results reported in this thesis support the central hypothesis that spatial-mode decomposition and modal diversity can significantly improve the resilience of coherent FSO links under turbulence. However, a deeper analysis reveals that these gains emerge from a combination of physical and architectural factors, each carrying specific trade-offs.

A first observation concerns the MPLC itself. While the device proved effective in separating mode content even under strong distortions, its insertion loss remains a practical limitation. Although acceptable in laboratory conditions, a real deployment would require either optical link margins capable of absorbing these losses or improved MPLC designs with lower attenuation per plane. On the other hand, the MPLC exhibited a clear advantage over the photonic lantern in terms of polarization insensitivity, which is critical for FSO channels where the input state of polarization evolves unpredictably. This reinforces the idea that spatial demultiplexing cannot rely only on fiber-inherited mode coupling principles when operating in free space.

Concerning turbulence, the analysis of received power confirmed that fading in FSO channels is not uniform across spatial modes. The HG basis provides independent projections of the distorted wavefront, but these projections do not share equal reliability. In particular, HG_{00} consistently demonstrated stronger power coupling, while higher-order modes were more insensitive to wavefront distortions only when turbulence reaches important levels. This heterogeneity is not a limitation—in fact, it enables diversity. The weak performance of a mode during deep fades can be compensated by another mode whose spatial structure overlaps differently with the distorted beam. Still, this implies that a modal-diversity system must operate over a sufficiently rich mode set to provide meaningful diversity gain.

The transition from single-mode reception to MPLC-assisted detection highlights an important conceptual point: even selecting only the fundamental mode offers measurable performance improvements. This is not merely a filtering effect but the result of spatial matching. The MPLC is performing a projection that isolates the most stable component of the optical field, while the SMF blindly couples whatever light reaches its core—often dominated by wavefront distortions rather than useful signal. This result suggests that mode demultiplexing may be beneficial even when only one mode is ultimately detected.

The greatest performance gains, however, emerged from the multi-carrier modal-diversity architecture. By launching multiple replicas of the signal and recovering them through orthogonal spatial modes, a form of MISO combining could be applied in the digital domain. This approach does not increase spectral efficiency, but it dramatically improves link robustness—particularly in the temporal domain—by mitigating deep fades that would otherwise cause burst errors or decoding failures. The observation that the performance improves progressively as more modes are included is a direct indicator that turbulence acts partially independently across modal projections.

Yet this approach also introduces system-level complexity. Managing four subcarriers requires increased bandwidth in both the transmitter and receiver, and the DSP must handle multi-input signal separation and combining. In a real deployment, this would translate into higher hardware cost and power consumption.

In conclusion, the findings of this work confirm that MPLC-based spatial processing can significantly improve the performance of coherent FSO links operating under turbulence. The approach is not without trade-offs, but the diversity gain demonstrated experimentally suggests that the technique is not merely of academic interest—it constitutes a promising avenue for designing more resilient optical wireless communication systems.

6.4 Implications for Future FSO Systems

The results achieved in this thesis have direct implications for the design of next-generation FSO communication systems, particularly those targeting high-capacity coherent links in turbulent environments. The demonstrated ability of the MPLC to spatially decompose the received field into orthogonal Hermite–Gaussian modes suggests that mode-selective reception can serve as a powerful alternative to traditional turbulence mitigation techniques such as adaptive optics or aperture diversity. Unlike solutions requiring mechanical steering or complex wavefront correction, MPLC-based reception operates entirely in the optical domain without requiring dynamic elements.

From an implementation perspective, the experimental results show that even single-mode extraction through the MPLC yields an improvement over classical SMF-based reception, indicating that the approach may be beneficial even in systems not equipped for full modal diversity. This could enable hybrid receivers where a low-loss modal filter acts as a turbulence-aware spatial equalizer, improving sensitivity without requiring additional spatial channels.

In applications where link stability is paramount—such as ground-to-satellite links, inter-building urban FSO backhaul, or maritime optical links—the multi-branch modal-diversity architecture demonstrated here offers a promising path to robustness. By exploiting the partial statistical independence between modal projections, the receiver behaves as a spatially selective field sampler, preserving information even when the total collected power is heavily distorted.

However, the integration of MPLC-based modal diversity in practical systems requires addressing several engineering challenges. Mode-selective receivers must be paired with coherent front-ends capable of multi-input DSP processing, and system designers must balance diversity gain with power consumption, hardware complexity, and optical insertion loss. Scalable architectures—potentially combining photonic integration, low-loss multi-plane conversion, and shared coherent processing—will be key to deploying such systems beyond laboratory settings.

Looking forward, the outcomes of this work suggest that future FSO systems need not rely solely on better transmit-side optics or passive aperture scaling. Instead, receiver-side spatial intelligence, enabled through optical mode decomposition, offers a complementary pathway toward turbulence-resilient coherent communication. As spatial-mode optics continues to mature, MPLC-based modal filtering and diversity combining may become standard building blocks in high-performance free-space links.

6.5 Future Work

The results obtained in this thesis open several directions for future investigation, aimed at further improving the resilience and applicability of spatial-mode-based reception in coherent FSO systems.

A first natural extension involves exploiting the full modal capability of the MPLC. Although the present work focused on four Hermite–Gaussian modes, the device supports up to ten spatial outputs. A future experimental campaign could therefore investigate the benefits and limitations of operating with the complete modal set, assessing how much additional diversity gain can be extracted and whether higher-order modes provide meaningful performance improvements under strong turbulence. Such an analysis would also clarify whether there is an optimal trade-off between modal richness and receiver complexity, particularly as insertion loss increases for higher-order modes.

Another important development would be the inclusion of forward error correction in the transmission chain. In this thesis, NGMI served as a reliable predictor of post-FEC performance, but implementing actual soft-decision decoding would allow direct evaluation of net error rates and operational margins. This would also enable comparing diversity gains with coding gains and exploring their combined benefits in a unified performance framework.

With respect to the physical test environment, the atmospheric chamber provided a controlled and repeatable way to emulate thermal turbulence. However, real-world propagation conditions involve additional impairments, including wind-driven turbulence, temperature gradients, platform motion, and pointing inaccuracies. Extending the experiments to outdoor links—or to laboratory setups capable of reproducing such dynamics—would provide valuable validation of the modal diversity approach under realistic deployment conditions.

Finally, while the MPLC proved effective in demultiplexing spatial modes, its insertion loss remains a structural constraint. Moreover, each spatial mode exhibits a different intrinsic loss, which shapes the power balance at the receiver and ultimately affects the achievable diversity gain. Although the device cannot be redesigned within the scope of this work, future investigations could explore link budgets and amplification strategies optimized around the known modal insertion profile, enabling practical assessments of system-level feasibility.

Overall, the work presented in this thesis lays the foundation for a broader exploration of spatial-mode processing in free-space optical links, with several clear paths for expanding both experimental capabilities and system-level understanding.

6.6 Final Remarks

This thesis has demonstrated that modal diversity, when implemented through an MPLC-based spatial demultiplexer, represents a powerful and practical strategy to enhance the robustness of coherent free-space optical links affected by atmospheric turbulence. By enabling the reception of multiple orthogonal projections of the same transmitted signal, the MPLC architecture effectively transforms turbulence-induced fading from a single-point failure into a multi-dimensional impairment—one that can be mitigated through diversity combining rather than merely endured.

Across all experimental stages, the MPLC consistently outperformed the single-mode fiber configuration, first by improving link stability when only the fundamental mode was detected, and ultimately by enabling multi-carrier modal combination that significantly reduced error bursts and preserved high signal quality even under severe fading. Unlike classical aperture enlargement or multi-aperture receivers, this approach achieves turbulence mitigation entirely in the spatial-mode domain, requiring neither multiple transmitters nor parallel coherent front-ends.

While insertion loss and mode-dependent coupling remain practical constraints, the results clearly show that the benefits of modal diversity outweigh these penalties—especially when multiple modes are digitally recombined to restore signal integrity. In this sense, the MPLC is not merely a mode separator, but an enabler of a new class of turbulence-resilient coherent receivers.

The work conducted here demonstrates that spatial-mode processing, made possible by devices like the MPLC, holds strong promise for the next generation of free-space optical systems, bridging the gap between theoretical capacity gains and experimentally validated performance improvements. At the receiver, where channel impairments are fully revealed, the MPLC offers not only a richer description of the distorted wavefront, but also a concrete path to overcome its limitations.

Acronyms

AWG Arbitrary Waveform Generator. 25, 26, 78

B2B Back-to-Back. 79–82

BER Bit Error Rate. 16, 24–26, 29, 30, 77, 83–87, 89, 93–95, 97–99

CW-SSIM Complex Wavelet Structural Similarity Index. 47, 53–57

DAQ Data Acquisition. 42, 45

DFB Distributed Feedback Laser. 37, 45

DSP Digital Signal Processing. 25–30, 78, 82, 91, 93, 95, 97, 99, 100

EDFA Erbium-Doped Fiber Amplifier. 25, 26, 82, 91, 92

FEC Forward Error Correction. 29, 77, 80, 84, 101

FMF Few Mode Fiber. 17–20, 23, 32, 37, 45, 63, 66, 85, 90, 92

FSO Free-Space Optical. 1, 5–8, 16, 17, 21–26, 28, 29, 31, 37, 59, 60, 77, 82, 90, 91, 93, 97–101

GMI Generalized Mutual Information. 29

HG Hermite-Gaussian. 7, 12–15, 18–21, 40, 46, 47, 49, 54, 90, 91, 95, 98, 99

LG Laguerre-Gaussian. 7, 12, 19

LP Linearly Polarized. 12, 17, 21, 22, 90

LUT Look-Up Table. 44

MDM Mode Division Multiplexing. 1, 6–8, 11

MISO Multiple-Input Single-Output. 13, 29, 91, 93–95, 97, 99

MPC Motorized Polarization Controller. 35, 37, 38, 40, 42, 44, 46

MPLC Multi Plane Light Converter. 1, 7–9, 11–13, 18–21, 25, 29–35, 37, 40, 45, 46, 56, 57, 59, 62, 66, 68–75, 77, 84–92, 97–102

NGMI Normalized Generalized Mutual Information. 25, 26, 29, 30, 77, 80, 82–88, 93, 94, 97–99, 101

OAM Orbital Angular Momentum. 6, 7, 12, 19

OI Overlap Integral. 47, 51, 53, 55

PL Photonic Lantern. 7–9, 11, 12, 17, 18, 25, 32–34, 37–40, 59, 62–65, 67, 68, 70, 73, 74, 98

RRC Root Raised-Cosine. 26, 28, 77

SC Single-Carrier. 26, 27

SCM Subcarrier Multiplexing. 26–28, 89

SMF Single Mode Fiber. 1, 7–9, 11, 16–21, 23, 25, 29, 31, 32, 37, 59, 60, 62, 63, 65, 67, 68, 70, 73–75, 77, 81–90, 97–100

SNR Signal-to-Noise Ratio. 8, 16, 24, 25, 30, 77, 79–88, 93, 94, 97, 98

SOP State of Polarization. 41–44, 54, 55

SSIM Structural Similarity Index. 51–54

VOA Variable Optical Attenuator. 79, 81

Bibliography

[1] Pritam Sahoo and Ajay Yadav. A comprehensive road map of modern communication through free-space optics. *Journal of Optical Communications*, -1, 12 2020.

[2] Hemani Kaushal and Georges Kaddoum. Optical communication in space: Challenges and mitigation techniques. *IEEE Communications Surveys Tutorials*, 19(1):57–96, 2017.

[3] Hamid Hemmati. *Near-Earth Laser Communications.* CRC Press, 2006.

[4] Larry C. Andrews and Ronald L. Phillips. *Laser Beam Propagation through Random Media.* SPIE Press, second edition, 2005.

[5] Arun K. Majumdar. *Free-Space Laser Communications: Principles and Advances.* Springer, 2014.

[6] Vitor D. Correia, Marco A. Fernandes, Paulo P. Monteiro, Fernando P. Guiomar, and Gil M. Fernandes. On the impact and mitigation of turbulence in fiber-coupled fso systems. *IEEE Access*, 12:69505–69516, 2024.

[7] V. I. Tatarskii. *Wave Propagation in a Turbulent Medium.* McGraw-Hill, 1961.

[8] R. Frehlich. Laser beam propagation in a turbulent atmosphere. *Journal of the Optical Society of America A*, 9(9):1723–1736, 1992.

[9] Robert K. Tyson. *Principles of Adaptive Optics.* CRC Press, 2010.

[10] Larry C. Andrews and Ronald L. Phillips. Laser beam scintillation with applications. *SPIE Press*, 1999.

[11] El-Mehdi Amhoud, Boon S. Ooi, and Mohamed-Slim Alouini. A unified statistical model for atmospheric turbulence-induced fading in orbital angular momentum multiplexed fso systems. *IEEE Transactions on Wireless Communications*, 19(2):888–900, 2020.

[12] Alan E Willner, Hanying Huang, Yingjie Yan, Yongxiong Ren, Naveed Ahmed, Guodong Xie, Cong Bao, Long Li, Yun Cao, Zijiao Zhao, and Jian Wang. Optical communications using orbital angular momentum beams. *Science*, 347(6224):144–149, 2015.

[13] Manuel M. Freitas, Marco A. Fernandes, Vitor D. Correia, Paulo P. Monteiro, Fernando P. Guiomar, and Gil M. Fernandes. Reliability enhancement in fso communications using fmf assisted by subcarrier multiplexing. In *2024 Optical Fiber Communications Conference and Exhibition (OFC)*, pages 1–3, 2024.

[14] T. A. Birks, I. Gris-Sánchez, S. Yerolatsitis, S. G. Leon-Saval, and R. R. Thomson. The photonic lantern. *Advances in Optics and Photonics*, 7(2):107–167, 2015.

[15] Nicolas K. Fontaine, Roland Ryf, Haoshuo Chen, David T. Neilson, Kwangwoong Kim, and Joel Carpenter. Laguerre-gaussian mode sorter. *Nature Communications*,

10(1), April 2019.

[16] Katsunari Okamoto. *Fundamentals of Optical Waveguides*. Academic Press, San Diego, CA, 2 edition, 2006.

[17] Bahaa E. A. Saleh and Malvin Carl Teich. *Fundamentals of Photonics*. Wiley, Hoboken, NJ, 3rd edition, 2019.

[18] Yuanhang Zhang and Nicolas K. Fontaine. Multi-plane light conversion: A practical tutorial, 2023.

[19] Antonin Billaud, Andrew Reeves, Adeline Orieux, Helawae Friew, Fausto Gomez, Stephane Bernard, Thibault Michel, David Allioux, Juraj Poliak, Ramon Mata Calvo, and Olivier Pinel. Turbulence mitigation via multi-plane light conversion and coherent optical combination on a 200 m and a 10 km link. pages 85–92, 03 2022.

[20] Darli Augusto de Arruda Mello and Fabio Aparecido Barbosa. *Digital Coherent Optical Systems: Architecture and Algorithms*. Springer, Cham, Switzerland, 2022.

[21] Inc. Thorlabs. Mpc320 - motorized fiber polarization controller. `https://www.thorlabs.com/thorproduct.cfm?partnumber=MPC320`, 2019. Accessed: 2025-05-06.

[22] Duma Optronics. Beamon - beam profiler, 2024. Accessed: 2025-06-04.

[23] Thorlabs, Inc. Pax5720vis-t. `https://www.thorlabs.com/catalogpages/Obsolete/2017/PAX5720VIS-T.pdf`, 2017. Accessed: May 2025.

[24] Thorlabs, Inc. Pax57205720 series polarimeters. `https://www.thorlabs.com/drawings/7bd4f036e9bc133f-515A4F4D-07D5-3089-EFC0DECB74D9F14F/PAX5710VIS-T-SpecSheet.pdf`, 2017. Accessed: May 2025.

[25] Ľubomír Škvarenina, Stephen Simpson, Yashar Alizadeh, and Martin Lavery. Extraction of bend-resolved modal basis in deformed multimode fiber. 03 2025.

[26] David Terr. Hermitepoly.m. `https://www.mathworks.com/matlabcentral/fileexchange/4911-hermitepoly-m`, 2004. MATLAB Central File Exchange. Retrieved June 5, 2025.

[27] John. Plot hermite gaussian beams. `https://www.mathworks.com/matlabcentral/fileexchange/29258-plot-hermite-gaussian-beams`, 2025. MATLAB Central File Exchange. Retrieved June 5, 2025.

[28] MathWorks. corr2 — 2-d correlation coefficient, 2024. MATLAB File Exchange.

[29] Zhou Wang, A.C. Bovik, H.R. Sheikh, and E.P. Simoncelli. Image quality assessment: from error visibility to structural similarity. *IEEE Transactions on Image Processing*, 13(4):600–612, 2004.

[30] MathWorks. ssim function - Image Processing Toolbox. `https://www.mathworks.com/help/images/ref/ssim.html`, 2024. Accessed: 2025-06-16.

[31] Mehul P. Sampat, Zhou Wang, Shalini Gupta, Alan Conrad Bovik, and Mia K. Markey. Complex wavelet structural similarity: A new image similarity index. *IEEE Transactions on Image Processing*, 18(11):2385–2401, 2009.

[32] Zhou Wang and Eero P. Simoncelli. Translation insensitive image similarity in complex wavelet domain. In *IEEE International Conference on Acoustics, Speech, and Signal Processing (ICASSP)*, pages 573–576, 2005.

[33] Mehul. Complex-wavelet structural similarity index (cw-ssim). https://www.mathworks.com/matlabcentral/fileexchange/43017-complex-wavelet-structural-similarity-index-cw-ssim, 2025. MATLAB Central File Exchange. Retrieved June 18, 2025.